

3
0
5
0
6

A STUDY OF SOLID-PROPELLANT ROCKET
MOTOR EXPOSED MATERIALS BEHAVIOR

Vidya Project No. 9061

THIRD QUARTERLY PROGRESS REPORT
for the period from
1 December 1963 through 29 February 1964

RDT & DDC: (4)

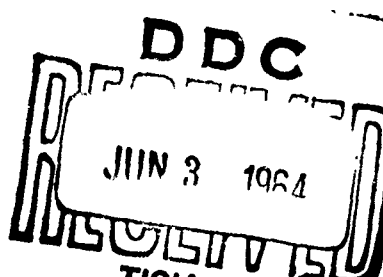
164-1-3.00

by

John W. Schaefer
Raymond E. Lundberg
Robert M. Kendall
Peter A. McCuen

for
AIR FORCE FLIGHT TEST CENTER
EDWARDS AIR FORCE BASE, CALIFORNIA

Contract No. AF 04(611)-9073
Air Force Program Structure No. 750G
AFSC Project No. 3059
AFSC Task Nos. 305907 and 305913



V I D Y A

RESEARCH

DEVELOPMENT

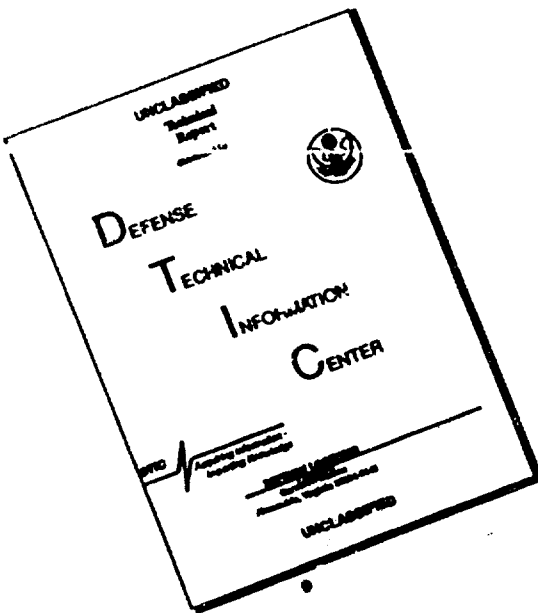
1450 PAGE MILL ROAD, PALO ALTO, CALIFORNIA

A DIVISION OF

Itek

CORPORATION

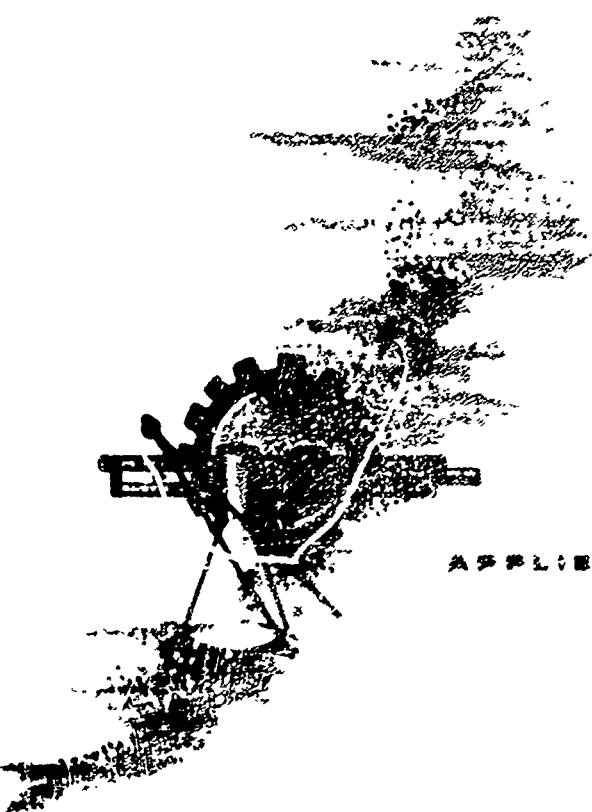
DISCLAIMER NOTICE



THIS DOCUMENT IS BEST
QUALITY AVAILABLE. THE COPY
FURNISHED TO DTIC CONTAINED
A SIGNIFICANT NUMBER OF
PAGES WHICH DO NOT
REPRODUCE LEGIBLY.

विद्या

The word *Vidya*, taken from the *Vedanta* philosophy of the Hindus, means knowledge. The symbol used to denote the *Vidya* organization is the letter "V" from Sanskrit, the ancient language of India.



APPLIED MECHANICS . . . PHYSICS . . . ANALYSIS

**A STUDY OF SOLID-PROPELLANT ROCKET
MOTOR EXPOSED MATERIALS BEHAVIOR**

THIRD QUARTERLY PROGRESS REPORT
for the period from
1 December 1963 through 29 February 1964

by

John W. Schaefer
Raymond E. Lundberg
Robert M. Kendall
Peter A. McCuan

for
AIR FORCE FLIGHT TEST CENTER
EDWARDS AIR FORCE BASE, CALIFORNIA

Contract No. AF 04(611)-9073
Air Force Program Structure No. 750G
AFSC Project No. 3058
AFSC Task Nos. 305907 and 305913

Vidya Project No. 9061



V I D Y A

A DIVISION OF

Itek

CORPORATION

1450 PAGE MILL ROAD • PALO ALTO, CALIFORNIA
TEL: DAVENPORT 1-2455 TWX: 415 492-9270

ACKNOWLEDGMENTS

The authors express their appreciation to the many Vidya staff members and others who have materially contributed to the study. In particular, the efforts of M. W. Rubesin, D. T. Flood, R. W. Higgins, and H. Aroeste are gratefully acknowledged.

SUMMARY

This report describes the work performed under Contract AF 04(611)-9073 during the third quarter of the contract period, beginning December 1963. The objectives of the study: ~~xxxx~~

(a) To develop design tools, in the form of digital computer programs, for the nozzle designer to use for calculating the behavior of materials exposed to a solid-propellant rocket-exhaust environment.

(b) To marshall existing theoretical methods, ~~and to extend these~~ or develop new methods ~~where necessary~~, to gain a better understanding of the fundamental mechanisms, ~~associated with~~ ~~explosive~~ ~~material behavior in a rocket-nozzle environment.~~

The work during this quarter ~~was~~ ^{was} ~~mainly~~ directed toward the development of two digital-computer programs. One ~~of these~~ is applicable to materials such as graphite and tungsten, that, ~~generally~~ erode with one moving boundary or do not erode at all. The other ~~is~~ applicable to the reinforced plastic materials that form a char layer. ~~This involved~~ ^{involved} ~~an~~ effort in the areas of transient conduction, equilibrium chemistry, reaction kinetics, and mass transport, as applied to the solid-propellant rocket problem, ~~which~~ is described in detail.

Further, an arc-plasma generator rocket-simulation test program has been conducted to study the effects of chemical and mechanical erosion of several material types, and the results of 43 nozzle firings are reported. A second test program to investigate the erosive effects of Al_2O_3 particle impaction has been formulated, and the proposed test plan is described. (See also AD 40843)

LIST OF CONTENTS

	<u>Page No.</u>
ACKNOWLEDGMENTS	ii
SUMMARY	iii
LIST OF FIGURES	vi
LIST OF SYMBOLS	ix
1. INTRODUCTION	1
2. THEORETICAL STUDIES	2
2.1 Introduction	2
2.2 Thermal Response of Materials Which Ablate With One Moving Boundary	3
2.2.1 Introduction	3
2.2.2 Surface chemical reactions	4
2.2.2.1 Surface equilibrium	7
2.2.2.2 Finite surface reaction rates	11
2.2.2.3 Graphite surface reactions	14
2.2.3 One moving-boundary computer program	17
2.3 Thermal Response of a Charring Ablator	22
2.3.1 Introduction	22
2.3.2 The differential equation for the tempera- ture field in a charring ablator	23
2.3.3 Thermophysical properties of a charring ablator	30
2.3.4 Surface chemical reactions	31
3. EXPERIMENTAL STUDIES	35
3.1 Introduction	35
3.2 Chemical-Erosion Test Program	37
3.2.1 Introduction	37
3.2.2 Facility modifications	39
3.2.3 Instrumentation and data reduction	40
3.2.4 Test results and discussion	45
3.2.4.1 Introduction	45
3.2.4.2 Pressure-distribution tests	46
3.2.4.3 Heat-transfer tests	47
3.2.4.4 Materials tests	51

	<u>Page No.</u>
3.2.4.4.1 Introduction	51
3.2.4.4.2 Post-test observations	53
3.2.4.4.3 Surface recession and surface- recession rate histories	59
3.2.4.4.4 Comparison of experiment with theo- retical prediction	62
3.2.4.4.5 Temperature histories	67
3.2.5 Summary	71
3.3 Particle-Impact Test Program	73
3.3.1 Introduction	73
3.3.2 Testing technique	74
3.3.3 Facility modification and instrumentation	77
3.3.4 Test preparations	80
REFERENCES	82
TABLES 1 AND 2	
FIGURES 1 THROUGH 35	
DISTRIBUTION LIST	

LIST OF FIGURES

- 1.- Program flow chart.
- 2.- Flow diagram of wall-erosion calculation.
- 3.- Theoretical chemical erosion of graphite in an H, C, N, O, C exhaust.
- 4.- Typical X-ray photograph for determining thermocouple locations.
- 5.- Pressure distribution, Mixture 4.
 - (a) 0.3-inch-diameter throat nozzle, high-temperature condition.
 - (b) 0.4-inch-diameter throat nozzle, high-temperature condition.
 - (c) 0.5-inch-diameter throat nozzle, high-temperature condition.
 - (d) 0.4-inch-diameter throat nozzle, low-temperature condition.
- 6.- Pressure distribution, Mixture 5.
 - (a) 0.3-inch-diameter throat nozzle, high-temperature condition.
 - (b) 0.4-inch-diameter throat nozzle, high-temperature condition.
 - (c) 0.5-inch-diameter throat nozzle, high-temperature condition.
 - (d) 0.4-inch-diameter throat nozzle, low-temperature condition.
- 7.- Heat-transfer coefficient axial distribution, Mixture 4.
 - (a) 0.3-inch-diameter throat nozzle, high-temperature condition.
 - (b) 0.4-inch-diameter throat nozzle, high-temperature condition.
 - (c) 0.5-inch-diameter throat nozzle, high-temperature condition.
- 8.- Heat-transfer coefficient axial distribution, Mixture 5.
 - (a) 0.3-inch-diameter throat nozzle, high-temperature condition.
 - (b) 0.4-inch-diameter throat nozzle, high-temperature condition.
 - (c) 0.5-inch-diameter throat nozzle, high-temperature condition.
- 9.- Test nozzle configuration, 0.3-inch-diameter throat.
- 10.- Cut-away of fired nozzle, Graphitite GX graphite, Mixture 4.
 - (a) Nozzle E17, nominal conditions of $T_o = 3500^{\circ}$ K,
 $(p_o)_{\theta=0} = 300$ psia, $\theta_f = 30.7$ sec, Test No. 939.
 - (b) Nozzle E10, nominal conditions of $T_o = 3500^{\circ}$ K,
 $(p_o)_{\theta=0} = 300$ psia, $\theta_f = 30.8$ sec, Test No. 940.
 - (c) Nozzle E19, nominal conditions of $T_o = 3500^{\circ}$ K,
 $(p_o)_{\theta=0} = 300$ psia, $\theta_f = 30.2$ sec, Test No. 997.
 - (d) Nozzle E31, nominal conditions of $T_o = 3500^{\circ}$ K,
 $(p_o)_{\theta=0} = 175$ psia, $\theta_f = 30.4$ sec, Test No. 998.
 - (e) Nozzle E13, nominal conditions of $T_o = 2750^{\circ}$ K,
 $(p_o)_{\theta=0} = 300$ psia, $\theta_f = 31.1$ sec, Test No. 1039.
 - (f) Nozzle E12, nominal conditions of $T_o = 2000^{\circ}$ K,
 $(p_o)_{\theta=0} = 300$ psia, $\theta_f = 30.7$ sec, Test No. 1023.

11.- Cut-away of fired nozzle, ATJ graphite, Mixture 4, nozzle E43, nominal conditions of $T_o = 3500^{\circ} K$, $(p_o)_{\theta=0} = 300$ psia, $\theta_f = 30.2$ sec, Test No. 1000.

12.- Cut-away of fired nozzle, MX4500 graphite phenolic, Mixture 4.

- (a) Nozzle E38, nominal conditions of $T_o = 3500^{\circ} K$, $(p_o)_{\theta=0} = 300$ psia, $\theta_f = 30.3$ sec, Test No. 1001.
- (b) Nozzle E39, nominal conditions of $T_o = 2750^{\circ} K$, $(p_o)_{\theta=0} = 300$ psia, $\theta_f = 30.5$ sec, Test No. 1040.
- (c) Nozzle E36, nominal conditions of $T_o = 2000^{\circ} K$, $(p_o)_{\theta=0} = 300$ psia, $\theta_f = 30.7$, Test No. 1024.

13.- Cut-away of fired nozzle, MX2600 silica phenolic, Mixture 4.

- (a) Nozzle E22, nominal conditions of $T_o = 3500^{\circ} K$, $(p_o)_{\theta=0} = 300$ psia, $\theta_f = 19.4$ sec, Test No. 941.
- (b) Nozzle E26, nominal conditions of $T_o = 2750^{\circ} K$, $(p_o)_{\theta=0} = 300$ psia, $\theta_f = 30.6$ sec, Test No. 1038.

14.- Cut-away of fired nozzle, Graphitite GX graphite, Mixture 5.

- (a) Nozzle E18, nominal conditions of $T_o = 3500^{\circ} K$, $(p_o)_{\theta=0} = 300$ psia, $\theta_f = 14.1$ and 14.5 sec, Test Nos. 957 and 958.
- (b) Nozzle E32, nominal conditions of $T_o = 3500^{\circ} K$, $(p_o)_{\theta=0} = 175$ psia, $\theta_f = 30.4$ sec, Test No. 1004.

15.- Cut-away of fired nozzle, ATJ graphite, Mixture 5, nozzle E42, nominal conditions of $T_o = 3500^{\circ} K$, $(p_o)_{\theta=0} = 300$ psia, $\theta_f = 30.4$ sec, Test No. 1005.

16.- Cut-away of fired nozzle, MX4500 graphite phenolic, Mixture 5.

- (a) Nozzle E35, nominal conditions of $T_o = 3500^{\circ} K$, $(p_o)_{\theta=0} = 300$ psia, $\theta_f = 26.2$ sec, Test No. 1006.
- (b) Nozzle E40, nominal conditions of $T_o = 2750^{\circ} K$, $(p_o)_{\theta=0} = 300$ psia, $\theta_f = 35.3$ sec, Test No. 1043.
- (c) Nozzle E37, nominal conditions of $T_o = 2000^{\circ} K$, $(p_o)_{\theta=0} = 300$ psia, $\theta_f = 6.5$ and 16.1 sec, Test Nos. 1026 and 1028.

17.- Cut-away of fired nozzle, MX2600 silica phenolic, Mixture 5.

- (a) Nozzle E24, nominal conditions of $T_o = 3500^{\circ} K$, $(p_o)_{\theta=0} = 300$ psia, $\theta_f = 20.8$ sec, Test No. 960.
- (b) Nozzle E27, nominal conditions of $T_o = 2750^{\circ} K$, $(p_o)_{\theta=0} = 300$ psia, $\theta_f = 30.6$ sec, Test No. 1042.
- (c) Nozzle E25, nominal conditions of $T_o = 2000^{\circ} K$, $(p_o)_{\theta=0} = 300$ psia, $\theta_f = 29.7$ sec, Test No. 1031.

- 18.- Surface recession and surface-recession rate, Graphitite GX graphite, Mixture 4.
 - (a) Nozzle E17, Test No. 939.
 - (b) Nozzle E10, Test No. 940.
 - (c) Nozzle E19, Test No. 997.
 - (d) Nozzle E31, Test No. 998.
- 19.- Surface recession and surface-recession rate, ATJ graphite, Mixture 4, nozzle E43, Test No. 1000.
- 20.- Surface recession and surface recession rate, MX4500 graphite phenolic, Mixture 4, nozzle E38, Test No. 1001.
- 21.- Surface recession and surface-recession rate, MX2600 silica phenolic, Mixture 4, nozzle E22, Test No. 941.
- 22.- Surface recession and surface-recession rate, MX2600 silica phenolic, Mixture 5, nozzle E24, Test No. 960.
- 23.- Comparison of surface-recession rate for graphite-nozzle firings.
- 24.- Comparison of surface-recession rate for graphite, graphite phenolic, and silica phenolic.
- 25.- Comparison of surface recession with and without swirl.
- 26.- Comparison of chemical-equilibrium surface-recession rate prediction with experiment, graphite.
- 27.- Temperature histories, Graphitite GX graphite, Mixture 4.
 - (a) Nozzle E10, Test No. 940.
 - (b) Nozzle E31, Test No. 998.
- 28.- Temperature histories, MX4500 graphite phenolic, Mixture 4, nozzle E38, Test No. 1001.
- 29.- Temperature histories, MX2600 silica phenolic, Mixture 4, nozzle E22, Test No. 941.
- 30.- Temperature histories, Graphitite GX graphite, Mixture 5.
 - (a) Nozzle E11, Test No. 959.
 - (b) Nozzle E32, Test No. 1004.
- 31.- Temperature histories, MX4500 graphite phenolic, Mixture 5, nozzle E32, Test No. 1004.
- 32.- Temperature histories, MX2600 silica phenolic, Mixture 5, nozzle E24, Test No. 960.
- 33.- Char recession and char depth, MX2600 silica phenolic, Mixture 4, nozzle E22, Test No. 941.
- 34.- Char recession and char depth, MX2600 silica phenolic, Mixture 5, nozzle E24, Test No. 960.
- 35.- Plenum extension ring for particle injection.

LIST OF SYMBOLS

B'	nondimensional blowing rate,	$\frac{(\rho v)_w}{\rho_e u_e c_M}$
C	specific heat	
c_p	specific heat at constant pressure	
c_H	heat-transfer coefficient defined by $q = \rho_e u_e c_H \Delta H$	
c_{H_0}	heat-transfer coefficient without wall blowing	
c_M	mass-transfer coefficient defined by	
	$\rho_e u_e c_M \Delta K_j = -\rho D_{jm} \left(\frac{\partial K_j}{\partial y} \right)_w$	
c_t	$\rho_p \epsilon_p c_p + (1-\epsilon_p) \rho_c c_c$	
D	nozzle diameter	
D_{jm}	diffusion coefficient of species j through the mixture	
ΔE	activation energy	
H	static enthalpy	
H_g	enthalpy of pyrolysis gases	
H_r	recovery enthalpy	
H_t	$(\rho_p H_p - \rho_c H_c) (\rho_p - \rho_c)$	
h	heat-transfer coefficient defined by $q = h \Delta t$	
k	thermal conductivity	
k_f, k_o, k_1	reaction rate constants	
K_{p_o}, K_p'	equilibrium constant	
K_j	mass fraction of molecular species j in the gas phase	

$\tilde{\kappa}_i$	mass fraction of elemental species i in the gas phase
m, n	indices in nodal network
\dot{m}_a	erosion rate of virgin ablator
\dot{m}_g	rate of transpiration of pyrolysis gases
M	molecular weight
p	pressure, partial pressure when subscripted
Pr	Prandtl number
q	heat flux, that is, energy per unit area, per unit time
q_{rad}	incident heat-flux due to radiation from the stream
r	radius, radial coordinate
r_s	surface radius
r_b	back-wall radius
\dot{R}	universal gas constant
Re	Reynolds number
T	absolute temperature
T_{pyro}	temperature indicated by pyrometer
u_e	velocity at the boundary-layer edge
u	velocity component parallel to the surface
v	velocity component normal to the surface
\dot{w}_j	net rate of production of the j th species
x	transformed coordinate in the heat equation, coordinate parallel to the surface in the boundary-layer equations
x_j	mole fraction of j th species
y	coordinate normal to the surface

z axial coordinate in a nozzle
 α_{ij} mass fraction of element i in species j
 γ isentropic exponent
 Δ difference
 ϵ surface emissivity
 ϵ_p volume fraction of undecomposed plastic
 θ time
 θ_f test duration
 μ absolute viscosity
 ρ mass density
 σ Stefan-Boltzmann constant

Subscripts

a ablation material
 c char layer
 e evaluated at the edge of the boundary layer
 i, j species i or j
 o evaluated at total or stagnation conditions
 p virgin plastic
 r evaluated at recover conditions
 w evaluated at the wall conditions
 $*$ evaluated at the nozzle throat

Superscripts

$*$ denotes condensed phase
 $'$ evaluated at reference condition or value at the end of a time step.

A STUDY OF SOLID-PROPELLANT ROCKET MOTOR EXPOSED MATERIALS BEHAVIOR

1. INTRODUCTION

During the past several years, significant theoretical techniques have been developed by various investigators for characterizing many of the complex individual phenomena occurring in the ablation process of solid-propellant rocket wall materials. These techniques have been used to gain a better understanding of ablation phenomena under simplified conditions and to guide, to a certain extent, the design of aft-closures and nozzles. The proven utility of the theoretical approach in this area has made meaningful the possibility of developing an integrated, more general, analytical technique for the design of solid-propellant rocket wall materials and configurations. The need for such a technique is becoming more urgent as motors increase in size, and thus render the traditional cut-and-try approach more costly and time-consuming.

Recognizing this need, the objectives of this study are two-fold:

- (1) To develop design tools for the nozzle designer to use for calculating the behavior of materials exposed to a solid-propellant rocket-exhaust environment. These design tools will be in the form of digital computer programs.
- (2) To marshall existing theoretical methods, and to extend these or develop new methods where necessary, to gain a better understanding of the fundamental mechanisms associated with exposed materials behavior in a rocket-nozzle environment. This second objective is, of course, coupled with the first in that an appreciation of the fundamental ablation mechanisms is required to calculate their effects.

Both theoretical and experimental studies are being conducted to accomplish the objectives of the program. The relations characterizing the ablation process are being formulated largely from theoretical considerations, but also draw on experimental work in

those areas not amenable to theoretical treatment. Existing test data are being used where available, and small-scale laboratory tests are being conducted as a part of this program to provide information in several areas where it is required. The flow chart of Figure 1 indicates how the various areas of investigations are interrelated.

As indicated in Figure 1, the theoretical studies are divided into two major categories, the first having to do with materials that erode with one "moving boundary" such as graphite (nonablating refractories are a special case of this category), and the second with materials such as the reinforced plastics, or composites, whose ablation can be characterized by two moving boundaries. The experimental studies are being carried out in the Vidya 1-megawatt arc-plasma generator facility; they consist of graphite and composite-nozzle ablation tests and metallic-oxide particle-impaction tests.

During the third quarter of the program, the theoretical effort continued in the following areas: thermal behavior of nonmelting, noncharring materials, thermal behavior of charring materials, and wall chemical erosion (both diffusion and kinetically controlled). The accomplishments here are reported in Section 2. The experimental effort during the quarter consisted of conducting and interpreting 43 nozzle firings under the chemical-erosion program and formulating test plans for the particle impact program. This work is discussed in Section 3.

2. THEORETICAL STUDIES

2.1 Introduction

For the purpose of classification, all engineering effort on the program that does not directly involve an experimental test program is called "theoretical." This is actually a misnomer, since the effort is based largely on proven physical and mathematical relations, and is of a very practical and applied nature;

that is, the effort is directed toward the construction of calculation tools for characterizing the phenomena occurring at an eroding nozzle wall. Because many physical relations are needed for this characterization, and because the interactions between them are quite complex, an analysis flow diagram was prepared (Fig. 2) to help clarify the role of each area of study.

Figure 2 is itself necessarily complex, but it is hoped that it will be helpful in placing each phase of the effort discussed herein in proper perspective. The row of boxes at the top of the figure represents the various inputs required to perform nozzle wall erosion calculations; except for the erosion effects of particle impact, none of these specific data are being sought experimentally under the present contract. The program emphasis, rather, is on the "calculation" area of the figure, to provide a technique for determining nozzle erosion rates and wall temperature from the input data.

The work reported in this section is in the areas of surface chemical reactions and internal material behavior. As the reader reviews the work, it is recommended that he refer to Figure 2 occasionally to review the role of each study.

2.2 Thermal Response of Materials Which Ablate With One Moving Boundary

2.2.1 Introduction

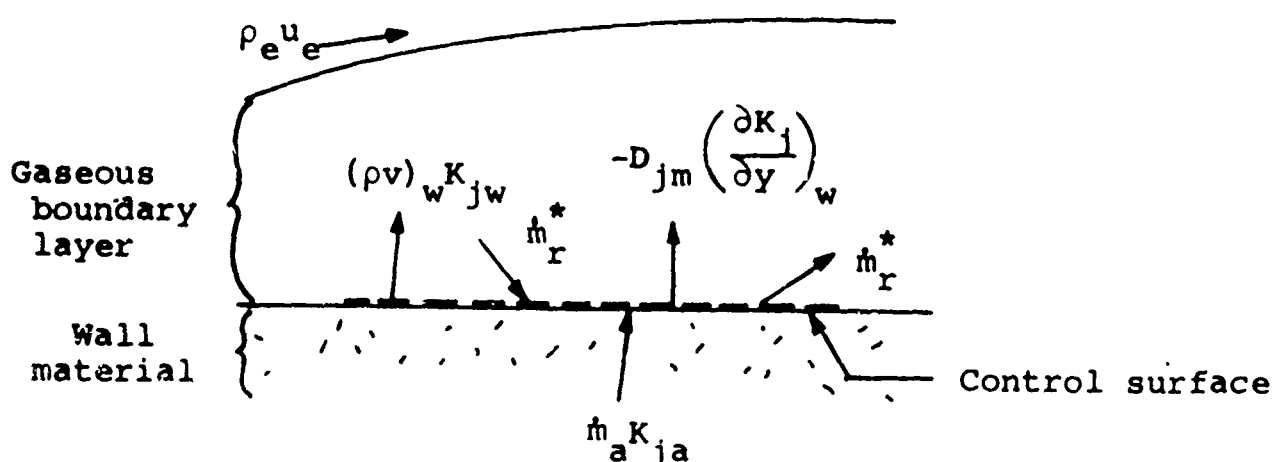
The class of materials considered here is that class which undergoes physical and chemical change only at the surface which is exposed to the exhaust environment. The most common example of these materials encountered in rocket motors is graphite. A prediction of the response of this class of materials to an exhaust environment involves a consideration of the internal thermal response (through conduction of heat away from the exposed surface) and the thermal and chemical interaction between the exposed surface and the exhaust stream.

2.2.2 Surface chemical reactions

A study of the chemical reactions occurring at the exposed surface has a two-fold purpose, first, to determine the rate at which wall material is consumed by chemical reactions and, second, to enable specification of the energy state (enthalpy) of the mixture of gases existing at the wall. In general, these quantities are determined as functions of temperature and exhaust stream parameters (pressure, transfer coefficients, etc.) and are needed to supply a boundary condition to the calculation of the temperatures in the interior of the wall material.

The basic analytical technique used to calculate the desired quantities is a surface mass balance. This mass balance simply states that the net rate of arrival of an identifiable molecular species to the surface must vanish; that is, the sum of the rates of supply of a molecular species due to gas convection normal to the surface, diffusion through the boundary layer, condensed phase mass addition and chemical reactions at the surface must be zero. Further discussion of the mass balance technique can be found in References 1 and 2.

Consider the control surface shown in the following sketch:



The basic mass balance at the surface can be written as follows:

$$\begin{aligned}
 (\rho v)_w K_{jw} - D_{jm} \left(\frac{\partial K_j}{\partial y} \right)_w + \dot{m}_r^* K_{jr}^* \\
 = \dot{m}_a K_{ja} + \dot{m}_d^* K_{jd}^* + \dot{w}_j \quad (1)
 \end{aligned}$$

where

- $(\rho v)_w$ net convective mass-velocity normal to the surface
- K_{jw} mass fraction of species j in the surface gas mixture
- D_{jm} diffusion coefficient of species j through the mixture
- \dot{m}_r^* mass rate of removal of condensed phase material from the surface
- K_{jr}^* mass fraction of species j in the condensed phase material being removed
- \dot{m}_a mass rate of erosion of virgin ablator
- K_{ja} mass fraction of species j in the ablation material
- \dot{m}_d^* mass rate of deposition of condensed phase material
- K_{jd}^* mass fraction of species j in the condensed phase material being deposited
- \dot{w}_j net rate of production of species j due to surface chemical reactions

The chemical production term \dot{w}_j can, in general, be expressed in the form of a reaction-rate term multiplied by a difference in partial pressures. For example, if the reaction



is the only reaction involving CO_2 at the surface, then

$$\dot{w}_{CO_2} = k_f \left(\frac{p_{CO}}{K_p}^2 - p_{CO_2} \right) \quad (3)$$

where

k_f reaction rate constant

p_{CO} partial pressure of CO

p_{CO_2} partial pressure of CO_2

K_p equilibrium constant for reaction (2)

The reaction rate k_f is a function of temperature, as is K_p , and the p_j are related to the K_j through the equation

$$K_j = \frac{M_j p_j}{pM}$$

where p is the system pressure and M the molecular weight of the gas mixture at the surface. Writing Equation (1) for each species considered yields J equations which are, in principle, independent. It will be shown later that in a practical sense they may not all be independent. We have, in addition, the equations

$$\sum_{j=1}^J K_j = 1 \quad (4)$$

and

$$M = \sum_{j=1}^J M_j \frac{p_j}{p} \quad (5)$$

Hence, we have $J+2$ equations. However, the unknown quantities are

K_j , $\partial K_j / \partial y$, $(\rho v)_w$, and M , so that there are $2J+2$ unknowns. We might introduce the boundary-layer equations, but this introduces considerable complexity quickly. Instead, we would like to introduce a general transport equation, which really represents an integrated form of the boundary-layer equations, in the form

$$-D_{im} \left(\frac{\partial K_j}{\partial y} \right)_w = \rho_e u_e C_{M_j} (K_{jw} - K_{je}) \quad (6)$$

Equation (6) can only reasonably be expected to hold for a non-reacting boundary layer. If reactions occur in the boundary layer, its application to a reacting species can be shown to result in a logical contradiction, at least under some, if not under all circumstances. The idea of introducing Equation (6) is still very appealing, however, because if the K_{je} are known, the number of equations in the system is increased to $2J+2$ without increasing the number of unknowns, and we have immediately a determinate system. It will be shown in the next two sections how Equation (6) can be applied to many situations of interest, even without the restrictive assumption of a chemically frozen boundary layer. Because some simplifications result when the gas mixture at the surface is in equilibrium, we shall consider that case first before turning to the general situation with finite surface-reaction rates.

2.2.2.1 Surface equilibrium

Equilibrium at the surface will be achieved when the reaction rates are very large. Consider the general chemical reaction



where N_j is a general chemical symbol and r , n , q , and s are the stoichiometric coefficients. Ideally, the rate of production of species j by this general reaction can be expressed as

$$\dot{w}_j = k_{fj} \left(\frac{p_m^q p_k^s}{K_{pj}} - p_j^n p_l^r \right) \quad (8)$$

where K_{pj} is the equilibrium constant for the general reaction. This will be taken to represent both surface and gas-phase reactions. If the reaction given by Equation (7) is nonideal, the exact form of Equation (8) may be altered. For example, the exponents on the partial pressures may not equal the stoichiometric coefficients. However, the net production of any species is still expressed as the difference between a forward and a reverse reaction rate.

If we substitute Equation (8) for \dot{w}_j in Equation (1) and divide by k_{fj} we have

$$\left(\frac{p_m^q p_k^s}{K_{pj}} - p_j^n p_l^r \right) = \frac{(\rho v)_w}{k_{fj}} K_{jw} - \frac{D_{jm}}{k_{fj}} \left(\frac{\partial K_j}{\partial y} \right)_w + \frac{\dot{m}_r^*}{k_{fj}} K_{jr}^* - \frac{\dot{m}_a}{k_{fj}} K_{ja} - \frac{\dot{m}_d}{k_{fj}} K_{jd}^* \quad (9)$$

when, as $k_{fj} \rightarrow \infty$

$$\left(\frac{p_m^q p_k^s}{K_{pj}} - p_j^n p_l^r \right) \rightarrow 0 \quad (10)$$

Now we notice that the J unknowns, $\partial K_j / \partial y$, do not appear and, further, Equation (10) is exactly the equilibrium relation among the partial pressures of the species involved in reaction (7). It should be noted that the ideal form chosen for the general reaction rate, Equation (8), in no way influences the conclusion. The same

conclusion is reached if one recognizes that only at equilibrium the forward rate equals the reverse rate.

For those molecules which do not react with the surface but which may experience gas phase reactions, the same results can be obtained by writing a mass balance for a small but still finite volume element adjacent to the surface. As $k_{fj} \rightarrow 0$, all of the terms in the mass balance will vanish except for the equilibrium relation, Equation (10).

We have not, however, completely abrogated the difficulty with the system of equations resulting from Equation (1). We have, to be sure, reduced the number of unknowns to $J+2$, but it can be shown that of the equilibrium relations among J molecular species only $J-I$ are independent, where I is the number of elements present in the system; thus, we have only $J+2 - I$ independent equations, and $J+2$ unknowns.

To supply the additional equations required we shall make a mass balance on the chemical elements at the surface. If j molecules involve element i and α_{ij} is the mass fraction of element i in molecule j , we can multiply Equation (1) by α_{ij} and sum over j , obtaining

$$\begin{aligned} (\rho v)_w \tilde{K}_{iv} - \sum_j \alpha_{ij} D_{jm} \left(\frac{\partial K_j}{\partial y} \right)_w + \dot{m}_r^* \tilde{K}_{ir}^* \\ = \dot{m}_a \tilde{K}_{ia} + \dot{m}_d^* \tilde{K}_{id}^* + \sum_j \alpha_{ij} \dot{w}_j \end{aligned} \quad (11)$$

where the tilde indicates an elemental mass-fraction. Since elements are conserved,

$$\sum_j \alpha_{ij} \dot{w}_j \equiv 0$$

If the D_{jm} are equal or if we accept a weighted average diffusion coefficient, Equation (11) becomes

$$(\rho v)_w \tilde{K}_{iw} - D_{im} \left(\frac{\partial \tilde{K}_i}{\partial y} \right)_w + \dot{m}_r^* \tilde{K}_{ir}^* = \dot{m}_a \tilde{K}_{ia} + \dot{m}_d^* \tilde{K}_{id} \quad (12)$$

Lees, Reference 3, presents a plausibility argument suggesting that the diffusional mass flux of the elements, which are of course conserved through the boundary layer, can be expressed as

$$-D_{im} \left(\frac{\partial \tilde{K}_i}{\partial y} \right)_w = \rho_e^u e^{C_{M_i}} (\tilde{K}_{ie} - \tilde{K}_{iw}) \quad (13)$$

Then, Equation (12) becomes

$$(\rho v)_w \tilde{K}_{iw} + \rho_e^u e^{C_{M_i}} (\tilde{K}_{iw} - \tilde{K}_{ie}) + \dot{m}_r^* \tilde{K}_{ir} = \dot{m}_a \tilde{K}_{ia} + \dot{m}_d^* \tilde{K}_{id} \quad (14)$$

If values are available for $\rho_e^u e^{C_{M_i}}$, \dot{m}_d^* , and \tilde{K}_{ie} , the elemental composition of the gas mixture at the wall can be determined as a function of wall erosion rate, \dot{m}_a . For example, if $\dot{m}_r^* = \dot{m}_d^* = 0$, Equation (14) assumes the familiar form (see Ref. 1)

$$\tilde{K}_{iw} = \frac{\tilde{K}_{ie} + B' \tilde{K}_{ia}}{1 + B'} \quad (15)$$

where

$$B' = \frac{(\rho v)_w}{\rho_e^u e^{C_{M_i}}}$$

It is not necessary for the C_{M_i} to be equal in order to get a solution, but it certainly simplifies computation.

Then the equilibrium chemical system previously developed becomes determinate with the addition of I equations of the form

$$\sum_j \alpha_{ij} K_{jw} = \tilde{K}_{iw} \quad (16)$$

2.2.2.2 Finite surface reaction rates

If some of the surface reactions are slow enough that the terms on the right-hand side of Equation (9) are significant, we are still caught in the original equation shortage dilemma. The escape here is to devise a model for which the transport equation, Equation (6), might reasonably be expected to apply, and then to use it to supply the additional equations needed to arrive at a determinate system.

We shall consider a subsystem consisting of a group of molecular species which share a common element. The common, or bound, element is distributed among the species of the subsystem according to the dictates of overall system equilibrium, but enters or leaves the subsystem only by way of specified surface reactions. The rates of the surface reactions involving the bound element can be anything from zero to infinity. All the other elements in the subsystem may enter or leave only by way of fast reactions.

A mass balance on the bound element at the surface is (assuming no condensed phase transport)

$$(\rho v)_w \tilde{K}_{iw}^b - D_{im}^b \left(\frac{\partial \tilde{K}_i^b}{\partial y} \right)_w = \dot{m}_a \tilde{K}_{ia}^b + \dot{w}_i^b \quad (17)$$

where the superscript b refers to the bound element alone in order to distinguish these atoms from other atoms of the same element which may be present outside the subsystem.

Since the bound element is conserved in the boundary layer, we might expect that the transport equation, Equation (6), would be valid. Then we have

$$-D_{im}^b \left(\frac{\partial \tilde{K}_i^b}{\partial y} \right)_w = \rho_e^u e^c M_i^b (\tilde{K}_{iw}^b - \tilde{K}_{ie}^b) \quad (18)$$

If we associate a subsystem with each of the "slow" surface reactions, the bound element balance, Equation (17), replaces the surface balance on the reacting molecular species, Equation (1). Hence, the concentration gradient of the reacting species does not appear as an unknown in the system of equations, but we have introduced \tilde{K}_{iw}^b and $(\partial \tilde{K}_i^b / \partial y)_w$ as additional unknowns. One of the additional equations needed is supplied by Equation (18); the other comes from conservation of the bound element and is

$$\tilde{K}_i^b = \sum_j \alpha_{ij}^b K_j \quad (19)$$

where the summation is only over those molecules in the subsystem. This concept of the equilibrium microcosm containing a conserved element was conceived by Kendall and first presented in a paper by Kendall and Rindal, Reference 4. The principal utility of the concept is to allow the use of the macroscopic equations to quantify mass diffusion to a general reacting surface. Inherent in the definition of the subsystem is that gas-phase reactions affecting the species in the subsystem are fast. There appears to be no great difficulty in relaxing this assumption and this will be pursued in future effort.

To illustrate this concept, consider a subsystem composed of acetylene and methane. The bound element is taken to be carbon and enters the subsystem only through the reaction



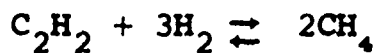
Then, since the mass fraction of carbon in C_2H_2 is 24/26, the production rate of bound carbon is

$$w_C^b = \frac{24}{26} k_f \left(\frac{p_{H_2}}{K_p} - p_{C_2H_2}^b \right) \quad (21)$$

where k_f and K_p are the reaction rate constant and equilibrium constant, respectively, for reaction (20). The statement that the bound element distributes itself in the subsystem according to the dictates of equilibrium means that

$$\frac{\left(p_{C_2H_4}^b \right)^2}{p_{C_2H_2}^b \times \left(p_{H_2} \right)^3} = K_p' \quad (22)$$

where K_p' is the equilibrium constant for the reaction



The mass balance on bound carbon at the surface becomes

$$(pv)_w \tilde{K}_{Cw}^b + p_e^u c_M (\tilde{K}_{Cw}^b - \tilde{K}_{Ce}^b) = \frac{24}{26} k_f \left(\frac{p_{H_2}}{K_p} - p_{C_2H_2}^b \right) \quad (23)$$

And the conservation equation is

$$\tilde{K}_C^b = \frac{24}{26} K_{C_2H_2}^b + \frac{12}{16} K_{CH_4} \quad (24)$$

The specification of the state of the subsystem then requires the simultaneous solution of Equations (22), (23), and (24).

2.2.2.3 Graphite surface reactions

For the graphite wall in an H, C, N, O, Cl exhaust, three such subsystems were chosen. They were

- (a) The compounds C_2H_2 , CH_4 , C_2H , C_3H , C_4H , C_6H , CH_2 , C_4H_2 , and C_3H_2 , containing bound carbon produced by reaction (20);
- (b) The compounds H_2O , OH , O , and O_2 , containing bound oxygen produced (in this case consumed is a better word) by the reaction

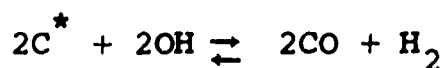


- (c) The compound CO_2 alone produced by the reaction

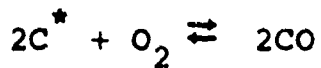


The remaining compounds considered were assumed to satisfy the conventional equilibrium relations among their partial pressures.

It should be apparent that there is some latitude in the selection of the molecules which are included in the various subsystems. For example, C and O_2 could well be included with the CO_2 in the third subsystem, rather than in the second subsystem. In principle, one can also consider two (or more) parallel reactions as contributing to the supply (or consumption) of the "bound" elements in the subsystem. The choice of the three specific reactions for the graphite wall was prompted by the availability of data and the significance of molecular concentrations. For example, data on the reaction



were lacking, and very little free O_2 is present in the exhaust so that the reaction



was not considered. The final test of the adequacy of the choice of member compounds in the various subsystems will be in how well the calculation fits observed performance. All of the molecular species which react with the wall to any extent should in some manner be tied to a reaction which is kinetically controlled, since this will insure compliance with the observed phenomenon of zero erosion at low wall temperatures. Thus, even though the reaction of OH with graphite was not considered directly, the inclusion of OH in subsystem (b) ties that molecule to a kinetically controlled wall reaction.

For acetylene production, the reaction rate was determined by an extrapolation of data given by the Union Carbide Research Institute, References 5 and 6. Expressed in an Arrhenius form, the rate is given by

$$(k_f)_{C_2H_2} = 4.525 \times 10 \exp\left(\frac{-81,200}{T}\right) \frac{lb}{ft^2 \cdot sec \cdot atmosphere} \quad (27)$$

where T is in $^{\circ}K$.

For the CO_2 - graphite reaction given by Equation (2), the rate was taken to be

$$(k_f)_{CO_2} = 13.83 \times 10^7 \exp\left(\frac{-42,000}{T}\right) \frac{lb}{ft^2 \cdot sec \cdot atmosphere} \quad (28)$$

where T is in $^{\circ}K$. This represents an extrapolation of an equation given by Walker, Rusinko, and Austin, Reference 7, which was based on measurements by Gulbranson and Andrew, Reference 8, and Armington, Reference 9.

Blyholder and Eyring, Reference 10, express the rate of reaction (25) as

$$\dot{w}_{H_2O} = \frac{k_1 \left(\frac{p_{H_2} \cdot p_{CO}}{1 + (k_0 p_{H_2O})^{1/2}} - p_{H_2O} \right)}{\left[1 + (k_0 p_{H_2O})^{1/2} \right]^2} \frac{lb}{sec \cdot ft^2} \quad (29)$$

where K_p is the equilibrium constant for reaction (25). The rate constants are given by

$$k_1 = \left(\frac{2217}{T} \right) \exp \left(\frac{-17,900}{T} \right) \frac{lb}{ft^2 \cdot sec \cdot atmosphere} \quad (30)$$

and

$$k_0 = \left(\frac{7.024}{T} \right) \exp \left(\frac{-19,830}{T} \right) \frac{lb}{atmosphere} \quad (31)$$

where, again, T is in $^{\circ}K$.

Using the rate constants given by Equations (27), (28), (30), and (31), the nondimensional erosion rate of a graphite wall in a typical exhaust was calculated. Figure 3 is a plot of

$$B' = \frac{(\rho v)_w}{\rho_e u_e c_M}$$

as a function of wall temperature. For comparison purposes, Figure 3 also shows the predicted erosion if all surface chemical reactions are very fast, that is, if equilibrium is achieved. The profound effect of reaction kinetics is clear. On the basis of very sparse nozzle erosion data, it appears that the kinetically controlled prediction is closer to the real situation than is the prediction based on fast reactions.

In order to predict with accuracy the performance of a graphite wall in a rocket exhaust, one must have reliable rate data for the particular type of graphite and graphite reactions involved.

2.2.3 One-moving-boundary computer program

A digital computer program has been developed to calculate the thermal response of materials which erode with one moving boundary. There are two fairly distinct, but coupled, parts to the program. One deals with the conduction of heat to the interior, the other with the convection of heat and mass to the ablating surface.

The internal thermal response portion of the program is an explicit finite difference solution of the differential equation of heat conduction. The form and derivation of this equation are discussed at length in References 1 and 2 and will not be repeated here. The differential equation is transformed into a coordinate system fixed to the ablating surface as follows. The basic body shape considered is two-dimensional and axisymmetric, that is, it can be specified in r - and z -coordinates. The differential equation for the conduction of heat in axisymmetric cylindrical coordinates is transformed from r -, z -, and θ -coordinates to x -, z' -, and θ' -coordinates via the transformations

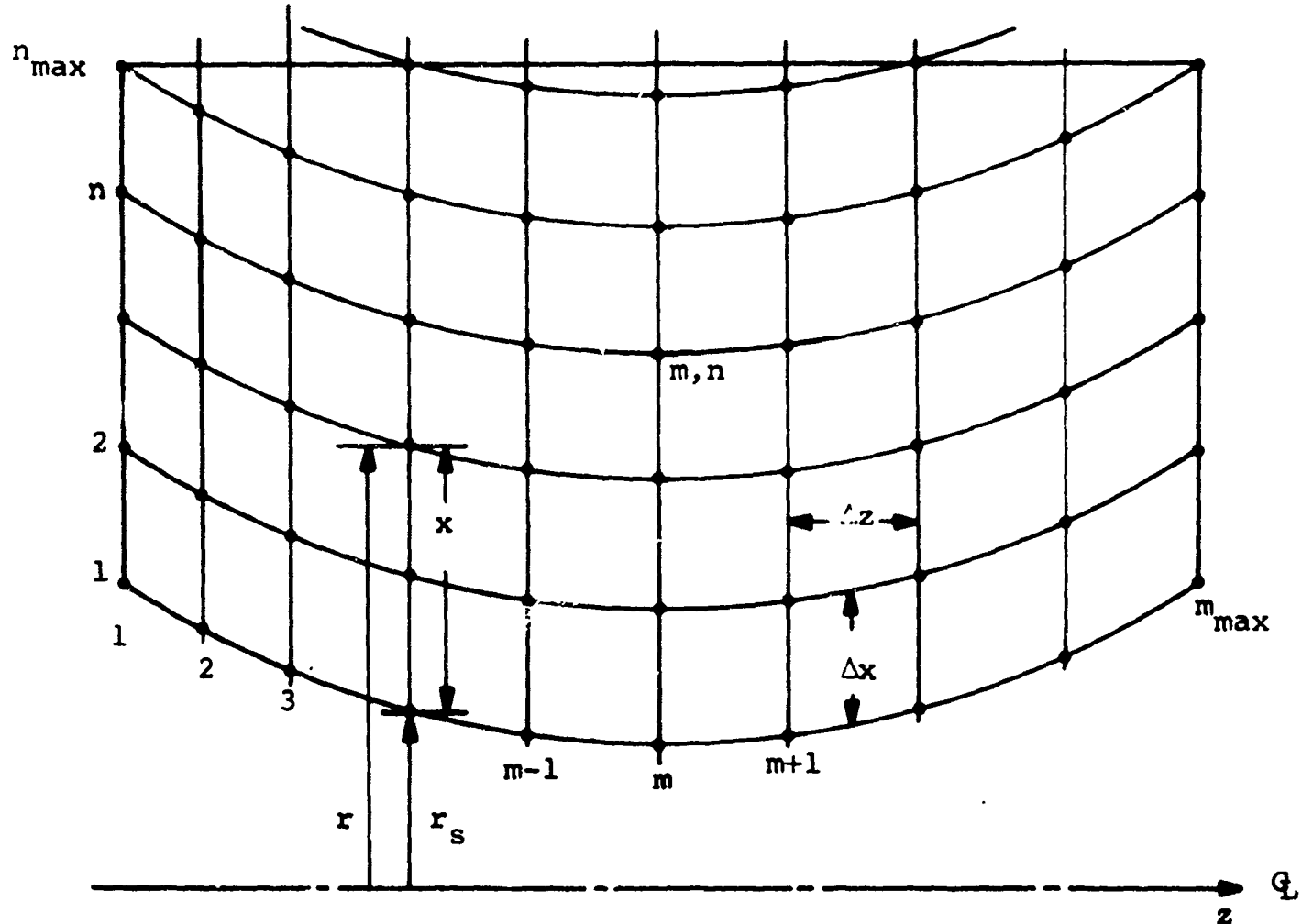
$$x = r - r_s$$

$$z' = z$$

$$\theta' = \theta$$

where r_s is the local surface radius. Because the surface can recede, r_s is a function of both axial position, z , and time, θ .

The following sketch illustrates the basic body shape and nodal positions:



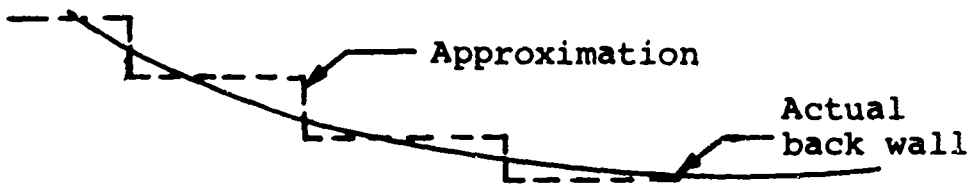
Grid lines of the coordinate system are constant- x and constant- z lines. Nodes are positioned at the intersections of the grid lines. The position of any node is specified by the double index m, n . The axial, or z -position index, m , runs from 1 to m_{\max} . The radial, or x -position index, n , runs from 1 to n_{\max} and, in general, n_{\max} is different for each value of m .

The inner surface shape is arbitrary so long as it is continuous. The selection of Δz and Δx is arbitrary within the

context of the stability of the explicit solution to the difference equations.

Of course, the spacing, Δx , between adjacent rows of nodes is constant along any row, and the spacing, Δz , between adjacent columns of nodes is constant up any column, but either or both may vary from row to row or column to column as the case may be.

The side walls are assumed to be lines of constant- z , the back wall composed of constant- r and constant- z segments with, however, the boundary condition always written only for the constant- r segment. In this way, an arbitrary back wall can be approximated as shown in the following sketch:



The boundary condition which is applied at each intersection of the constant- x lines with the side walls and at each intersection of the constant- z lines with the back wall is

$$a \frac{\partial T}{\partial n} + bT = c \quad (32)$$

where n is the outward normal direction and a , b , and c are specified constants.

The energy input to the ablating surface is determined from a general convection condition. If the mass-transfer coefficients for all species are equal and the Lewis-Semenov number is unity we have¹

¹A thorough discussion of the rationale leading to Equation (2) is given by Kendall and Rindal, Reference 4.

$$q_{\text{net}} = \rho_e u_e C_H \left[H_r + B' H_a - (1 + B') H_w \right] - \sigma \epsilon T_w^4 + q_{\text{rad}} + q_p \quad (33)$$

where

C_H heat-transfer coefficient

H_r recovery enthalpy

H_a enthalpy of virgin ablator at wall temperature

H_w enthalpy of gas mixture at the wall

ϵ emissivity of the surface

q_{rad} incident radiation heat flux

q_p incident heat flux due to particle impingement

T_w wall temperature

The dimensionless erosion rate, B' , and the wall gas enthalpy, H_w , are obtained from an analysis of the surface chemical reactions as described in Section 2.2.2. The quantities $\rho_e u_e C_H$, H_r , q_{rad} , and q_p are properties of the exhaust stream and must be derived from an analysis of it. The quantities H_a and ϵ are properties of the wall material.

In order to allow for some generality in the problems which can be treated, the one-moving boundary program is equipped with three different options for the specification of surface boundary conditions. Option 1 relates specifically to the erosion of a graphite wall in an H, C, N, O, Cl exhaust. The ablating surface heat flux is calculated by Equation (33). A subroutine is provided which calculates B' , H_w , and ϵ from the set of chemical and

transport equations described in Section 2.2.2. The three reactions given by Equations (2), (20), and (25) are presumed to proceed at finite rates.

The user of the program can either accept the built-in reaction constants given in Section 2.2.2 or can specify his own reaction rates in the general Arrhenius form

$$k_f = A e^{-B/RT} \quad (34)$$

The specification of rate constants is made by inputting the values of A and B for each of the three reactions, Equations (2), (20), and (25). Under this specification, reaction (25) is presumed to be ideal, that is, the denominator in Equation (29) is unity. The builtin reaction constants will be revised throughout the remainder of the current project as (or if) newer or better data become available.

The remainder of the information needed to evaluate Equation (33) is supplied to the program by the way of tables as functions of firing time. The surface emissivity and, of course, the r- and z-direction thermal conductivities are to be provided as tabular functions of temperature.

The program modifies the heat-transfer coefficient for wall blowing by the empirical relation

$$\rho_{e^u e^c H} = \rho_{e^u e^c H_0} \left[1 - 0.2 \left(\frac{M_e}{M} \right)^{1/3} B' \right]$$

where

C_{H_0} heat-transfer coefficient in the absence of blowing

M_e molecular weight of the exhaust stream gas mixture

M molecular weight of the gases added at the wall

The user provides a table of $\rho_e^u e^{C_{H_o}}$ which may be obtained by the ARM method as discussed in Reference 2.

Under option (2), Equation (33) is still used to calculate the surface heat flux, but B' , H_w , and H_a can be provided as tabular functions of wall temperature. In this way, the same moving-boundary conduction package can be used for materials or exhausts other than those covered by the chemical erosion subroutine.

Option (3) provides for specification of both B' and T_w as tabular functions of firing time. This option will be principally used in evaluating test data where the requisite information may be available from independent measurements.

Complete details on the use of the program and the various boundary-condition options will be covered in a users' manual. The principal effort on the one-moving-boundary program during the next quarter will be in making minor modifications and the preparation of the users' manual.

2.3 Thermal Response of a Charring Ablator

2.3.1 Introduction

When a material, such as a resin-impregnated composite, can experience gross physical or chemical change in the interior as well as at the surface, the description of the internal thermal response of these materials to a heating environment can no longer be given in terms of simple heat conduction. In addition to the transport of energy by conduction, one must consider the effects of variable density, consumption of energy due to formation of products of pyrolysis, and the transport of energy through a porous char material by these products of pyrolysis.

In addition to the modification of the equation describing the internal thermal response, an analysis of these materials requires a consideration of two other phenomena. First, the mechanism of the pyrolysis itself must be understood and quantified.

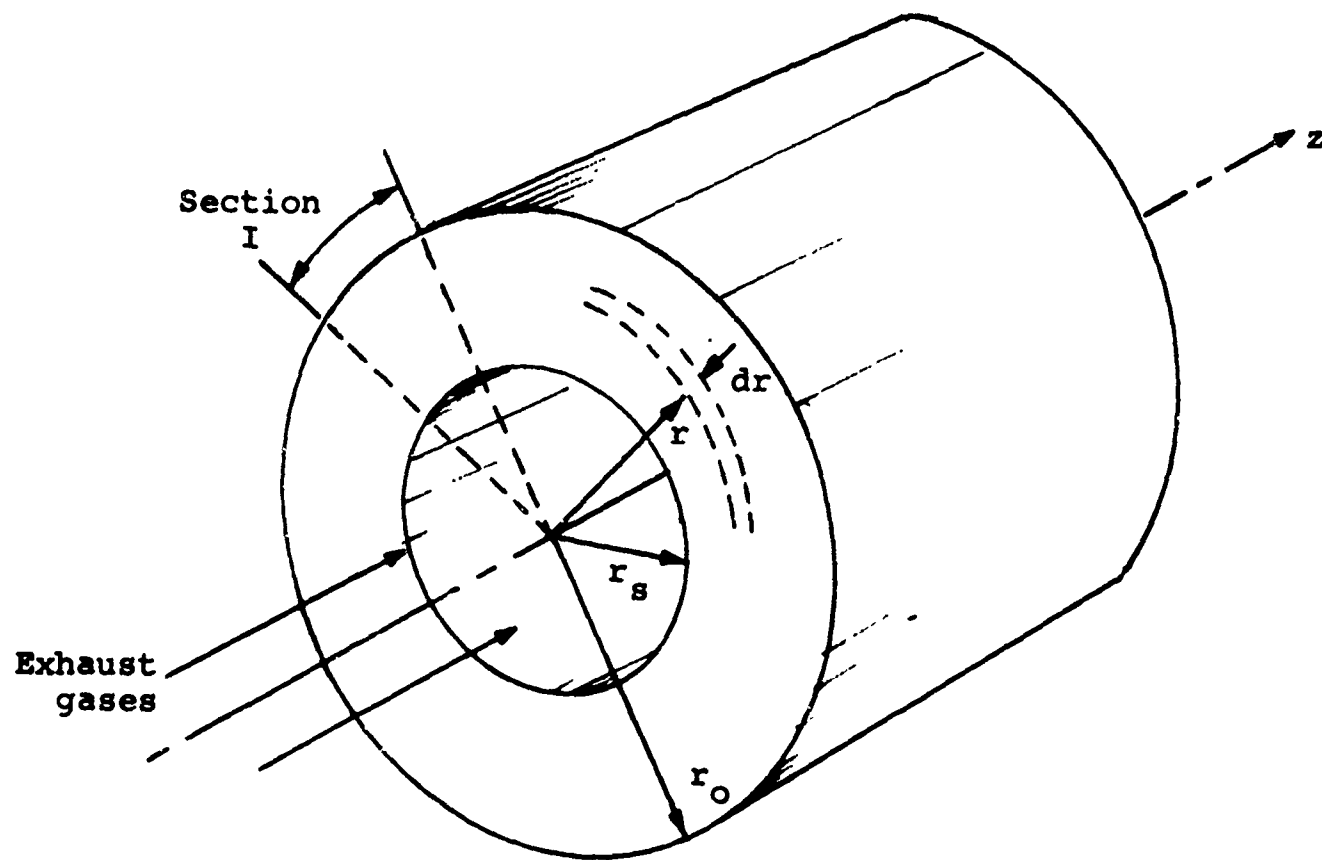
Frequently, this requires a kinetic description of the decomposition, rather than the assumption of a discontinuous process which occurs at some threshold temperature (as, for instance, melting). Second, the chemical reactions between the pyrolysis gases and the gases at the exposed surface must be considered.

All of these phenomena, collectively, comprise the "response" of a charring ablator to the exhaust environment. All of them and the coupling among them must be considered in order to predict that response. In the following sections, the equations describing the internal thermal response of a charring ablator will be developed, and the calculative technique used for prediction of chemical erosion of the surface when all the chemical reactions are fast (i.e., equilibrium is obtained) will be presented. The use of these equations and calculative techniques to predict the response of a charring ablator to a rocket-engine exhaust is the principal task of the next quarter.

2.3.2 The differential equation for the temperature field in a charring ablator

Because the types of materials comprising the class referred to as "charring ablators" have, in general, a low thermal conductivity and are used in regions of a rocket nozzle where the axial gradients of stream conditions are not severe, a one-dimensional axisymmetric body was chosen as the representative shape.

Consider the body represented by the following sketch (assuming a unit dimension in the z-direction):



Let us make an energy balance on an annular ring of differential thickness, dr , as shown in the sketch. The net energy transport into the element by conduction is

$$2\pi \frac{\partial}{\partial r} \left(r k \frac{\partial T}{\partial r} \right) dr$$

where K must be thought of as a local effective conductivity. If the local rate of transpiration of pyrolysis gases is denoted by \dot{m}_g and the enthalpy of the gases by H_g , then the net energy transport into the element by the moving gases is

$$- \frac{\partial}{\partial r} (\dot{m}_g H_g) dr$$

The rate of change of thermal energy storage in the differential ring is

$$2\pi r dr \frac{\partial(\rho H)}{\partial \theta}$$

where ρ and H are the density and enthalpy, respectively, of the material contained in the differential ring. Then, the equation for the conservation of energy is

$$r \frac{\partial(\rho H)}{\partial H} = \frac{\partial}{\partial r} \left(r k \frac{\partial T}{\partial r} \right) - \frac{1}{2\pi} \frac{\partial(\dot{m}_g H_g)}{\partial r} \quad (35)$$

In order to use Equation (34) for computation, we must be able to evaluate the material thermal and transport properties, ρH , k , and H_g , as well as the rate of gas transpiration, \dot{m}_g , as functions of position and local temperature. For this purpose, let us consider each of the terms in Equation (34) in greater detail.

At any instant in time, the ablating material will be considered as being composed of two parts: the first, virgin plastic and the second, completely decomposed char. Notice that both the virgin plastic and the charred material may themselves be composites of some sort. If we denote properties of the plastic by the subscript p and those of the char by the subscript c , we may write

$$\rho = \epsilon_p \rho_p + (1 - \epsilon_p) \rho_c \quad (35)$$

where ϵ_p is the volume fraction of undecomposed plastic existing at any instant in time. For undecomposed material ϵ_p is 1, for the char layer ϵ_p is 0, and for other locations it may be anywhere in between. Further, we have

$$\rho H = \epsilon_p \rho_p H_p + (1 - \epsilon_p) \rho_c H_c \quad (36)$$

where H_p and H_c are the enthalpies of the plastic and the char, respectively. In order to account for the energy associated with the process of pyrolysis we must have

$$H_p = \left(\Delta H_f^{\circ} \right)_p + \int_{T_0}^T C_p dT \quad (37)$$

and

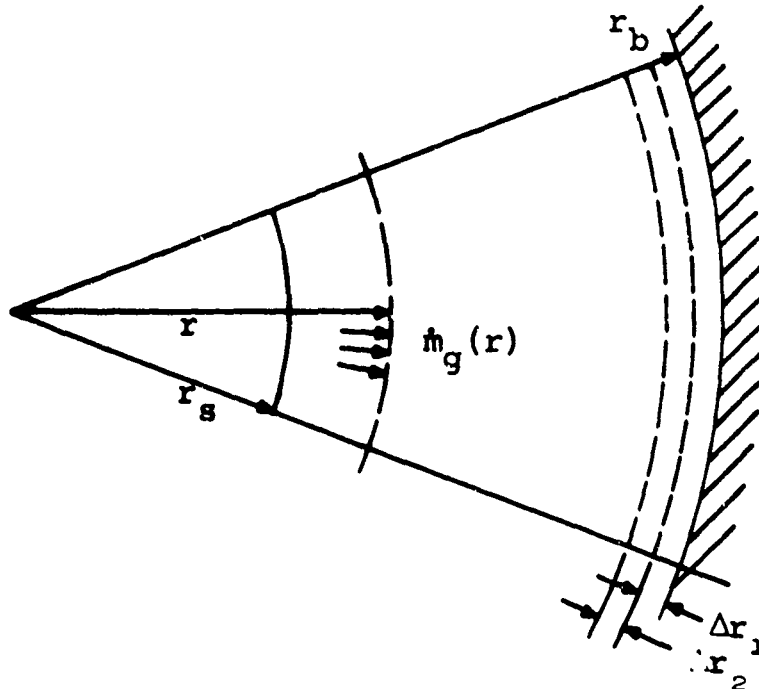
$$H_c = \left(\Delta H_f^{\circ} \right)_c + \int_{T_0}^T C_c dT \quad (38)$$

Implicit in the definition of char is the fact that both ρ_c and H_c must include the gaseous products of pyrolysis present in the matrix. (This is a small contribution to be sure, but the purist will insist on its inclusion.) Then, using Equation (36), we can work out the first term in Equation (34) as

$$r \frac{\partial(\rho H)}{\partial \theta} = r \left\{ \left[\rho_p \epsilon_p C_p + (1 - \epsilon_p) C_c \rho_c \right] \frac{\partial T}{\partial \theta} + \frac{(\rho_p H_p - \rho_c H_c)}{\rho_p - \rho_c} \left(\frac{\partial \rho}{\partial \theta} \right) \right\} \quad (39)$$

In deriving Equation (39), ρ_p and ρ_c have been assumed to be constants.

In order to evaluate the last term in Equation (34), consider an enlarged view of the region denoted as Section I in the sketch on page 24.



We seek an expression for the mass rate of flow of pyrolysis gas through any shell at r . Assume for the moment that pyrolysis can be occurring anywhere throughout the section and that the outer radius, r_b , is at an impermeable surface. The mass of gas crossing a cylindrical surface a distance Δr_1 from the back wall is

$$\left. \dot{m}_g \right|_{r=r_b - \Delta r_1} = 2\pi(r_b - \Delta r_1) \Delta r_1 \left(\frac{\partial \rho}{\partial \theta} \right)$$

Similarly, that crossing the surface a distance $\Delta r_1 + \Delta r_2$ from the back wall is

$$\left. \dot{m}_g \right|_{r=r_b - (\Delta r_1 + \Delta r_2)} = \left. \dot{m}_g \right|_{r=r_b - \Delta r_1} 2\pi \left[r_b - (\Delta r_1 + \Delta r_2) \right] \Delta r_2 \left(\frac{\partial \rho}{\partial \theta} \right)$$

If we proceed in this way, adding up the contributions of the annular rings Δr thick, until we reach the surface at r , and then allowing $\Delta r \rightarrow 0$ we have

$$\dot{m}_g(r) = 2\pi \int_r^{r_b} \left(\frac{\partial \rho}{\partial \theta} \right) r dr \quad (40)$$

Note that $\partial \rho / \partial \theta$ is itself a function of r . We are now prepared to write

$$\frac{1}{2\pi} \frac{\partial (\dot{m}_g H_g)}{\partial r} = \frac{\partial}{\partial r} \left[H_g \int_r^{r_o} \left(\frac{\partial \rho}{\partial \theta} \right) r dr \right] \quad (41)$$

The term representing conduction in Equation (34) is straightforward, provided one can define the conductivity, k , for the composite material. If the same gradient of temperature is assumed to exist, locally, in all the component materials of the composite, it is easy to show that the desired quantity is

$$k = \sum_j \epsilon_j k_j \quad (42)$$

where ϵ_j is the volume fraction of material j , and k_j is the thermal conductivity of material j . The assumption of equal local gradients is only strictly true for steady state, if the k_j 's are unequal. Better results would probably be obtained by using experimental data, when such data are available.

If all the terms appearing in Equation (34) are assembled and the result solved for $\partial T / \partial \theta$, there results

$$\frac{\partial T}{\partial \theta} = \frac{1}{C_t} \left\{ \frac{1}{r} \frac{\partial}{\partial r} \left(r k \frac{\partial T}{\partial r} \right) - \frac{1}{r} \frac{\partial}{\partial r} \left[H_g \int_r^{r_b} \left(\frac{\partial \rho}{\partial \theta} \right) r dr \right] - H_t \frac{\partial \rho}{\partial \theta} \right\} \quad (43)$$

where

$$c_t = \rho_p \epsilon_p c_p + (1 - \epsilon_p) \rho_c c_c \quad (44)$$

and

$$H_t = \frac{(\rho_p H_p - \rho_c H_c)}{\rho_p - \rho_c} \quad (45)$$

When ablation is occurring at the inner surface, the solution of Equation (43) by finite difference techniques is facilitated by transforming to a moving coordinate system fastened to the ablating surface.² Taking

$$\begin{aligned} x &= r - r_s \\ \theta' &= \theta \end{aligned} \quad (46)$$

and transforming Equation (43), there results

$$\begin{aligned} \left(\frac{\partial T}{\partial \theta'} \right)_x &= \frac{1}{c_t} \left\{ \frac{\partial}{\partial x} \left(k \frac{\partial T}{\partial x} \right) + \left[\frac{k}{(r_s + x)} + \left(\frac{\partial r_s}{\partial \theta'} \right) c_t \right] \frac{\partial T}{\partial x} \right. \\ &\quad - \frac{1}{(r_s + x)} \frac{\partial}{\partial x} \left[H_g \int_x^{r_s} \left(\frac{\partial \rho}{\partial \theta'} \right)_r (r_s + x) dx \right] \\ &\quad \left. - H_t \left(\frac{\partial \rho}{\partial \theta'} \right)_r \right\} \end{aligned} \quad (47)$$

Notice that the time derivative of temperature is taken at constant x , while the time derivative of density is at constant r . The reason for retaining the density term in this form will be discussed in Section 2.3.3

²The motives and considerations involved are discussed in Reference 1.

2.3.3 Thermophysical properties of a charring ablator

In order to effect a solution to Equation (47), thermophysical data of three different types are required. These are:

- (a) Effective thermal conductivities.
- (b) Density changes and decomposition rates.
- (c) Enthalpy-temperature relationships.

The conceptual difficulty with the apparent conductivity of a composite has already been mentioned. The most satisfactory determination of conductivity is from experiment, but this is a relatively difficult measurement to make. If the conductivities of the materials comprising the composite are strongly temperature dependent, the effective conductivity may depend on the heating rate. For most materials of interest, the properties of the virgin materials are fairly well-established, and the difficulty is mainly with partially or fully degraded material.

In general, the instantaneous rate of decomposition of phenolic-type plastics depends on both the temperature and the extent of prior decomposition. For example, Munson and Spindler, Reference 11, assume a decomposition law of the form

$$\frac{dp}{dt} = - (\rho - \rho_c)^n A \exp\left(-\frac{\Delta E}{RT}\right) \quad (48)$$

and choose the constants to fit experimental data on decomposition as well as possible. In dealing with nylon cloth-phenolic composite, Kratch, Hearne, and McChesney, Reference 12, assume that three parallel decompositions occur, each of which is expressed in the form of Equation (48). Using this, they are able to fit the decomposition rate data very closely.

It should be noted that Equation (48) (or its counterparts in a more elaborate decomposition model) applies to a point fixed in the decomposing material; that is, at some point in the ablating

body there exist some instantaneous values of ρ and T which will uniquely determine $\partial\rho/\partial\theta$. Therefore, the value resulting from Equation (48) represents the $(\partial\rho/\partial\theta)_r$ term appearing in Equation (47).

The enthalpies and specific heats of the virgin plastic and the char, as functions of temperature, can either be determined from direct calorimetric measurements or computed from data on the component molecules if such data are available. The enthalpy of the mixture of pyrolysis gases can be calculated, provided some additional assumptions regarding chemical and thermal state are made. It appears reasonable to assume that the gases achieve both thermal and chemical equilibrium with the char layer.

If the density of the material at any point and at any instant in time is known, the apparent fraction of undecomposed plastic, ϵ_p , can be calculated. It should be appreciated that ϵ_p is a convenient fiction that truly represents the state of affairs only at the values 0 and 1. It may be possible to establish the adequacy of the approximation by way of Equation (36), if enthalpy data are available for partially degraded material, as well as for virgin material and char.

One area of continuing effort on this program is a search for the requisite thermophysical data for the various materials of interest. It is hoped that analyses such as that outlined previously will stimulate the acquisition of the necessary material properties.

2.3.4 Surface chemical reactions

In order to establish a surface boundary condition for the internal conduction program, it is necessary to consider the requisite inputs and resultant outputs involved in a calculation of the surface state. At each time step, certain information is available from the internal conduction solution which may be used to

evaluate this surface state. Included are:

- (a) The rate at which pyrolysis gas is being supplied to the surface as a consequence of in-depth decomposition of resin (for a charring ablator).
- (b) A relation between the surface temperature and the surface-temperature derivative; for example, using the temperature of a node Δx below the surface, this relation is of the general form

$$\left. \frac{dT}{dx} \right)_w \approx \frac{T_w - T_{\Delta x}}{\Delta x} = f(T_w) \quad (49)$$

In general, several other required parameters are established either absolutely or through some known or calculated functional dependence. These parameters include:

- (a) The elemental composition of the char layer.
- (b) The elemental composition of the pyrolysis gas.
- (c) The elemental composition of the boundary-layer-edge gas.
- (d) The enthalpy of the boundary-layer-edge gas.
- (e) The incident radiation flux upon the wall.
- (f) Heat- and mass-transfer coefficients.
- (g) The blowing correction factor on the preceding.
- (h) The enthalpy of the char as a function of its temperature.
- (i) The enthalpy of the adjacent pyrolysis gas (immediately below the surface) as a function of its temperature.
- (j) The thermal conductivity of the char as a function of temperature.
- (k) The emissivity of the char as a function of temperature.

Some of the above parameters may be given explicitly as functions of time without further complicating the problem.

From this information it is necessary to establish the surface temperature and the char-removal rate. The present procedure at Viuya utilizes mass and energy balances plus an assumption of surface chemical equilibrium. In the following paragraphs the functional relations will be presented briefly, together with some sample results.

By performing an elemental mass balance on each of the I elements at the surface, it is possible to formulate an expression for the mass fractions of each of the elements contained in the gas immediately adjacent to the material surface. These relations are

$$\tilde{K}_{iw} = \frac{\frac{\dot{m}_g \tilde{K}_{ig}}{\rho_e^u C_M} + \frac{\dot{m}_c \tilde{K}_{ic}}{\rho_e^u C_M} + \tilde{K}_{ie}}{1 + B'} \quad (50)$$

where

$$B' = \frac{\dot{m}_g + \dot{m}_c}{\rho_e^u C_M} \quad (51)$$

for the case of no condensed-phase deposition or removal from the surface and equal effective binary diffusion coefficients within the boundary layer. Based on the presumed input information, the I equations of this type contain $I+1$ unknowns, \tilde{K}_{iw} and \dot{m}_c .

The energy balance given by Equation (33) can be written somewhat more generally (in the absence of particles) as

$$\left(k \frac{dT}{dx} \right)_{x=+0} = f(T_w) = \rho_e^u C_H \left[H_r - (1 + B') H_w \right] + \dot{m}_g H_g + \dot{m}_c H_c + q_{rad} - \sigma \epsilon T_w^4 \quad (52)$$

where the first equality is a consequence of the internal conduction solution. This equation introduces two new unknowns, namely, the enthalpy of the wall gas, H_w , and the wall or surface temperature, T_w .

The assumption of surface equilibrium, both among the gas species adjacent to the surface and between them and the surface material, introduces the final required relations. It is well-established that, given the elemental composition of a gas and its temperature and pressure, a definitive set of relations can be formulated to establish the state of the system. In the present case this would imply that

$$\text{Surface gaseous state} = f(\tilde{K}_{iw}, T_w, p) \quad (53)$$

using the requirement that gas phase equilibrium exists among the species at the surface. The requirement for equilibrium between the gas phase and the surface material has yet to be included. The introduction of this constraint demands the removal of one of the existing constraints in Equation (53). Consequently, we may write for the ablation problem

$$\text{Surface gaseous state} = f(\tilde{K}_{iw}, p) \quad (54)$$

or more specifically

$$H_w = \xi(\tilde{K}_{iw}, p) \quad (55)$$

$$T_w = f(\tilde{K}_{iw}, p) \quad (56)$$

Thus, a definitive set of relations exists in the $I+3$ unknowns, \tilde{K}_{iw} , T_w , H_w , and m_c , and the $I+3$ Equations (50), (52), (55), and (56).

The solution of the system of relations represented by Equation (54) has been programed at Vidya for solution on the IBM 7094 computer. The program has the capability of selecting the appropriate surface material from a list of possible candidates. For example, the exposed surface of a silica-phenolic ablator can be, under various conditions, either silicon carbide, carbon, liquid silicon, or silica. A sample of the output from this program for silica phenolic is shown in Table I. This sample computer output was selected to show the transition from one surface material to another as the char-removal rate varies at fixed pyrolysis gas efflux. The variation of surface temperature indicates why it has been discarded as an independent variable in these calculations.

The establishment of the surface boundary state has thus been reduced to an iteration based upon the selection of an initial char-recession rate, \dot{m}_C , evaluation of the elemental mass fraction of the surface gases, \tilde{K}_{iw} , with Equation (50), the establishment of the wall temperature and enthalpy through the use of the described computer program, and, finally, the checking of these values by use of the energy equation (Eq. (52)). The actual procedure for this iteration is based upon a simple Newton method approach.

The foregoing discussion has shown how a multidependent system has been reduced to a simple iteration based on a single parameter by use of a computer program, written at Vidya, for the evaluation of a surface equilibrium state of an ablating material. Because of the complete generality of the program, it is applicable to all material types, requiring only the knowledge of conventional thermodynamic properties as contained, for example, in Reference 13.

3. EXPERIMENTAL STUDIES

3.1 Introduction

The choice of a rocket-nozzle liner material requires a knowledge of the behavior of appropriate materials in the combustion

product environment. This knowledge must be supplied by both a theoretical treatment of the materials response and experimental materials testing. As indicated in Figure 1, the theoretical treatment requires appropriate input of basic data for a successful and accurate solution. Some of this input must be determined experimentally. Hence, in the experimental phases of this program, several areas in which data are currently lacking are being investigated. These areas include chemical reactions and particle impact as they affect surface erosion. The experimental effort is conveniently divided into two separate programs:

(1) The chemical-erosion program; the investigation of chemical effects in the erosion process and the development of a simple materials-testing technique.

(2) The particle-impact program; the investigation of the effects of particle impingement on erosion.

As indicated above, a secondary purpose of the chemical-erosion program is to investigate a relatively simple materials-testing technique. The usual materials-testing techniques have taken three general forms: full-scale rocket tests, small-scale rocket tests, and splash tests on materials samples. The last technique must be regarded as only qualitative since only a rough comparison between the performance of different materials is possible. With the advent of large rocket motors, full-scale rocket tests for materials evaluation become prohibitive. Small-scale rocket tests do not permit the flexibility of varying test parameters independently and are also relatively expensive. A flexible, inexpensive yet quantitative experimental materials-evaluation technique is therefore desirable, and its development is the subject of one part of the experimental effort.

The presentation which follows covers the areas of experimental activity during the third quarter of the project. In the chemical-erosion test program, 43 test firings which were a direct part of the program were performed during the report period. This

does not include a large number of checkout tests which were also run. These 43 tests included the firing of 24 nozzles of graphite, graphite phenolic, and silica phenolic and 16 heat-transfer and pressure-distribution calibration tests. This testing completed the program on Mixtures 4 and 5 (see Ref. 2). Testing will be continued for Mixtures 1-3 later in the next quarter. The program will be stopped in the early part of the quarter, however, to allow a preliminary test series in the particle-impact program as discussed below.

The effort in the particle-impact test program consisted of the definition and investigation of instrumentation, particularly for measurement of particle velocity, and the start of the setup for the program. The program effort for the immediate future will be the setup for and performance of a preliminary test series to get the "feel" of the program and to define problem areas, if any. If problems do come up, the appropriate fixes will be made while the chemical-erosion program is continued.

3.2 Chemical-Erosion Test Program

3.2.1 Introduction

The primary objective of the chemical-erosion test program is the determination of the effects of specific chemical reactions on the erosion of rocket liner materials. The results obtained, in addition to being of general importance, provide necessary guidance to the theoretical phase of the subject contract. A secondary objective is the definition of an inexpensive technique for the quantitative, as opposed to qualitative, evaluation of candidate materials for rocket nozzles. The technique is expected to be a powerful tool for the material fabricator and the nozzle designer.

The program, in brief, consists of an appropriate series of tests on ablative materials utilizing the five gas mixtures discussed in References 1 and 2. These gas mixtures closely approximate the temperature-enthalpy variation of a typical solid-propellant exhaust gas and range, chemically, from a duplication of the actual combustion products to a mixture of inert gases. The Vidya arc-plasma generator supplies the energy input to the gas mixtures for simulation of the rocket environment. The test materials are graphite, silica phenolic, and graphite phenolic. An axisymmetric-nozzle configuration is used for all tests. The heat transfer and pressure distributions for a nonablating wall of the same geometry as the test nozzle are determined with sets of heat-transfer calibration nozzles and pressure-distribution calibration nozzles.

Testing during the report period included 24 nozzle firings of graphite, graphite phenolic, and silica phenolic. Several heat-transfer and pressure-distribution calibration tests were also performed. The results of these tests are presented in the following sections. In addition to this effort which was a direct part of the chemical-erosion program, several checkout tests including nine graphite-nozzle firings were performed to eliminate a swirl component in the exit flow and to establish a high-confidence level in the test results. Because of unanticipated problems in eliminating the swirl, the anticipated completion of the chemical-erosion program by the end of this report period was not achieved. Approximately half of the program was completed, however; all tests with Mixtures 4 and 5 were performed. The chemical-erosion program effort will be reduced in the immediate future to allow an initial testing effort in the particle-impact test program. This change in emphasis is being made in order to get a feel for the problems, conduct, and nature of the results in the particle-impact program.

3.2.2 Facility modifications

Two significant facility modifications were made during the report period, one to eliminate the swirl component in the exit flow of the plasma generator and the other to improve the power supply capability of the facility. These modifications and additions are discussed below.

As presented in Reference 1, the discussion of the arc-plasma generator, arc stability and the integrity of the electrodes is maintained by inducing arc rotation with a solenoidal magnetic field. This arc rotation induces an undesirable angular velocity or swirl component in the flow that, under some conditions, can be quite significant. Tests performed early in the experimental program indicated that the swirl could be kept to an apparently acceptable level by introducing the primary gas tangentially in a direction counter to that induced by arc rotation. These tests were performed on flat-faced nylon disks placed normal to the plasma generator exit flow. The flow pattern indicated by the melted-nylon surface showed that the swirl could be brought down to a negligible level by using sonic or close to sonic jets for introducing the primary gas. This splash flow apparently was not a critical indicator of the presence of swirl, however, since close inspection of the throat entry of the first nozzle fired (Test No. 795, reported in Ref. 2) revealed a pattern that indicated the presence of a significant swirl component.

Further testing on eliminating the swirl was therefore begun early in this report period. The magnetic-field strength (which dictated the magnitude of the swirl component) was first reduced. At a field strength one-fourth of that usually used, the swirl as indicated in nozzle firings finally became negligible. Due to the low field strength, however, the plasma-generator operation was somewhat unstable - sufficiently so that operation at these conditions was unacceptable. Tangential injection of the secondary

gas-flow was then attempted with successful results. By injecting the secondary gas in a direction counter to the arc-induced rotation of the primary gas, the swirl was eliminated. No stability problems existed, since swirl elimination was done at the standard magnetic-field strength of 6000 gauss. The facility modification required to accomplish this was simply the fabrication of a new injection ring. The characteristics of the new ring are as follows: the angle of injection, the angle between a radial line from the plasma-generator centerline to the injection point and the direction of secondary gas-injection, is 42° ; 16 injection ports are used; and the injection jets are changeable to allow swirl elimination at different secondary-gas conditions.

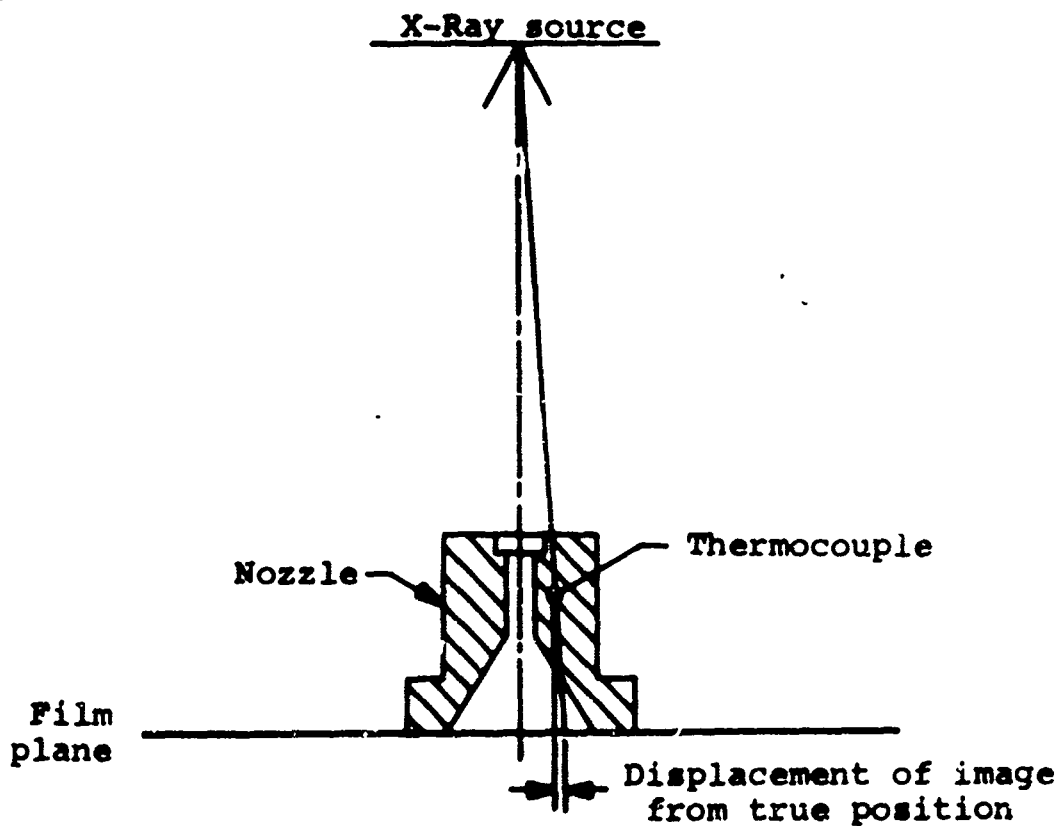
The increase in power supply capability mentioned above was the addition of a diesel generator to the power supply system. This was an in-house sponsored effort as part of Vidya's continuing program to increase the capabilities of the arc-plasma generator facility. The diesel unit was put into operation late in the report period and is capable of producing up to 500 kw of electrical power. A tandem hookup with the battery power-supply is used to eliminate the power droop inherent in the battery system alone. By "topping" the batteries with the diesel (the batteries and diesel in parallel) constant-power operation in excess of one megawatt is possible for extended operating times. The frequency at which tests can be performed has also been increased since the diesel unit is also used to recharge the battery supply at a much higher rate than previously possible. This new power-supply capability has already been used in the chemical-erosion test program for the intermediate-enthalpy test firings, the last firings that were performed during the quarterly report period.

3.2.3 Instrumentation and data reduction

The instrumentation and data-reduction techniques have been presented for the most part in References 1 and 2; these will not

be repeated here. Three particular areas, the X-ray technique for locating thermocouple positions in the test nozzles, the data-reduction computer programs, and the pyrometer measurement of surface temperature have not been discussed previously, however, and are presented below.

As discussed in Reference 2, the thermocouple instrumentation for measurement of the internal-temperature distributions in the test nozzles consists of very small diameter probes (0.035 inch). These probes are inserted into the test nozzles so that they follow approximately an isotherm in the region of the thermocouple junction in order to minimize the isotherm-distortion effect on the temperature readings. Because of the small hole size and large depth, drift of the drill during the hole-drilling operation can occur, particularly in the phenolics where there are material nonuniformities. The location of the bottom of the hole (the location of the thermocouple bead) may therefore not be where expected from measurement of the point of drill entry. X-ray photographs of each instrumented test nozzle are therefore taken at a commercial inspection laboratory. The technique for determining the thermocouple locations from the X-ray photographs is illustrated in the following sketch:



Correction must be made for the effect of the film plane and the thermocouple plane being non-coplanar. - the thermocouples being above the film plane. In order to make this correction, however, the following requirements must be met: the X-ray source must approximate a point, the film plane and the nozzle must be level, and the nozzle centerline must coincide with the normal from the film plane to the source. Unfortunately, commercial (as well as medical) X-ray equipment is not ordinarily set up within these requirements. A number of tests, measurements, and adjustments were therefore made on the equipment to allow the required precision measurements. The X-ray unit used has a small-source diameter, 0.5 mm. The distance from the source to the film plane was measured, and is 48 inches. The film plane was leveled and the "bulls-eye" on the film plane was precisely located. The required capability for accurately determining the thermocouple locations was therefore established.

A typical X-ray print is shown in Figure 4. The three dark lines which terminate approximately perpendicular to a radial line from the nozzle center are wires inserted in the probe holes to simulate the thermocouple probes. The dark rectangular patches are calibration shims of known length for length calibration and for a check on the accuracy of the calculated locations. One of the long shims is on the top surface of the nozzle and the other is on the film plane. By making the appropriate correction on the measured length of the top shim, the accuracy of the method is checked for each nozzle. A cylindrical plug is inserted into the tubular throat region to define accurately its location; without it, the definition of the throat surface is somewhat fuzzy.

For actual measurement, the X-ray negative is enlarged approximately three times. The film-plane shim is then used for a length calibration. The error in the calculated distance from the nozzle centerline to the probe tip is felt to be within ± 3 percent.

In order to speed up and simplify the data-reduction process for the nozzle firings and calibration tests, a number of computer-program additions and modifications were written during the report period for use on the Vidya IBM 1620 computer. A heat-flux calculation routine was added to the standard arc-plasma-generator data-reduction program for use in the reduction of the heat-transfer calibration test data. The average heat flux for each calibration nozzle segment is calculated and read out along with the standard arc-plasma-generator operating data.

A new program was written to check nozzle performance, to calculate instantaneous surface recession, and to calculate the instantaneous throat heat- and mass-transfer coefficients. The nozzle performance is checked by a calculation of the nozzle coefficient, C_n , (see Eq. (63), Ref. 2) for each test. Values not in an appropriate range indicate some problem in the test or in the data reduction (the values of C_n typically fall in the range 0.90 to 0.98). The instantaneous surface recession is calculated from the plenum pressure at a number of discrete times during a test by first calculating the throat area at each time, then the throat diameter obtained therefrom and, from this and the initial throat diameter, the surface recession (see pp 57 and 58, Ref. 2). The heat-transfer coefficient is calculated from the simplified Bartz equation (see Section 3.2.4.3) at each time for which surface recession is determined. The mass-transfer coefficient is calculated from the analogy between heat and mass transfer (see Section 3.2.4.4.4). The required transport properties are program inputs along with the thermodynamic data obtained from the arc-plasma-generator operation conditions. This program is also used as a check on the nozzle coefficient in the pressure distribution and heat-transfer calibration tests, and for calculation of heat-transfer coefficient in the heat-transfer tests.

An existing curve-fit program was modified for calculation of the instantaneous surface-recession rate. The calculated

values of surface recession are input to the program and a least squares fit of these points made. The slope of the fitted curve, the surface-recession rate, is calculated and read out together with the curve fit itself.

A computer program was also written to reduce the pre- and post-test nozzle profile data. The axial variation of nozzle diameter before and after test and the axial and circumferential variation of surface recession are calculated. The program input is the two sets of readings (before and after test) from four axial traverses, each 90° apart circumferentially, of a pivot arm-dial gauge micrometer.

A two-color optical pyrometer is being used in all nozzle firings in an attempt to get a direct indication of wall temperature. The pyrometer is set so that it looks into the nozzle throat at the throat wall. The two-color principle has the advantage of requiring no emissivity correction. The pyrometer senses the intensity at two discrete wavelengths and, from the ratio of the intensities, identifies the temperature corresponding to the black-body curve that has this intensity ratio. Since it senses temperature from a ratio of intensities rather than from an absolute intensity, the temperature readout is independent of emissivity if the object is radiating as a gray body. This type of pyrometer also has its disadvantages, however, the most serious being its sensitivity to stray radiation. Any stray radiation intercepted by the pyrometer will generally have different relative intensities than the object of interest and therefore will throw the pyrometer indication off. Because of this effect, the validity of the pyrometer data obtained by looking through the luminous arc-plasma stream is somewhat questionable.³

³Thermocouple instrumentation is, of course, also being used for determination of wall temperature. The pyrometer complements these measurements.

3.2.4 Test results and discussion

3.2.4.1 Introduction

The test program on Mixtures 4 and 5 was completed during the report period and the majority of results are presented herein. Because of incomplete data reduction on some tests at the time of writing, some results are necessarily omitted. Twenty-four test nozzles of graphite, graphite phenolic, and silica phenolic were fired as a direct part of the program. Appropriate heat-transfer and pressure-distribution calibration tests were also performed. The complete test program is presented in Table II. This table does not include a number of other tests, including nine graphite-nozzle firings, which were performed during the report period in preparation and checkout for the actual program. Note that the test program was altered somewhat from that originally presented in Reference 2. This was because Graphitite GX exhibited no surface recession at all with Mixture 5 (all inert gases) at the high-temperature condition, and therefore the two graphite-nozzle firings at less severe conditions were eliminated; two firings with ATJ graphite, Test Nos. 1000 and 1005, were substituted in their place to obtain a comparison between ATJ and Graphitite GX.

The test results are presented and discussed in the following sections. The experimental pressure distributions are presented in terms of the pressure ratio, p/p_0 , and are compared with one-dimensional isentropic theory. The experimental heat-transfer results are presented in the form of heat-transfer coefficients and are compared with the axial distribution predicted by the simplified Bartz method. The results of the nozzle firings are presented and discussed in detail. These results include post-test observations of surface condition, char depths, and surface recession, the time variation of surface recession and surface-recession rate, and internal and wall-surface temperature histories. Wherever possible, comparisons are made with theoretical predictions.

3.2.4.2 Pressure-distribution tests

Pressure-distribution calibration tests were run for the complete range of test conditions, nominally 2000° K to 3500° K, with both Mixtures 4 and 5. The description of the nozzles and conduct of tests is presented in References 1 and 2 and is not repeated here. The test results are presented in Figures 5 and 6 and are discussed below. The test conditions are indicated in each figure, as is the theoretical one-dimensional isentropic pressure distribution for each nozzle contour.

As seen from the figures, the experimental results are characterized by satisfactory agreement with one-dimensional isentropic theory in the convergent entry section and the divergent exit section of the nozzles (except as noted below) but, as expected, substantial disagreement, particularly for the 0.3-inch-diameter throat nozzle, is apparent in the tubular throat. As discussed in detail in Reference 2, this discrepancy is due to machining nonuniformities and boundary-layer growth. The predicted pressure drops based on consideration of these effects were presented in Reference 2 for the 0.3-and 0.4-inch-diameter throat nozzles and was calculated during this report period for the 0.5-inch throat nozzle. A comparison of the predicted values and the experimental results is presented in the table below:

D_* (in.)	Predicted pressure drop (psi)	Measured pressure drop (psi)
0.3	52	49 (956), 55 (955)
.4	21	10 (954), 11 (953), 10 (1030), 11 (1029)
.5	9	6 (952), 6 (951)

Numbers in parentheses indicate test numbers.

Discrepancies between measured and calculated values are felt to be due to the simplified approach used for predicting the pressure drop (Ref. 2), and to the small but progressive copper oxide build-up which occurs during each test causing a slight change in the nozzle-throat profile and therefore in the pressure drop.

Relatively poor agreement between experiment and theory is evident in the divergent exit section of the high-temperature condition tests on the 0.3- and 0.4-inch-diameter throat nozzles, Figures 5(a) and (b) and 6(a) and (b). No explanation for this discrepancy is apparent. The possibility of a calibration shift in the pressure transducer, a leak in the pressure line, and an obstruction in the line were all investigated with a negative result. Also, the 0.5-inch-throat nozzle run just prior to these tests (Figs. 5(c) and 6(c)) demonstrates favorable agreement as does the 0.4-inch nozzle run at the low-temperature condition later in the program (Figs. 5(d) and 6(d)).

Results at four of the nominal test conditions presented herein, Figures 5(a) and (b) and 6(a) and (b), were also presented in Reference 2. These four tests were repeated, however, since those tests presented in Reference 2 were run before the swirl component in the flow was eliminated. From a comparison of results, however, the swirl component was found to have had little effect on the pressure distribution.

3.2.4.3 Heat-transfer tests

As discussed in detail in Reference 2, the heat-transfer calibration nozzles consist of stacked calorimeter segments which form the desired nozzle contour. The average steady-state heat flux for each segment is determined from the known heated wall surface area of the segment and the heat rate into the segment calculated from the measured cooling-water flow rate and temperature rise. The reader is referred to Reference 2 for further details of the nozzle construction and data acquisition.

Tests were run on the 0.3-, 0.4-, and 0.5-inch-diameter throat nozzles with Mixtures 4 and 5 over the complete free-stream temperature range of the program, nominally, 2000° K to 3500° K. The experimental results for the high-temperature condition are presented in Figure 7 and 8. The data for the low-temperature tests, which were obtained on the 0.4-inch-diameter throat nozzle only, are in the data-reduction process and are not yet available for presentation herein. In each figure, the nozzle contour and segment positions are indicated for reference. The experimental results are presented in terms of the heat-transfer coefficient, defined as $q/(H_r - H_w)$, where the recovery enthalpy is approximated by the stagnation enthalpy (a reasonable approximation here). The wall enthalpy was calculated from the measured heat flux by considering the water side heat transfer and the heat transfer through the copper wall. In the variable area segments, the convergent and divergent sections, the experimental heat-transfer coefficients are plotted at the axial point where the predicted average heat-transfer coefficient for the segment is equal to the predicted local coefficient based on the simplified Bartz technique discussed below.

The predicted axial variation of heat-transfer coefficient is also included in each plot for reference. This variation was calculated from the simplified Bartz expression (Refs. 14 and 2),

$$\rho' u_e^2 C_{H'} = \frac{0.026 \rho' u_e}{Re^{0.2} Pr^{0.6}}$$

where the prime superscripts indicate evaluation of properties at the film enthalpy⁴.

⁴The reference enthalpy, as presented in Reference 2, is more frequently and, in this case, probably more appropriately used. The film enthalpy was used here, however, because of its simplicity and because it is the value suggested for use with the simplified Bartz equation, Reference 14. (Use of the reference enthalpy would result in a lower value of the predicted heat-transfer coefficient, by about 8 percent.)

$$H' = \frac{H_S + H_W}{2}$$

Values of Prandtl number and viscosity were estimated for the two gas mixtures and constant values of $Pr = 0.72$ and $\mu = 0.5 \times 10^{-4}$ lb/ft-sec were used throughout.

Returning now to the experimental results, Figures 7 and 8, the heat flux in the tubular throat region increases with increasing distance downstream in almost all cases. In most tests, a definite time effect in the value of the heat-transfer coefficient is apparent. This is felt to be due to the effect on the calculation of enthalpy of the power droop inherent in the battery power supply. The enthalpy calculation method currently being used is such that a somewhat lower than actual enthalpy is calculated when an appreciable power droop occurs as is the case at late test times. It is therefore felt that the early time results, the lower heat-transfer coefficient values, are more representative. With the addition of the new diesel power supply this problem will be eliminated in future tests.

The experimental results are consistently below the predicted heat-transfer coefficient in the throat region. A line which represents a 30-percent decrease in the predicted value is therefore included for reference. This value is seen to be in good agreement with experiment (considering, of course, that the early time results are felt to be more representative), except for one test, Test No. 948, Figure 7(a). No satisfactory explanation for the higher heat-transfer coefficient values in this

test has been found as yet. From the results of all other tests, however, it is apparent that the experimental throat heat-transfer coefficient is less than the simplified Bartz prediction by approximately 30 percent. This has also been observed in other investigations of nozzle heat transfer. The results presented in Reference 15 and also discussed in Reference 2 (see Fig. 8 of that reference, particularly) also exhibit experimental heat-transfer results which are almost exactly 30 percent below the simplified Bartz prediction in the throat region.

In the convergent entry section of the nozzle, the experimental heat-transfer coefficient is consistently above the predicted value. This reversal in the trend found in the throat region is felt to be due to radiation from the arc. This segment is able to "see" the arc and, therefore, will receive a radiant heat input from it. The radiant flux is apparently high enough to cause a significant increase in the apparent heat-transfer coefficient. No attempt to estimate this radiative flux and to compare it with the experimental results has been made as yet. Unfortunately, an adequate description of the radiation source, an electric arc rotating at high speed in an annular region, is rather difficult. Some effort at estimating this radiative flux is expected to be made in the next quarter, however.

The experimental heat-transfer coefficient in the divergent exit section of the nozzle is well below the simplified Bartz prediction in all cases. This trend is as expected from the comparison in the throat region. However, the experimental values are consistently less than 50 percent of the predicted values and not approximately 70 percent as found in the throat. These even lower coefficients are probably due to flow separation upstream of the nozzle exit. For all three nozzle sizes, the required static pressure at the exit for complete expansion is less than the actual static pressure of 1 atmosphere. Flow separation would therefore be expected upstream of the exit, with the attendant

lower heat transfer in the separated region. Actually, the point of separation should be further upstream from the exit with the 0.5-inch-diameter throat nozzle and move downstream in going first to the 0.4 nozzle and then to the 0.3. The discrepancy with theory should therefore become greater as the throat diameter increases, and this is indeed the case, as seen from the figures.⁵

3.2.4.4 Materials tests

3.2.4.4.1 Introduction

The test results for the 24 graphite, graphite phenolic, and silica phenolic nozzle firings performed during this report period as a direct part of the chemical-erosion program are presented below. Cut-away photographs of the fired nozzles are presented to reveal the nozzle material surface condition and, where applicable, char layer after test. Nozzle performance is presented in terms of instantaneous surface recession and surface-recession rate in the throat region. Wherever possible, comparison of the results with theoretically predicted recession is made. In most cases, the internal nozzle temperature distribution is also presented, and wall surface temperatures are indicated where possible. Again, appropriate comparisons are made with theory.

Before turning to these results, however, a brief discussion of the test program is appropriate. The test firings which were outlined previously in Table II complete the schedule with Mixtures 4 and 5. Mixture 4 is made up of the oxygen fraction in the combustion products of a typical solid propellant that is capable of reacting with a nozzle wall material, plus inert gases; Mixture 5 is made up of all inerts. Both gases, of course, simulate the temperature-enthalpy variation of the typical solid propellant. The reader is referred to References 1 and 2 for a complete

⁵ In all pressure-distribution calibration tests, the pressure tap in the exit cone was always upstream of the point where separation would be expected. The effect of separation, therefore, was not apparent in the pressure distribution results.

-2-

development of the simulation requirements and for the gas mixture analysis.

Tests were run over a range of total temperature and initial plenum pressure in order to allow the investigation of wall temperature and pressure on chemical reaction. The emphasis is on the high-temperature condition, $T_0 = 3500^{\circ}$ K, however, since this is the approximate total temperature for the combustion products of many solid propellants.

A 30-second firing duration was used in almost all tests. In the two silica phenolic tests at the high-temperature condition, this time was shortened to approximately 20 seconds because of the large surface recession. Also in some tests premature arc-out occurred because of the inherent power supply droop being unusually excessive.

The instantaneous surface recession was calculated as a function of time for each nozzle firing from the time variation of plenum pressure. This method is discussed in detail in Reference 2. As indicated in Reference 2, the expansion cone in the test nozzles was felt to be limiting the usefulness of this technique due to the movement of the minimum diameter point, the actual nozzle throat, into the expansion cone as surface recession progressed. This difficulty was eliminated by eliminating the exit expansion cone so that the nozzle exit was the downstream end of the tubular throat. After this fix, the agreement between measured and calculated values of surface recession in the tubular throat was excellent, as is apparent from the results presented below. The new test nozzle geometry is presented in Figure 9. The internal nozzle wall profile both before and after test was determined by traversing the wall with a pivot-arm, dial-gauge micrometer. Local surface recession, both axial and circumferential, was determined from these measurements.

In most of the firings, the internal wall temperature history was measured. Thermocouples were located in the tubular

throat region at three radial positions in a plane normal to the nozzle centerline. The instrumentation technique is discussed in Reference 2. The actual thermocouple positions were measured by X-ray photography as discussed in Section 3 2.3. Originally, instrumentation in three planes in the tubular throat region was anticipated. This was abandoned, however, since preliminary firings indicated little axial variation of temperature and because of the fairly sizeable time and cost involved in instrumentating the nozzles. For further details of the overall testing technique and other background material, the reader is referred to References 1 and 2.

3.2.4.4.2 Post-test observations

The response of the test nozzles to the simulated rocket environment was assessed in part from post-test inspection and measurements. These results are presented in this section. Photographs of the fired nozzles after being sectioned are presented for most tests. These photographs reveal the extent and uniformity of surface recession, the surface condition, and, in the case of the phenolics, the char layer. The values of surface recession determined from pre- and post-test measurements are also presented for the tubular throat region. In the case of the phenolics, the char depths are also discussed.

The cut-away photographs of the test nozzles after firing are shown in Figures 10 to 17. The original nozzle contour before firing is indicated in each figure for reference. These contours are only approximate because of alignment and enlargement problems in the photographic printing of the composite of nozzle cut-away and original contour. Photographs are not presented for three of the fired nozzles. In Test No. 959 no surface recession occurred and, since Test No. 958 was identical to it, it was decided to save the nozzle for a future test. In Test No. 999, graphite phenolic nozzle E34, a catastrophic delamination occurred, apparently

because of improper curing. Tests on the nozzle are now under way to check this out, and therefore it is not available for inclusion here. The test conditions to which nozzle E23 were exposed, Test Nos. 1017 and 1020, were somewhat erratic, and therefore the results are questionable and are now under study. Because of this, no photograph is presented for this nozzle.

The results available from post-test observations and measurement are discussed from the photographs and from tabulations of the measured surface recessions. Surface recession results are discussed first, followed by other observations and analysis of surface condition and char depth.

Absolutely no surface recession occurs with graphite, both Graphitite GX and ATJ, in the inert gas environment, Mixture 5, Figures 14 and 15. Remember that this environment closely duplicates all aspects of the solid-propellant rocket environment except its chemical character. Also for graphite phenolic, Figure 16, the same behavior is observed.

For Mixture 4, which contains oxygen, surface recession does occur with graphite and graphite phenolic, and its magnitude is dependent on temperature level, Figures 10(a) to (e) and 12(a) to (c). The measured surface recession for graphite (Graphitite GX) is summarized as follows:

Graphite, Graphitite GX

Nominal Total Temperature (°K)	Surface Recession (mils)	
	Mixture 4	Mixture 5
3500	74 (939), 73 (940), 47 (997)	0 (957 & 958)
2750	37 (1039)	*
2000	0 (1023)	*

Numbers in parentheses indicate test numbers.

* No firings performed since no surface recession occurred in the most severe case.

All results presented are for approximately the same firing times, 30 seconds (see Table II). The comparison between Mixtures 4 and 5 indicates that the surface recession for Mixture 4 is due solely to chemical reaction. The decrease in surface recession with decreasing temperature is apparently due to kinetic control of the oxygen-carbon reaction at the wall for the two lower temperatures. This is discussed further in Section 3.2.4.4.4 following. One test at the high-temperature level produced results which are out of line with the others (see the above table). The test setup was identical and the test conditions were almost identical for the three firings. No obvious explanation for the discrepancy is readily apparent. The nozzles could have come from different billets but, hopefully, no such variation between billets would actually occur.

As mentioned previously, the graphite phenolic nozzles exhibited no surface recession with Mixture 5, the inert environment, Figure 16. In fact, a buildup of the solid-resin pyrolysis products on the surface actually resulted in a slight decrease in throat diameter. A significant weight loss occurs, however, due to the resin decomposition and out-gassing. The surface recession for graphite phenolic in the oxidizing environment, Mixture 4, is significant over the entire temperature range, Figure 12. The measured surface recession is summarized below:

Graphite Phenolic, MX 4500

Nominal Total Temperature (°K)	Surface Recession (mils)	
	Mixture 4	Mixture 5*
3500	64 (1001)	0 (1006)
2750	54 (1040)	0 (1043)
2000	4 ² (10 ² 4)	0 (1026 & 1028)

Numbers in parentheses indicate test numbers.

*Actually a slight surface buildup occurred in each case.

For Mixture 4, the surface recession remains high with decreasing temperature, probably due to the large number of sites available for chemical reaction in the "porous" char surface. Again the comparison between Mixtures 4 and 5 points out the significance of chemical reaction - here it is also apparently the only contributor to surface recession.

The performance of silica phenolic is dependent on both the temperature level and the gas environment, Figures 13 and 17. Surface recession is due to "melting" of the silica and to chemical reaction with the wall. A comparison of the measured surface recession is presented below:

Silica Phenolic, MX2600

Nominal Total Temperature (°K)	Surface Recession (mils)	
	Mixture 4	Mixture 5
3500	160 (941) (19 seconds)	124 (960) (21 seconds)
2750	60 (1038)	0 (1042)
2000	-	0 (1031)

Numbers in parentheses indicate test numbers.

Note that the recession at the high-temperature condition is for firing times less than 30 seconds. At this condition, the surface recession is very large - completely out of line with the performance of the other materials. Its degradation at high temperature is largely due to the "melting" of the silica. With Mixture 5, the recession is apparently due to melting only, whereas with Mixture 4 chemical reaction is also contributing to the surface recession. At the intermediate temperature condition, no melting

appears to occur and, from a comparison of the results for the two gas environments, the surface recession with Mixture 4 is apparently due to chemical reaction only.

The test results presented and discussed above demonstrate conclusively the importance of chemical reaction in the erosion of nozzle wall materials. The surface recession for graphite and graphite phenolic was apparently due solely to chemical reaction. No recession occurred in the inert environment. Chemical reaction was also a significant contributor to recession for silica phenolic.

Post-test inspection of the nozzle surface condition and appearance was made in each case and revealed some interesting behavior. In the case of the phenolics the surface condition and appearance are dependent on both the chemical nature of the gas environment and the temperature. With Mixture 4, both the graphite phenolic and silica phenolic exhibit a "clean" surface, apparently produced by the reaction of the oxygen with the carbon produced in resin pyrolysis. With Mixture 5, however, the carbon products remain in the interstices of the char surface, apparently because of the absence of oxygen in the free stream.

The nozzle wall for graphite phenolic with Mixture 4 becomes more rough and pitted as the total temperature is decreased, Figure 12. Local delaminations are also apparent, particularly in the tubular throat region. With Mixture 5, the graphite phenolic nozzles exhibit a smooth wall surface, Figure 16. Some local delaminations are also apparent, however. In all cases with Mixture 4, the axial and circumferential variation of recession was somewhat nonuniform.

For silica phenolic and Mixture 4 at high total temperature, resolidified silica or a resolidified silicon compound is apparent on the surface, particularly in the subsonic entry region, Figure 13(a). This is not evident in the nozzle fired with Mixture 5, Figure 17(a). One possible explanation for this is that in Mixture 5 the carbon due to resin pyrolysis reacts with the

molten silica to form carbon monoxide and silicon. The silicon, due to its low viscosity, is then removed mechanically upon formation. In Mixture 4, however, the available carbon reacts with the free-stream oxygen more readily than with the silica which apparently is sufficiently viscous to resist at least to some extent the shear forces which tend to remove it from the nozzle.

In the graphite nozzle firings in which the surface recession is appreciable, the surface is somewhat rough, indicating preferred sites for chemical reaction, for example, Figures 10 and 11. This is particularly apparent in the ATJ nozzle. In all cases where surface recession occurred, the minimum recession occurred at the entry to the tubular throat.

The cut-away photographs also reveal the char layer in the phenolic nozzles, Figures 12, 13, 16, and 17. The char depths are considerably greater for graphite phenolic than for silica phenolic, about a factor of 3 for the 30 second firing times. This is reasonable, considering the lower thermal diffusivity of the silica phenolic. The lower diffusivity results in a steeper temperature gradient, and therefore the resin pyrolysis temperature occurs closer to the wall surface.

In all firings, the char depth in the subsonic entry section is the same as, or greater than, that in the tubular throat region. This seems somewhat anomalous at first sight since the heat flux is much lower in the entry region. This behavior can be explained, however, by considering the two-dimensional effect associated with the small diameter throat and the insensitivity of internal temperature to changes in heat flux for low-conductivity materials. The char depth is also nearly independent of total temperature, for example, Figure 12. Again, this is due to the low conductivity of the phenolic materials which results in only small internal temperature changes with significant changes in surface heat flux.

In the silica phenolic nozzles, a definite resin decomposition region is apparent next to the char layer. This appears as

a lighter region in the photographs, Figures 13 and 17, and is approximately half the thickness of the char layer. No such region is apparent with the graphite phenolic.

The char-virgin plastic interface recession rate was also assessed for the silica phenolic nozzle firings from the thermocouple data and the post-test measurements of the nozzles. These results are discussed in Section 3.2.4.4.5.

3.2.4.4.3 Surface recession and surface-recession rate histories

The discussions of the preceding section were based strictly on before- and after-the-fact observations and measurements. During the firings in which surface recession occurred, however, the surface recession rate varied over wide ranges. A significant transient time exists early in each firing before a quasi-steady recession condition is achieved. Also, once the quasi-steady condition is reached, the surface-recession rate remains a variable, decreasing with time due to the decreasing heat- and mass-transfer coefficients associated with the increasing throat diameter. These considerations are particularly important in making general conclusions regarding surface recession and surface-recession rate. An average surface-recession rate calculated only from pre- and post-test measurements and the firing duration can be quite misleading if it is applied for firing times or geometries other than those for which the results were obtained. A knowledge of the instantaneous surface recession and surface-recession rate is therefore important. These results are presented in this section.

The surface recession and surface-recession rate are plotted against time in Figures 18 to 22 for all nozzle firings in which surface recession occurred at the high-temperature condition.⁶ The data for the firings at the intermediate and low

⁶As discussed briefly in Section 3.2.3 and in detail in Reference 2, the instantaneous surface recession and surface-recession rate are calculated from the measured plenum pressure decay.

temperature conditions were in the reduction process at the time of writing and therefore are not presented. All plots are to the same scale for ready comparison. The test conditions, including, where available, the wall surface temperature indicated by the pyrometer, and a comparison of the measured and calculated final throat diameter, are presented in each figure. The agreement between these throat diameters is good in every case. The results presented are therefore felt to represent closely the actual instantaneous variation of surface recession and surface-recession rate in the tubular throat region during each firing.

The theoretically predicted surface-recession rate is also presented for the graphite-nozzle firings with Mixture 4. The prediction technique and the comparison of the experimental results with prediction are discussed in Section 3.2.4.4.4 following.

The surface recession exhibits two different types of variation with time, depending on the time during the firing, Figures 18 to 22. At early times, both the surface recession and the surface-recession rate are increasing. At later times the surface recession is of course still increasing but the surface-recession rate is decreasing. The early time variation is a transient response to the step change in conditions at the start of firing. After the nozzle has accommodated itself to this step change, the second, later-time variation is apparent. The surface recession in this regime may be termed quasi-steady in that, even though the surface-recession rate is decreasing, this variation occurs only after the equilibration to the step change in conditions at the start of firing has occurred. Note that as much as 18 seconds may be required to reach the quasi-steady condition for the range of conditions and materials presented.

The surface-recession rates for all graphite-nozzle firings at the high-temperature condition are presented in Figure 23. The three Graphitite GX graphite firings at high pressure,

Test Nos. 939, 940, and 997, show reasonable agreement and, as indicated in Figure 24, fall within a fairly narrow band with a maximum surface-recession rate at early time of about 4 mils/sec and a minimum at the end of the firings of something higher than 1.5 mils/sec. In Figure 23, the ATJ graphite firing, Test No. 1000, is seen to have a quite different trend than the three Graphitite GX firings at the same nominal conditions. The surface-recession rate is lower at early times but levels off such that at the end of the firings it has a recession rate comparable to that of the three Graphitite GX firings. This early-time behavior is probably due, at least in part, to the higher thermal diffusivity of ATJ graphite at low temperature which, in turn, results in a lower wall surface temperature at early times. If the firings had not been terminated at 30 seconds, it appears that the recession rate for ATJ would be higher than that for Graphitite GX at times in excess of 30 seconds.

By decreasing the initial plenum pressure, (Test No. 998, Fig. 23), and therefore the heat- and mass-transfer coefficients and probably the wall temperature, a significant decrease in surface-recession rate occurs - better than a factor of 2 for a reduction in initial plenum pressure from 300 psia to 177 psia. The rate is also almost invariant with time, at least for the 30 seconds of firing duration. A further discussion of the comparison between these results is presented in the discussion of the predicted surface-recession rates, Section 3.2.4.4.4.

A comparison of the recession rates for graphite, graphite phenolic, and silica phenolic is presented in Figure 24 for the high-temperature and high-pressure condition. The graphite tests are presented by the cross-hatched band which encloses the results of the three Graphitite GX firings. The surface-recession rate for graphite phenolic falls within the band for the graphite firings except at late times when it is lower. At early times it is close to the upper limit for graphite. The silica phenolic recession rate is much higher than that for graphite and graphite phenolic. The

maximum value is about 12.5 mils/sec after 5 seconds of firing, the start of quasi-steady conditions. Note that a quasi-steady recession is achieved much earlier in the firing than for the other materials, because of its low thermal diffusivity. At 1.5 seconds, the recession rate is about twice that of the other materials, 7.5 mils/sec. In this firing, the throat diameter increased by a factor of better than 2, and therefore the area by better than 4, over the 20-second firing duration.

The results of an early firing on an ATJ graphite nozzle, Test No. 795, were presented in Reference 2. This firing was performed before the swirl component was eliminated from the arc-plasma-generator flow, however. The surface-recession rate for this firing is presented in Figure 25, together with the results of the recent ATJ firing, Test No. 1000. The early test before swirl was eliminated has a substantially higher surface-recession rate. This is felt to be due to the higher heat- and mass-transfer coefficients caused by swirl in the early test. The higher heat-transfer coefficient can be expected to result in a higher wall temperature at an earlier time in the firing, thus contributing to a higher surface-recession rate when the recession is reaction rate controlled. The higher mass-transfer coefficient results in more oxygen available for reaction at the surface and, therefore, a higher surface-recession rate when recession is diffusion rate controlled, that is, when equilibrium obtains. The slightly more severe chamber conditions in the earlier firing is a further contribution to the discrepancy in the results. The primary contributor, however, is felt to be the swirl.

3.2.4.4 Comparison of experiment with theoretical prediction

Before discussing the comparison of experimental surface recession rate with prediction, a brief discussion of the meaning of such a comparison is in order. The predicted surface

recession rate is based on the assumption that all the reactant, in this case oxygen, that diffuses to the wall reacts with it (no mechanical erosion is considered). This rate of diffusion of the reactant is given by the term

$$\rho_e u_e C_M \left[(K_r)_e - (K_r)_w \right]$$

At low enough wall temperatures, however, the surface recession is influenced by the reaction rate as well as the diffusion rate. In this case, not all the reactant available does, in fact, react. The experimental surface recession will then be lower than that predicted. The reaction rate is generally expressible by an equation of the Arrhenius form $k_j p_j = A_j p_j e^{-B_j/T}$, where the units are the same as those for the diffusion rate and where p_j and T are the partial pressure of reactant and the temperature. Note that the reaction-rate constant is particularly sensitive to temperature in that it appears as an exponential. In summary, the surface recession corresponding to diffusion rate control represents the upper bound on chemical erosion. A surface recession lower than this value indicates that the wall reaction is reaction rate (kinetically) controlled.

An experimental surface-recession rate higher than the equilibrium prediction indicates mechanical erosion, since our prediction is the upper limit on chemical reaction. Mechanical erosion actually can present an insidious complication in comparing experiment with prediction since any additional surface recession due to mechanical erosion tends to compensate for any decrease due to kinetic control of the surface reaction. Fortunately, no mechanical erosion of graphite or graphite phenolic occurred with Mixture 5 and, therefore, would not be expected in the chemically reactive mixtures, unless, however, the chemical reaction weakens the wall material and allows mechanical erosion to take place. An appropriate test program could, of course,

determine the presence or absence of mechanical erosion in the chemical environment, but is not included as part of the chemical-erosion program.

The derivation of the surface-recession rate prediction was presented in Reference 2 and is not repeated here. The mass-transfer coefficient required for the calculation was determined from the simplified Bartz equation for heat-transfer coefficient and the analogy between heat and mass transfer

$$\rho' u_e^{C_M} = \rho' u_e^{C_H} Le^{2/3}$$

where Le is the Lewis number. Unity was chosen as a convenient yet reasonable value for the Lewis number. From the heat-transfer calibration tests, it was found that the experimental heat-transfer coefficient was approximately 30 percent lower than the Bartz prediction. The experimental mass-transfer coefficient should therefore also be lower than the predicted value by the same amount. Two theoretical lines are indicated on the plots, one based on the Bartz predicted mass-transfer coefficient and the other 30 percent lower, which is based on the heat-transfer calibration tests. The lower curve should be closer to fact for chemical equilibrium with the wall.

The experimental surface-recession rate is compared with the predicted value for all graphite-nozzle firings in Figure 18 and is presented in composite form for the three Graphitite GX firings at the same nominal conditions in Figure 26. At these conditions, the experimental recession rate is slightly lower than the predicted value, departing by the largest amount at late times when the pressure and possibly the wall temperature have

decreased due to the enlargement of the throat.⁷ At early times, therefore, the surface recession is very nearly, if not completely, controlled by the diffusion of oxygen to the wall. At the late times, however, the wall temperature apparently dropped to a sufficiently low level that the reaction at the wall is reaction rate influenced.

At the high-temperature and low-pressure condition, Figure 18(d), the experimental surface-recession rate is less than half the predicted rate. The final throat diameter (and mass-flow rate) and, therefore, the final free-stream conditions in this firing are almost identical to that at the end of firing in the tests of Figures 18(a) to (c). The difference in surface-recession rate and the comparison with theory between these two conditions must therefore be due to a difference in wall temperature. Because of the lower heat-transfer coefficient in the firing of Figure 18(d), the wall temperature would not be expected to be as high as that for the firings of Figures 18(a) to (c).⁸ A lower reaction rate and therefore a lower surface-recession rate obtains. The comparison of the two cases will be investigated further with the one-moving-boundary computer program.

Kinetic or reaction rate influence is also evident in the two graphite firings at lower total temperature for which the data reductions are not complete. In the lowest total temperature

⁷Although a decrease in wall temperature at later times in a firing seems a bit out of order at first glance, it is indeed a real possibility. With a sufficiently large decrease in heat-transfer coefficient, a decrease in wall temperature can occur in the absence of surface recession, even though the wall recovery enthalpy remains constant. The one-moving-boundary computer program will be used to checkout this possibility for the case of chemical erosion. Note that, as seen in the plots of temperature history, Figure 27, the wall temperature indicated by the pyrometer does decrease with firing time at late times.

⁸Note that the pyrometer indication of wall temperature does not indicate a substantial difference between the two conditions. However, as indicated previously, there is some doubt in the validity of the pyrometer indications due to the effects of looking through the luminous exit flow.

firing, nominally 2000° K, the experimental surface-recession rate is zero, whereas the predicted value is a constant at approximately 6.5 mils/sec. The wall temperature in this case will of course be substantially less than 2000° K.

In the ATJ graphite firing, Figure 19, the experimental surface-recession rate is somewhat below the predicted rate, but approaches it at late times. This low-recession rate is somewhat surprising when one considers the lower density and, therefore the expected availability of additional sites for chemical reaction. However, it may be due to the higher thermal diffusivity of ATJ graphite at low temperature; a low wall temperature⁸ or possibly a longer time to achieve a high wall temperature may result. (Again, this will be investigated further with the one-moving-boundary computer program.) Due to the apparently low temperature, the surface recession is reaction rate influenced, at least up to the 30-second test time of this firing.

In summary, reaction-rate control of surface recession is evident, at least to some extent, in all of the graphite-nozzle firings. The magnitude of this effect is apparently associated primarily with the wall surface temperature rather than the pressure. At the high wall temperatures experienced at early firing times in the high total temperature, high pressure firings, the surface recession is close to being, if not completely, diffusion rate controlled.

Further analysis of the graphite firing results will be performed with the one-moving-boundary computer program, Section 2.2, to investigate further the observed experimental behavior of the surface recession and to verify the explanations presented above. The charring-ablator computer program will also be used for an analysis of the experimental results with graphite phenolic and, conversely, the experimental results will be used as a guide

⁸Note that in this case, the pyrometer reading does support this explanation of the behavior.

in determining reaction-rate data for use in the program. These further analyses will also include an investigation of the experimentally determined internal temperature distributions discussed below.

3.2.4.4.5 Temperature histories

The internal wall temperature histories and the internal temperature distributions obtained therefrom provide a further means of assessing the chemical behavior at the nozzle wall. This information can be used in the determination of wall surface temperature, which of course affects chemical reaction, and in comparisons with the theoretical prediction techniques being developed in the program. The temperature data required to provide this information were obtained by thermocouple instrumentation at three radial locations in a plane perpendicular to the nozzle centerline that also goes through the center of the tubular throat (see Ref. 2). Three radial-thermocouple locations were used so that the internal temperature distribution at any time in the firing is available.

The interpretation of the results is complicated by surface recession, the distance between the thermocouples and heated surface continually decreasing, decreasing wall heat flux with time, and, in the case of the phenolics, the existence of a char layer and pyrolysis region between the heated surface and the thermocouples. Because of these problems it is difficult in most cases to obtain definitive information on surface temperature and chemical reaction directly. The primary utility of the experimental distributions is in comparison of the experimental results with those obtained by the theoretical prediction techniques being developed under the contract. From these comparisons, together of course with all other available experimental information, the appropriate chemical-reaction rate data for use in the program can be determined. Since the one-moving-boundary computer program (Section 2.2) has only recently become available and the charring

ablater computer program (Section 2.3) is not yet complete, the available temperature history results have not yet been put to full use. The pertinent information now available from the temperature histories is presented and discussed below.

The internal wall temperature histories for all nozzle materials and both test gas mixtures are presented in Figures 27 to 32, at the high-temperature test condition. The results for the lower temperature conditions are in the data-reduction process and, therefore, are not presented. The test conditions and the locations of the thermocouples are indicated in each figure.¹⁰ The pyrometer indication of the wall temperature variation is also indicated where available. For the graphite-nozzle firings with Mixture 5 (no surface recession and no chemical reaction), the experimental results are compared with the theoretical temperature histories calculated with the computer program of Reference 16. This program solves the differential equation for the transient heating of an axisymmetric body by a finite difference technique. The program allows variable material thermal properties and time-dependent heat-transfer coefficient and recovery enthalpy. The heat-transfer coefficient used was that predicted by the Bartz equation but reduced by 30 percent, as is indicated appropriate by the heat-transfer calibration tests.

In the comparison of the experimental and theoretical temperature histories in the nonablating, nonreacting cases, Figure 30, agreement in both magnitude and trend for the complete firing in both tests is surprisingly good. The discrepancy between experiment and theory never exceeds 90° K. This occurs at high temperature, and part of it is due to the inadequacy of the linear temperature-millivolt thermocouple calibration assumed for data reduction. From this agreement with theory, it appears

¹⁰Thermocouple locations in parentheses indicate nominal values; an X-ray photograph of this nozzle was not taken due to an oversight.

that the thermocouple instrumentation technique does indeed yield reliable results.

The theoretical surface temperatures are also presented in the figures and, based on the agreement at the internal points, they should be accurate. Unfortunately, no pyrometer data are available for comparison purposes in these tests. The pyrometer was set up but no reading was obtained. Based on the theoretical surface temperature, no reading is exactly what would be expected - the pyrometer was set on a high-temperature scale that had a minimum temperature above the maximum value indicated by the theoretical prediction (this scale setting was chosen because it was the one found to be correct for the same conditions with Mixture 4).

In the comparable firing with Mixture 4 where both surface recession and chemical reaction occurred, Figure 27(a), the temperature at the nearest-to-the surface location rose considerably faster than that at the same location with Mixture 5. This response is felt to be due both to the chemical reaction occurring at the wall and to the surface recession associated with it. Thermocouple 1 in the firing of Figure 27(b) did not appear to be functioning properly and, therefore, should not be used in interpreting the results.

In both of these firings, Figure 27, the pyrometer indicates a decreasing surface temperature in the time ranges for which information is available. If the pyrometer is indeed indicating the actual variation, it may well be due to the decreasing heat- and mass-transfer coefficient with surface recession. This trend will be checked further with the one-moving-boundary computer program.

The graphite phenolic firings with Mixtures 4 and 5, Figures 28 and 31, appear similar in the time ranges for which comparable results are available. Unfortunately, one thermocouple failed in each firing. With Mixture 4, the thermocouple closest to the surface reached a temperature quite close to the surface

temperature as indicated by the pyrometer; at the end of test, Thermocouple 1 is only about 0.040 inch from the surface.

The motion of the char-virgin plastic interface is not apparent in any of the thermocouple traces in either of the graphite phenolic firings. No abrupt changes in temperature occurred to signal the passing of the interface. However, both Thermocouples 1 and 2 were in the char layer at the end of the firings.

The silica phenolic-nozzle firings, Figures 29 and 32, are particularly interesting, at least academically. In these firings, the motion of the char-virgin plastic interface is identifiable from the thermocouple histories and Thermocouple 1 was overtaken by surface recession. From Figures 29 and 32, the variation of temperature with time is characterized by a slow increase in temperature followed by an abrupt rise to high temperature.¹¹ This is particularly evident in Figure 29 for both Thermocouples 1 and 2. This sharp increase in temperature occurs within the first 1/8-inch of the nozzle wall. The start of the abrupt rise probably signals the end of resin pyrolysis and the start of the motion of the char surface across the thermocouple location. Post-test measurements of the extent of the char layer support this interpretation. Pyrolysis, therefore, is seen to occur at temperatures less than 800° K (1000° F).

In both firings, the surface recession overtook Thermocouple 1. The point in time at which this occurred is indicated in the figures and was determined from the calculated surface recession and the thermocouple locations. The probable temperature history up to this point is indicated in Figure 29.

The motion of the char-virgin plastic interface as determined from the temperature histories is presented in Figures 33 and 34. The plot on the left is the recession referenced to the

¹¹ In Figure 32, Thermocouple 2 started an abrupt rise in temperature about 1/2 second after the firing was terminated, followed almost immediately by a drop in temperature as cool-down started.

location of the wall surface at the start of the firing. The right-hand plot shows the variation of char depth determined from the surface recession and the recession of the char-virgin plastic interface. The recession determined from measurement of the interface location in the sliced nozzles after firing is also indicated. The agreement between the value determined from post-test measurement and that predicted from the temperature history information is good. The variation of char depth with time is characterized by a rise to a value which is invariant with time in the latter part of the firing. This depth for the firing with Mixture 4 is approximately 110 mils and with Mixture 5 about 140 mils. This compares with the measured char depths of 110 mils and 120 mils, respectively.

3.2.5 Summary

The results of a number of nozzle firings of typical solid-propellant rocket-motor exposed materials were presented and discussed, together with the results of appropriate heat-transfer and pressure-distribution calibration tests. These tests were performed as part of the chemical-erosion program and represent almost half of the testing to be performed under this phase. The nozzle materials were Graphitite GX graphite, ATJ graphite, MX4500 graphite phenolic, and MX2600 silica phenolic. Tests were performed with Mixtures 4 and 5, both mixtures simulating all aspects of the rocket environment except its chemical nature. Mixture 5 is completely inert chemically, whereas Mixture 4 contains an amount of oxygen equivalent to that in typical solid-propellant combustion products that is able to react. The nominal range of test conditions was a gas total temperature from 3500° K to 2000° K and a plenum pressure from 300 psia on down.

The nozzle-firing results were presented in terms of the measured total surface recession, the time variation of surface recession and surface-recession rate, and the internal temperature histories. Cut-away photographs of most nozzles were also presented and the pertinent information available from them was

discussed. This included surface condition, uniformity of surface recession, and the char layer. Wherever possible, the experimental results were compared with theory. The calibration test results were presented in the form of the heat-transfer coefficient axial distribution and the pressure-ratio axial distribution. Again, comparisons were made with theory.

A summary of the results and conclusions is presented below:

(1) Chemical reaction appeared to be the only contributor to surface recession for graphite and graphite phenolic; no surface recession occurred with these materials in the inert environment, Mixture 5, whereas the surface recession was significant with Mixture 4, the chemically reactive environment.

(2) From the comparison of experiment and theory, the influence of both species diffusion and chemical kinetics on surface recession was apparent for the range of test conditions.

(3) At high total temperature, the performance of graphite and graphite phenolic are comparable; at lower temperatures graphite was superior, however.

(4) Silica phenolic exhibited severe surface recession at high total temperature due to "melting;" chemical reaction was also a contributor in the chemically-reactive environment, Mixture 4.

(5) Where comparison was made, the experimental internal-temperature histories agreed favorably with the theoretical prediction.

(6) The measured heat-transfer coefficient was approximately 30 percent below the simplified Bartz prediction and in agreement with results of other similar tests.

The analysis of the results is incomplete in that not all test data have been reduced at the time of writing and not all theoretical comparison were able to be made. This will be performed during the next quarterly period.

3.3 Particle-Impact Test Program

3.3.1 Introduction

The particle-impact program is an experimental investigation of the effects of metal-oxide particle impingement on the behavior of rocket-nozzle materials. The wall response and particle behavior associated with particle impact is assessed in terms of the individual mechanisms associated with or influenced by particle impingement. These mechanisms include:

- kinetic energy transfer
- internal thermal energy transfer
- chemical reaction
- shear due to impact
- radiative heat transfer
- boundary-layer perturbations which affect:
 - convective heat transfer
 - mass transfer
 - shear

The importance of these mechanisms and their contribution to nozzle-material wall degradation will be studied by two complementary and concurrent approaches. These are the definitive measurements of both the material response and the particle variables and behavior before, during, and after impact, and the observation and measurement of material response in pairs of tests that are identical except for the absence of particles in one and their presence in the other.

Testing in the particle-impact program will be started early in the next quarterly period, and before the testing in the chemical-erosion program (on Mixtures 1-3) is completed. These tests will take the form of checkout runs to obtain a general feel for the conduct of the particle-impact tests and to define

any problem areas which will require further effort before launching into the primary testing phase of the program. If any such problems do come up, the chemical-erosion program will be picked up again while the appropriate fixes are being made. The effort in the program during the third quarter consisted of the definition and investigation of instrumentation, particularly for measurement of particle velocity, and the start of the test setup for the program.

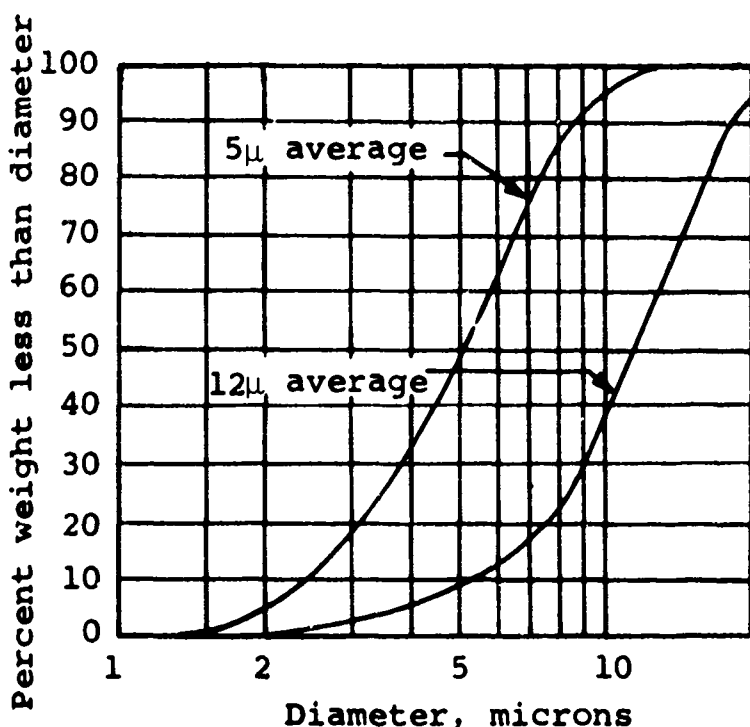
3.3.2 Testing technique

Testing will be conducted under controlled laboratory conditions which closely duplicate the solid-propellant rocket combustion products environment including the presence of solid particles or liquid droplets of aluminum oxide. The Vidya arc-plasma generator provides the combustion products environment. The test sections are typical rocket-nozzle wall materials, graphite, graphite phenolic, silica phenolic, and tungsten. The exit flow from the arc-plasma generator impinges on the test sections which are placed downstream of the plasma-generator exit plane at any desired preset angle of attack. Briefly, this outlines the test technique and procedure; the details are presented below.

The description of the arc-plasma generator and its operating characteristics is presented in References 1 and 2 and is not discussed further here. The reader is referred to these references for this background information. The test gas to be used in the program for most tests is Mixture 4.¹² A number of tests are also anticipated with Mixture 5, which consists of inert gases only, in order to investigate particle effects in the absence of chemical reaction of the wall material with the

¹²Again, the reader is referred to References 1 and 2 for the background information on the test gas mixtures.

test gas. The particles are high purity alumina, Al_2O_3 , Norton Company electronic grade Alundum, 99.65 percent Al_2O_3 minimum. Two different particle sizes will be used - one for which the average size on a weight basis is 12 microns, and the other 5 microns. The size distributions provided by the manufacturer are indicated in the following sketch:



The distributions and individual particle shapes will also be checked by electron microscope. Since the test procedure results in all particles in the exit flow impacting on the test sample, mass loadings typical of the complete solid-propellant rocket exhaust are not necessary. Small mass loadings in the test case are therefore required to simulate the larger mass loadings of a rocket exhaust. Small mass loadings are also being used to allow the identification of individual particle behavior and effects.

The test section materials are graphite, graphite phenolic, silica phenolic, and tungsten. Tungsten, in addition to being of

interest as a rocket nozzle material, also eliminates the effects of surface recession and chemical reaction in assessing particle-impact effects. The test section configuration is a 3-inch-diameter disk, the thickness of which will be varied between 1/4- and 3/4-inch to allow some control of the transient temperature response of the test sections. The plasma-generator exit flow impacting on the test sections will be circular in cross section with a diameter of 1/2-inch or slightly greater.

The test variables are the test section material, the wall temperature, the plasma-generator operating conditions, the particle temperature, the particle velocity, the particle size, the particle mass loading, the angle of incidence of the particles on the test section, and the chemical nature of the exhaust gas. Some of these variables are, of course, interdependent and all are discussed below. The test section materials, except for tungsten, are the same as those used in the chemical-erosion program, Graphitite GX graphite (Basic Carbon Corporation), MX4500 graphite phenolic (Fiberite Corporation) and, MX2600 silica phenolic (Fiberite Corporation).

The wall surface temperature is important in terms of chemical effects, both between particle and wall and test gas and wall, and can be expected to influence the impact behavior of the particle. A range in wall temperatures which covers those representative of aft closure, throat, and expansion cone is anticipated. Wall temperature control will be accomplished by variation of test section thickness as discussed above, changes in plasma-generator operating conditions, and variation of the exposure time of the test section to the particle-free exit stream before particles are introduced.

The particle temperature is tied directly to the plasma-generator operating conditions. The residence time of the particles in the plenum chamber will be sufficient for temperature equilibration with the test gas. The anticipated particle temperature

range is 2000°K to 3500° K. The particle velocity is dictated by the plasma-generator operating conditions and by the exit nozzle size. Particle velocities up to 6000 ft/sec are anticipated. The particle mass loading will be varied from 0 to 2 percent of the total exit mass flow, but most tests will be performed at low mass loadings to allow individual particle effects to be assessed. The angle of incidence between the particles and the test section surface will be varied from 10° to 40°. As discussed previously, tests will be performed with a chemical reactive test gas, Mixture 4, and an inert test gas, Mixture 5, both of which closely duplicate the thermodynamic properties of the solid-propellant rocket combustion products. The inert gas allows the assessment of particle effects in the absence of chemical reaction, whereas the chemically reactive gas simulates both the chemical and thermodynamic environment.

3.3.3 Facility modification and instrumentation

The general facility setup in preparation for the particle-impact-program has, for the most part, been completed in that the similar activities in preparation for the chemical-erosion program are applicable here. The additional facility modifications and the instrumentation techniques are discussed below.

A new plenum extension ring, shown in Figure 35, will be used for injection of particles in the plenum chamber of the arc-plasma generator downstream of the arc zone. This ring also accommodates the secondary gas injection. There are eight particle injection ports uniformly spaced to help insure proper distribution of particles in the exit flow. The particles are injected in a direction counter to the rotation imparted to the primary gas by the arc rotation. This, together with the secondary gas injection, cancels the arc-induced rotation and also helps to insure good mixing and a uniform particle distribution.

An existing particle hopper will be used for particle injection and flow control. This unit is capable of handling powders with a size distribution for which the average particle size is as low as 5 microns. The hopper has been checked out with the 12 micron particles for the range of mass loadings to be used and found to perform properly. Operation with 5 micron particles is possible only at very low mass loadings. Particle metering and control is accomplished by a variable speed vibrator. The vibrator causes the particles to fall from a storage cannister, through an orifice, and into a carrier-gas pickup chamber. The carrier gas, in this case a portion of the secondary injection gas, delivers the particles to the plenum chamber in eight separate feed tubes as discussed above.

Due to the nature of the program, a number of specialized instrumentation techniques are required in addition to the standard data-acquisition methods. A water-cooled calorimeter will be used in place of the test section to determine the average cold-wall heat flux over the central 3/4-inch-diameter surface of the test sections. The calorimeter will have a 3-inch guard ring enclosing its 3/4-inch sensing surface to duplicate the test section geometry. The radiative contribution to the total heat flux will be assessed with a HyCal asymptotic radiometer with a 15° view angle and a calibrated output to 500 Btu/ft²-sec. Some of the test sections will contain thermocouple instrumentation to assist in assessing the test section response and the wall surface temperature. The instrumentation technique will be the same as that used in the chemical-erosion program.

The response of the test slab to the simulated rocket environment will be photographed with a high-speed Traid motion picture camera at a film speed of 1000 frames per second. Real time color motion pictures and post-test still photographs will also be taken to further evaluate test section response. In some

of the tests, additional analyses of the slab response and particle behavior will be performed with an electron microscope for particle identification, sizing, and counting. This service will be performed by Allied Space Products, Inc., of Palo Alto, under Vidya supervision.

Particle-velocity measurements, both before and after impact, will be made with an Abtronics image-intensifier camera as discussed in Reference 2. With this technique, the particle velocities are measured by a streak photography method in which individual particles should be identifiable. The capability of the camera system in performing this task was checked out further during the report period. Calculations were made of the energy that is available from a single particle for energizing the camera system, and of the accuracies obtainable. The calculations indicated a marginal probability of the camera being able to "see" the particles and allowing a determination of particle velocity from the resultant photograph with an error no greater than about ± 5 percent. Since the capabilities do appear marginal, it has been decided to perform the preliminary tests using the camera on a short-term demonstration basis. In the preliminary tests, only a one-dimensional view of the particle stream will be taken in order to eliminate a complicated split-image optics system. A second Traid high-speed motion picture camera will also view the same field as the image-intensifier camera to obtain a continuous record of the particle stream both before and after impact.

An indication of particle temperatures will be attempted with the two-color pyrometer discussed previously. Measurements will be made both before and after impact to assess the energy lost in impaction by those particles that are reflected from the surface. The use of an infrared pyrometer is also anticipated. The pyrometer measurements will be made on the stream both with and without particles to checkout the validity of the pyrometer

indications. Color-densitometer analyses of photographs of the particle-laden stream as discussed in Reference 2 will also be made to determine particle temperatures.

Particle sampling for determination of the size distribution in the high-temperature exit flow of the plasma generator still remains a problem. An estimate of the size distribution of particles adhering to the test samples will be made as part of the electron microscope examination of the slab surface. This, of course, may not be representative of the free stream distribution due to the possibility of a selective adherence of the particles to the surface; particles in one size range may, for the most part, adhere to the surface, whereas in another size range they may tend to reflect. Other sampling techniques are under investigation and include sampling by collecting the complete exit flow over a period of time and "quick action" sampling using a nylon disk or right-circular cylinder. In the latter case, particles are collected by adherence to the nylon pickup which has been softened by the high-temperature environment itself. In this method the exposure of the pickup to the stream would be for a very short time only, 1 second or less. This technique will be attempted in the preliminary test program and the results analyzed to determine the validity of the distribution obtained from it.

3.3.4 Test preparations

Preparations for the actual performance of the test program were begun during the report period. Fortunately, much of the setup and checkout of the program had already been completed, in that much of that required for the particle-impact program is common to the chemical-erosion program. The progress in the additional facility and instrumentation preparations are discussed below.

The new plenum extension ring was designed (Fig. 35) and fabrication begun. The particle-feed unit was checked out and found to operate satisfactorily for the range of test conditions to be used in the program. The test section materials for the preliminary program are on hand. The excess materials from the nozzle fabrication in the chemical-erosion program are being used. The required test section holder and actuating system are a part of the arc-plasma generator facility and required no modification to accommodate the program.

The necessary arrangements for use of the Abtronics image-intensifier camera on a demonstration basis were made. The basic camera will be used with "breadboard" controls to allow variation of the camera operation to obtain an optimum camera system for photographing the particles. Overhaul and checkout of the Traid high-speed motion picture camera recently obtained through the government surplus list for use on this program was begun. The second Traid camera is ready for operation. The flat-face heat-flux calorimeter is a facility item and therefore ready for use. The guard ring around it required to duplicate the test section geometry will be fabricated shortly. The HyCal radiometer has been placed on order for delivery by the end of the first month of the quarter.

Preliminary testing for checkout of the complete setup will take place late in the first month of the quarterly period. The preliminary test program is expected to be completed at the end of the first week of the second month.

The future effort will be dictated by the results of the preliminary test program. If no unusual problems arise, the particle-impact program is expected to be continued to completion. Otherwise the chemical-erosion program will be resumed while appropriate fixes are made.

REFERENCES

1. Lundberg, R. E., Schaefer, J. W., and McCuen, P. A.: A Study of Solid-Propellant Rocket Motor Exposed Materials Behavior, First Quarterly Progress Report for the period 1 June 1963 through 31 August 1963. Air Force Rept. No. RTD-TDR-63-1038, Sept. 1963.
2. McCuen, P. A., Lundberg, R. E., and Schaefer, J. W.: A Study of Solid-Propellant Rocket Motor Exposed Materials Behavior, Second Quarterly Progress Report for the period 1 September 1963 through 30 November 1963. Air Force Rept. No. RTD-TDR-63-1076, Dec. 1963.
3. Lees, L.: Convective Heat Transfer With Mass Addition and Chemical Reactions, Third AGARD Combustion and Propulsion Colloquium, May 1958.
4. Kendall, R. M., and Rindal, R. A.: Analytical Evaluation of Rocket Nozzle Ablation, presented at the AIAA Solid-Propellant Rocket Conference, Jan. 29-31, 1964, Palo Alto, Calif.
5. Lowrie, R., et al.: Research on Physical and Chemical Principles Affecting High Temperature Materials for Rocket Nozzles, Semiannual Progress Report, Contract No. DA-30-0690-ORD-2787, Union Carbide Research Institute, Jun. 30, 1961.
6. Lowrie, R., et al.: Research on Physical and Chemical Principles Affecting High Temperature Materials for Rocket Nozzles, Semiannual Progress Report, Contract No. DA-30-069-ORD-2787, Union Carbide Research Institute, Dec. 31, 1961.
7. Walker, P. L., Jr., Rusinke, F. Jr., and Austin, L. G.: Gas Reactions of Carbon, Advances in Catalysis, v. II, p. 133, Academic Press, New York (1959).
8. Gulbransen, E. A. and Andrew, K. F.: Reaction of CO_2 With Pure Artificial Graphite at Temperatures of 5000° to 900° C, Ind. Eng. Chem. v. 44, p. 1048 (1952).
9. Armington, A. F.: Ph.D. Dissertation, Pennsylvania State University (1960).
10. Blyholder, G. D., and Eyring, H.: Kinetics of the Steam-Carbon Reaction, Jour. Phys. Chem., v. 61, 1957, p. 682.

11. Munson, T. R. and Spindler, R. J.: Transient Thermal Behavior of Decomposing Materials, Part I: General Theory and Application to Convective Heating, presented at the IAS 30th Annual Meeting, New York, Jan. 22-24, 1962.
12. Kratsch, K. M., Hearne, L. F., and McChesney, H. R.: Thermal Performance of Heat Shield Composites During Planetary Entry, presented at the AIAA-NASA National Meeting, Palo Alto, Calif., Sept. 30-Oct. 1, 1963.
13. Dergazarian, T. E., et al.: JANAF Thermochemical Tables. Thermal Laboratory, The Dow Chemical Co., Midland, Mich., Dec. 1960 and supplements to date.
14. Bartz, D. R.: A Simple Equation for Rapid Estimation of Rocket Nozzle Convective Heat-Transfer Coefficients, Jet Propulsion, pp. 49-51, Jan. 1957.
15. Massier, P. F., et al.: A Heat Transfer and Fluid Mechanics, Jet Propulsion Laboratory Research Summary No. 36-11, for the period Aug. 1, 1961 to Oct. 1, 1961, pp. 80-89.
16. Rindal, R. A. and Covert, M.: Axisymmetric Transient-Temperature Prediction Program, Vidya Technical Note 53/C-TN-16, Aug. 30, 1961.

TABLE I.- EXAMPLE OF OUTPUT FROM THE ABLATING SURFACE THERMO-CHEMICAL EQUILIBRIA COMPUTER PROGRAM.

ABLATING SURFACE THERMO-CHEMICAL EQUILIBRIA

PRESSURE,ATM	2.72000E 00	SURF.TEMP,K	2745.48	ENTH,CAL/GM	-4.41839E 01
MDOT P.G./CM	2.00000E-01	MOL.WEIGHT	29.1972	MW(1+M/CM)	-2.29756E 02
MDOT CHAR/CM	4.00000E 00	SPEC.HEAT	0.31396	SURFACE	02SI* 5
- - - - MOLE FRACTION - SPECIE - - - -					
0.0000000 CH	0.0000007 CHN	0.0000165 CH0	0.0000000 CH2		
0.0000000 CH3	0.0000000 CH4	0.0000000 CN	0.0221183 CO2		
0.0000000 C2H2	0.0000000 C3	0.0000000 C3H	0.0000000 C2H		
0.0000000 C4H	0.0143897 H	0.0000006 HN	0.0014957 HO		
0.0000000 HS1	0.0000000 H4SI	0.0000004 N	0.0001025 NO		
0.0000000 NO2	0.0000000 NS1	0.0000000 N20	0.0001054 O		
0.0000161 O2	0.0000046 SI	0.0000000 S12	0.0019607 O2SI		
0.3958704 CO	0.1256270 H2	0.0469780 H20	0.0853577 N2		
0.3059578 OS1					
PRESSURE,ATM	2.72000E 00	SURF.TEMP,K	2718.20	ENTH,CAL/GM	-6.32286E 01
MDOT P.G./CM	2.00000E-01	MOL.WEIGHT	30.6408	MW(1+M/CM)	-4.55246E 02
MDOT CHAR/CM	6.00000E 00	SPEC.HEAT	0.29580	SURFACE	02SI* 5
- - - - MOLE FRACTION - SPECIE - - - -					
0.0000000 CH	0.0000008 CHN	0.0000154 CH0	0.0000000 CH2		
0.0000000 CH3	0.0000000 CH4	0.0000000 CN	0.0169409 CO2		
0.0000000 C2H2	0.0000000 C3	0.0000000 C3H	0.0000000 C2H		
0.0000000 C4H	0.0117938 H	0.0000004 HN	0.0008443 HO		
0.0000000 HS1	0.0000000 H4SI	0.0000003 N	0.0000542 NO		
0.0000000 NO2	0.0000000 NS1	0.0000000 N20	0.0000595 O		
0.0000064 O2	0.0000064 SI	0.0000000 S12	0.0015461 O2SI		
0.4249789 CO	0.1032327 H2	0.0272893 H20	0.0647067 N2		
0.3485236 OS1					
PRESSURE,ATM	2.72000E 00	SURF.TEMP,K	2644.91	ENTH,CAL/GM	-9.52692E 01
MDOT P.G./CM	2.00000E-01	MOL.WEIGHT	32.1360	MW(1+M/CM)	-1.06701E 03
MDOT CHAR/CM	1.00000E 01	SPEC.HEAT	0.27851	SURFACE	02SI* 5
- - - - MOLE FRACTION - SPECIE - - - -					
0.0000000 CH	0.0000013 CHN	0.0000129 CH0	0.0000000 CH2		
0.0000000 CH3	0.0000000 CH4	0.0000000 CN	0.0080698 CO2		
0.0000000 C2H2	0.0000000 C3	0.0000000 C3H	0.0000000 C2H		
0.0000000 C4H	0.0077538 H	0.0000002 HN	0.0002494 HO		
0.0000000 HS1	0.0000000 H4SI	0.0000001 N	0.0000142 NO		
0.0000000 NO2	0.0000000 NS1	0.0000000 N20	0.0000154 O		
0.0000008 O2	0.0000103 SI	0.0000000 S12	0.0007958 O2SI		
0.4575991 CO	0.0782428 H2	0.0100161 H20	0.0436389 N2		
0.3925796 OS1					

ABLATING SURFACE THERMO-CHEMICAL EQUILIBRIA

PRESSURE,ATM	2.72000E 00	SURF.TEMP,K	2191.50	ENTH,CAL/GM	5.95612E 00
MDOT P.G./CM	4.00000E-01	MOL.WEIGHT	16.7465	MW(1+M/CM)	8.39813E 00
MDOT CHAR/CM	10.00000E-03	SPEC.HEAT	0.53985	SURFACE	02SI* 8
- - - - MOLE FRACTION - SPECIE - - -					
0.000000 CH	0.0000019 CHN	0.0000076 CHO	0.0000000 CH2		
0.000000 CH3	0.0000000 CH4	0.0900000 CN	0.0152161 CO2		
0.000000 C2H2	0.0000000 C3	0.0000000 C3H	0.0000000 C2H		
0.000000 C4H	0.0020477 H	0.0000000 HN	0.0000788 HO		
0.000000 HS1	0.0000000 H4SI	0.0000000 N	0.0000024 NO		
0.000000 NO2	0.0000000 NS1	0.0000000 N2O	0.0000003 O		
0.000000 O2	0.0000000 SI	0.0000000 SI2	0.0000045 O2SI		
0.2923518 CO	0.4000892 H2	0.1079133 H2O	0.1806630 N2		
0.0016238 OS1					
PRESSURE,ATM	2.72000E 00	SURF.TEMP,K	2324.41	ENTH,CAL/GM	7.81842E 01
MDOT P.G./CM	4.00000E-01	MOL.WEIGHT	16.9731	MW(1+M/CM)	1.13367E 02
MDOT CHAR/CM	5.00000E-02	SPEC.HEAT	0.53626	SURFACE	02SI* 4
- - - - MOLE FRACTION - SPECIE - - -					
0.0000000 CH	0.0000018 CHN	0.0000102 CHO	0.0000000 CH2		
0.0000000 CH3	0.0000000 CH4	0.0000000 CN	0.0143096 CO2		
0.0000000 C2H2	0.0000000 C3	0.0000000 C3H	0.0000000 C2H		
0.0000000 C4H	0.0041486 H	0.0000001 HN	0.0001940 HO		
0.0000000 HS1	0.0000000 H4SI	0.0000000 N	0.0000070 NO		
0.0000000 NO2	0.0000000 NS1	0.0000000 N2O	0.0000013 O		
0.0000001 O2	0.0000000 SI	0.0000000 SI2	0.0000257 O2SI		
0.2957008 CO	0.3931121 H2	0.1064358 H2O	0.1780540 N2		
0.0079986 OS1					
PRESSURE,ATM	2.72000E 00	SURF.TEMP,K	2385.53	ENTH,CAL/GM	1.06596E 02
MDOT P.G./CM	4.00000E-01	MOL.WEIGHT	17.2575	MW(1+M/CM)	1.59893E 02
MDOT CHAR/CM	1.00000E-01	SPEC.HEAT	0.52861	SURFACE	02SI* 4
- - - - MOLE FRACTION - SPECIE - - -					
0.0000000 CH	0.0000018 CHN	0.0000116 CHO	0.0000000 CH2		
0.0000000 CH3	0.0000000 CH4	0.0000000 CN	0.0139588 CO2		
0.0000000 C2H2	0.0000000 C3	0.0000000 C3H	0.0000000 C2H		
0.0000000 C4H	0.0055637 H	0.0000002 HN	0.0002804 HO		
0.0000000 HS1	0.0000000 H4SI	0.0000000 N	0.0000110 NO		
0.0000000 NO2	0.0000000 NS1	0.0000000 N2O	0.0000026 O		
0.0000003 O2	0.0000000 SI	0.0000000 SI2	0.0000533 O2SI		
0.2991946 CO	0.3861750 H2	0.1040248 H2O	0.1750012 N2		
0.0157202 OS1					

ABALATING SURFACE THERMO-CHEMICAL EQUILIBRIA

PRESSURE,ATM	2.72000E 00	SURF.TEMP,K	2447.66	ENTH,CAL/GM	1.27244E 02
MDOT P.G./CM	4.00000E-01	MOL.WEIGHT	17.8068	MW(1+M/CM)	2.03590E 02
MDOT CHAR/CM	2.00000E-01	SPEC.HEAT	0.51295	SURFACE	O2SI* 4
- - - - MOLE FRACTION - SPECIE - - - -					
0.0000000 CH	0.0000018 CHN	0.0000132 CHU	0.0000000 CH2		
0.0000000 CH3	0.0000000 CH4	0.0000000 CN	0.0136321 CO2		
0.0000000 C2H2	0.0000000 C3	0.0000000 C3H	0.0000000 C2H		
0.0000000 C4H	0.0073328 H	0.0000002 HN	0.0003932 HO		
0.0000000 HS1	0.0000000 H4SI	0.0000000 N	0.0000165 NU		
0.0000000 NO2	0.0000000 NS1	0.0000000 N2O	0.0000050 O		
0.0000005 O2	0.0000001 SI	0.0000000 SI2	0.0001078 O2SI		
0.3056521 CO	0.3739429 H2	0.0992097 H2O	0.1692827 N2		
0.0304091 OS1					
PRESSURE,ATM	2.72000E 00	SURF.TEMP,K	2508.25	ENTH,CAL/GM	1.32274E 02
MDOT P.G./CM	4.00000E-01	MOL.WEIGHT	18.8166	MW(1+M/CM)	2.38093E 02
MDOT CHAR/CM	4.00000E-01	SPEC.HEAT	0.48522	SURFACE	O2SI* 4
- - - - MOLE FRACTION - SPECIE - - - -					
0.0000000 CH	0.0000018 CHN	0.0000149 CHO	0.0000000 CH2		
0.0000000 CH3	0.0000000 CH4	0.0000000 CN	0.0132976 CO2		
0.0000000 C2H2	0.0000000 C3	0.0000000 C3H	0.0000000 C2H		
0.0000000 C4H	0.0093411 H	0.0000003 HN	0.0005193 HO		
0.0000000 HS1	0.0000000 H4SI	0.0000001 N	0.0000231 NO		
0.0000000 NO2	0.0000000 NS1	0.0000000 N2O	0.0000088 O		
0.0000009 O2	0.0000004 SI	0.0000000 SI2	0.0002064 O2SI		
0.3173353 CO	0.3527691 H2	0.0903566 H2O	0.1590020 N2		
0.0571220 OS1					
PRESSURE,ATM	2.72000E 00	SURF.TEMP,K	2541.11	ENTH,CAL/GM	1.24593E 02
MDOT P.G./CM	4.00000E-01	MOL.WEIGHT	19.7176	MW(1+M/CM)	2.49185E 02
MDOT CHAR/CM	6.00000E-01	SPEC.HEAT	0.46239	SURFACE	O2SI* 4
- - - - MOLE FRACTION - SPECIE - - - -					
0.0000000 CH	0.0000019 CHN	0.0000159 CHO	0.0000000 CH2		
0.0000000 CH3	0.0000000 CH4	0.0000000 CN	0.0130509 CO2		
0.0000000 C2H2	0.0000000 C3	0.0000000 C3H	0.0000000 C2H		
0.0000000 C4H	0.0104806 H	0.0000004 HN	0.0005828 HO		
0.0000000 HS1	0.0000000 H4SI	0.0000001 N	0.0000268 NO		
0.0000000 NO2	0.0000000 NS1	0.0000000 N2O	0.0000116 O		
0.0000012 O2	0.0000006 SI	0.0000000 SI2	0.0002896 O2SI		
0.3277504 CO	0.3344700 H2	0.0825563 H2O	0.1499513 N2		
0.0000094 OS1					

ABLATING SURFACE THERMO-CHEMICAL EQUILIBRIA

PRESSURE,ATM	2.72000E 00	SURF.TEMP,K	2576.90	ENTH,CAL/GM	1.02127E 02
MDOT P.G./CM	4.00000E-01	MOL.WEIGHT	21.2527	HW(1+H/CM)	2.45105E 02
MDOT CHAR/CM	1.00000E 00	SPEC.HEAT	0.42758	SURFACE	02SI* 4
- - - - MOLE FRACTION - SPECIE - - -					
0.0000000 CH	0.0000019 CHN	0.0000171 CHO	0.0000000 CH2		
0.0000000 CH3	0.0000000 CH4	0.0000000 CN	0.0125714 CO2		
0.0000000 C2H2	0.0000000 C3	0.0000000 C3H	0.0000000 C2H		
0.0000000 C4H	0.0116111 H	0.0000004 HN	0.0006225 HO		
0.0000000 HSI	0.0000000 H4SI	0.0000001 N	0.0000295 NO		
0.0000000 NO2	0.0000000 NSI	0.0000000 N2O	0.0000150 O		
0.0000014 O2	0.0000012 SI	0.0000000 S12	0.0004144 O2SI		
0.3456076 CO	0.3038944 H2	0.0695342 H2O	0.1346853 N2		
0.1209921 OS1					
PRESSURE,ATM	2.72000E 00	SURF.TEMP,K	2607.67	ENTH,CAL/GM	5.19700E 01
MDOT P.G./CM	4.00000E-01	MOL.WEIGHT	24.0231	HW(1+H/CM)	1.76698E 02
MDOT CHAR/CM	2.00000E 00	SPEC.HEAT	0.37556	SURFACE	02SI* 5
- - - - MOLE FRACTION - SPECIE - - -					
0.0000000 CH	0.0000021 CHN	0.0000178 CHO	0.0000000 CH2		
0.0000000 CH3	0.0000000 CH4	0.0000000 CN	0.0112015 CO2		
0.0000000 C2H2	0.0000000 C3	0.0000000 C3H	0.0000000 C2H		
0.0000000 C4H	0.0119348 H	0.0000004 HN	0.0005447 HO		
0.0000000 HSI	0.0000000 H4SI	0.0000001 N	0.0000262 NO		
0.0000000 NO2	0.0000000 NSI	0.0000000 N2O	0.0000163 O		
0.0000013 O2	0.0000028 SI	0.0000000 S12	0.0005592 O2SI		
0.3784511 CO	0.2495631 H2	0.0470340 H2O	0.1074637 N2		
0.1931805 OS1					
PRESSURE,ATM	2.72000E 00	SURF.TEMP,K	2601.00	ENTH,CAL/GM	-1.12858E 01
MDOT P.G./CM	4.00000E-01	MOL.WEIGHT	27.2046	HW(1+H/CM)	-6.09432E 01
MDOT CHAR/CM	4.00000E 00	SPEC.HEAT	0.32855	SURFACE	02SI* 5
- - - - MOLE FRACTION - SPECIE - - -					
0.0000000 CH	0.0000025 CHN	0.0000169 CHO	0.0000000 CH2		
0.0000000 CH3	0.0000000 CH4	0.0000000 CN	0.0081892 CO2		
0.0000000 C2H2	0.0000000 C3	0.0000000 C3H	0.0009000 C2H		
0.0000000 C4H	0.0100664 H	0.0000003 HN	0.0003013 HO		
0.0000000 HSI	0.0000000 H4SI	0.0000001 N	0.0000140 NO		
0.0000000 NO2	0.0000000 NSI	0.0000000 N2O	0.0000102 O		
0.0000005 O2	0.0000059 SI	0.0000000 S12	0.0005244 O2SI		
0.4177502 CO	0.1874090 H2	0.0233317 H2O	0.0766250 N2		
0.2757523 OS1					

ABLATING SURFACE THERMO-CHEMICAL EQUILIBRIA

PRESSURE,ATM 2.72000E 00 SURF.TEMP,K 2563.09 ENTH,CAL/GM-5.31587E 01
 MDOT P.G./CM 4.00000E-01 MOL.WEIGHT 28.9863 MW(1+M/CM) -3.93374E 02
 MDOT CHAR/CM 6.00000E 00 SPEC.HEAT 0.30655 SURFACE C2S1* 5
 - - - - MOLE FRACTION - SPECIE - - - -
 0.0000000 CH 0.0000055 CHN 0.0000151 CHO 0.0000000 CH2
 0.0000000 CH3 0.0000000 CH4 0.0000000 CN 0.0053497 CO2
 0.0000000 C2H2 0.0000000 C3 0.0000000 C3H 0.0000000 C2H
 0.0000000 C4H 0.0077620 H 0.0000002 HN 0.0001360 HO
 0.0000000 HS1 0.0000000 H4SI 0.0000001 N 0.0000060 NO
 0.0000000 N02 0.0000000 NSI 0.0009000 N2O 0.0000044 O
 0.0000001 O2 0.0000093 SI 0.0000000 S12 0.0003613 O2SI
 0.4409863 CO 0.1523724 H2 0.0115624 H2O 0.0595792 N2
 0.3218520 OS1

PRESSURE,ATM 2.72000E 00 SURF.TEMP,K 2338.22 ENTH,CAL/GM-1.49841E 02
 MDOT P.G./CM 4.00000E-01 MOL.WEIGHT 30.9482 MW(1+M/CM) -1.70819E 03
 MDOT CHAR/CM 1.00000E 01 SPEC.HEAT 0.28413 SURFACE O2S1* 7
 - - - - MOLE FRACTION - SPECIE - - - -
 0.0000000 CH 0.0000301 CHN 0.0000090 CHO 0.0000000 CH2
 0.0000000 CH3 0.0000000 CH4 0.0000000 CN 0.0005646 CO2
 0.0000000 C2H2 0.0000000 C3 0.0000000 C3H 0.0000000 C2H
 0.0000000 C4H 0.0023992 H 0.0000000 HN 0.0000029 HO
 0.0000000 HS1 0.0000000 H4SI 0.0000000 N 0.0000001 NO
 0.0000000 N02 0.0000000 NSI 0.0000000 N2O 0.0000000 O
 0.0000000 O2 0.0000309 SI 0.0000001 S12 0.0000304 O2SI
 0.4683762 CO 0.1143621 H2 0.0007770 H2O 0.0412801 N2
 0.3721371 OS1

PRESSURE,ATM 2.72000E 00 SURF.TEMP,K 2072.65 ENTH,CAL/GM 1.75800E 02
 MDOT P.G./CM 6.00000E-01 MOL.WEIGHT 15.3372 MW(1+M/CM) 2.83038E 02
 MDOT CHAR/CM 10.00000E-03 SPEC.HEAT 0.56095 SURFACE O2S1* 10
 - - - - MOLE FRACTION - SPECIE - - - -
 0.0000000 CH 0.0000087 CHN 0.0000071 CHO 0.0000000 CH2
 0.0000000 CH3 0.0000002 CH4 0.0000000 CN 0.0047062 CO2
 0.0000000 C2H2 0.0000000 C3 0.0000000 C3H 0.0000000 C2H
 0.0000000 C4H 0.0010941 H 0.0000000 HN 0.0000086 HO
 0.0000000 HS1 0.0000000 H4SI 0.0000000 N 0.0000002 NO
 0.0000000 N02 0.0000000 NSI 0.0000000 N2O 0.0000000 O
 0.0000000 O2 0.0000000 SI 0.0000000 S12 0.0000008 O2SI
 0.3382361 CO 0.4779035 H2 0.0318263 H2O 0.1449022 N2
 0.0013053 OS1

ABLATING SURFACE THERMO-CHEMICAL EQUILIBRIA

PRESSURE,ATM 2.72000E 00 SURF.TEMP,K 2189.83 ENTH,CAL/GM 2.34590E 02
 MDOT P.G./CM 6.00000E-01 MOL.WEIGHT 15.5411 HW(1+M/CM) 3.87074E 02
 MDOT CHAR/CM 5.00000E-02 SPEC.HEAT 0.55756 SURFACE 02SI* 4
 - - - - MOLE FRACTION - SPECIE - - - -
 0.0000000 CH 0.0000086 CHN 0.0000095 CHO 0.0000000 CH2
 0.0000000 CH3 0.0000001 CH4 0.0000000 CN 0.0043670 CO2
 0.0000000 C2H2 0.0000000 C3 0.0000000 C3H 0.0000000 C2H
 0.0000000 C4H 0.0022032 H 0.0000000 HN 0.0000208 HO
 0.0000000 HSI 0.0000000 H4SI 0.0000000 N 0.0000005 NO
 0.0000000 NO2 0.0000000 NSI 0.0000000 N2O 0.0000001 O
 0.0000000 O2 0.0000000 SI 0.0000000 SI2 0.0000044 O2SI
 0.3402471 CO 0.4720524 H2 0.0313649 H2O 0.1432691 N2
 0.0064523 OSI

PRESSURE,ATM 2.72000E 00 SURF.TEMP,K 2243.20 ENTH,CAL/GM 2.53158E 02
 MDOT P.G./CM 6.00000E-01 MOL.WEIGHT 15.7944 HW(1+M/CM) 4.30368E 02
 MDOT CHAR/CM 1.00000E-01 SPEC.HEAT 0.55025 SURFACE 02SI* 4
 - - - - MOLE FRACTION - SPECIE - - - -
 0.0000000 CH 0.0000086 CHN 0.0000108 CH2 0.0000000 CH2
 0.0000000 CH3 0.0000001 CH4 0.0000000 CN 0.0042059 CO2
 0.0000000 C2H2 0.0000000 C3 0.0000000 C3H 0.0000000 C2H
 0.0000000 C4H 0.0029462 H 0.0000001 HN 0.0000298 HO
 0.0000000 HSI 0.0000000 H4SI 0.0000000 N 0.0000008 NO
 0.0000000 NO2 0.0000000 NSI 0.0000000 N2O 0.0000001 O
 0.0000000 O2 0.0000001 SI 0.0000000 SI2 0.0000091 O2SI
 0.3425529 CO 0.4656185 H2 0.0305663 H2O 0.1415220 N2
 0.0127288 OSI

PRESSURE,ATM 2.72000E 00 SURF.TEMP,K 2296.86 ENTH,CAL/GM 2.59470E 02
 MDOT P.G./CM 6.00000E-01 MOL.WEIGHT 16.2852 HW(1+M/CM) 4.67046E 02
 MDOT CHAR/CM 2.00000E-01 SPEC.HEAT 0.53513 SURFACE 02SI* 4
 - - - - MOLE FRACTION - SPECIE - - - -
 0.0000000 CH 0.0000087 CHN 0.0000121 CHO 0.0000000 CH2
 0.0000000 CH3 0.0000001 CH4 0.0000000 CN 0.0040133 CO2
 0.0000000 C2H2 0.0000000 C3 0.0000000 C3H 0.0000000 C2H
 0.0000000 C4H 0.0038690 H 0.0000001 HN 0.0000410 HO
 0.0000000 HSI 0.0000000 H4SI 0.0000000 N 0.0000012 NO
 0.0000000 NO2 0.0000000 NSI 0.0000000 N2O 0.0000002 O
 0.0000000 O2 0.0000002 SI 0.0000000 SI2 0.0000182 O2SI
 0.3469550 CO 0.4537429 H2 0.0289304 H2O 0.1376177 N2
 0.0247898 OSI

ABLATING SURFACE THERMO-CHEMICAL EQUILIBRIA

PRESSURE,ATM	2.72000E 00	SURF.TEMP,K	2347.94	ENTH,CAL/GM	2.43597E 02
MDOT P.G./CM	6.00000E-01	MOL.WEIGHT	17.1994	HW(1+M/CM)	4.87195E 02
MDOT CHAR/CM	4.00000E-01	SPEC.HEAT	0.50784	SURFACE	02SI* 4
- - - - MOLE FRACTION - SPECIE - - -					
0.0000000 CH	0.0000090 CHN	0.0000135 CHO	0.0000000 CH2		
0.0000000 CH3	0.0000000 CH4	0.0000000 CN	0.0037464 CO2		
0.0000000 C2H2	0.0000000 C3	0.0000000 C3H	0.0000000 C2H		
0.0000000 C4H	0.0048968 H	0.0000001 HN	0.0000521 HO		
0.0000000 HSI	0.0000000 H4SI	0.0000000 N	0.0000016 NO		
0.0000000 NO2	0.0000000 NSI	0.0000000 N2O	0.0000004 O		
0.0000000 O2	0.0000005 SI	0.0000000 SI2	0.0000342 02SI		
0.3551371 CO	0.4323386 H2	0.0258350 H2O	0.1308079 N2		
0.0471267 OSI					
PRESSURE,ATM	2.72000E 00	SURF.TEMP,K	2374.31	ENTH,CAL/GM	2.19817E 02
MDOT P.G./CM	6.00000E-01	MOL.WEIGHT	18.0308	HW(1+M/CM)	4.83598E 02
MDOT CHAR/CM	6.00000E-01	SPEC.HEAT	0.48488	SURFACE	02SI* 4
- - - - MOLE FRACTION - SPECIE - - -					
0.0000000 CH	0.0000094 CHN	0.0000143 CH2	0.0000000 CH2		
0.0000000 CH3	0.0000000 CH4	0.0000000 CN	0.0035197 CO2		
0.0000000 C2H2	0.0000000 C3	0.0000000 C3H	0.0000000 C2H		
0.0000000 C4H	0.0054509 H	0.0000001 HN	0.0000560 HO		
0.0000000 HSI	0.0000000 H4SI	0.0000000 N	0.0000018 NO		
0.0000000 NO2	0.0000000 NSI	0.0000000 N2O	0.0000005 O		
0.0000000 O2	0.0000009 SI	0.0000000 SI2	0.0000468 02SI		
0.3626033 CO	0.4132301 H2	0.0230298 H2O	0.1246642 N2		
0.0673722 OSI					
PRESSURE,ATM	2.72000E 00	SURF.TEMP,K	2399.56	ENTH,CAL/GM	1.72479E 02
MDOT P.G./CM	6.00000E-01	MOL.WEIGHT	19.4846	HW(1+M/CM)	4.48444E 02
MDOT CHAR/CM	1.00000E 00	SPEC.HEAT	0.44897	SURFACE	02SI* 4
- - - - MOLE FRACTION - SPECIE - - -					
0.0000000 CH	0.0000103 CHN	0.0000149 CHO	0.0000000 CH2		
0.0000000 CH3	0.0000000 CH4	0.0000000 CN	0.0030927 CO2		
0.0000000 C2H2	0.0000000 C3	0.0000000 C3H	0.0000000 C2H		
0.0000000 C4H	0.0059051 H	0.0000001 HN	0.0000538 HO		
0.0000000 HSI	0.0000000 H4SI	0.0000000 N	0.0000017 NO		
0.0000000 NO2	0.0000000 NSI	0.0000000 N2O	0.0000005 O		
0.0000000 O2	0.0000018 SI	0.0000000 SI2	0.0000627 02SI		
0.3757439 CO	0.3802455 H2	0.0181962 H2O	0.1139891 N2		
0.1026807 OSI					

ABLATING SURFACE THERMO-CHEMICAL EQUILIBRIA

PRESSURE,ATM 2.72000E 00 SURF.TEMP,K 2401.18 ENTH,CAL/GM 7.88366E 01
 MDOT P.G./CM 6.00000E-01 MOL.WEIGHT 22.2368 HW(1+M/CM) 2.83812E 02
 MDOT CHAR/CM 2.00000E 00 SPEC.HEAT 0.39309 SURFACE 02SI* 5

--- MOLE FRACTION - SPECIE ---

0.0000000 CH	0.0000149 CHN	0.0000146 CHO	0.0000000 CH2
0.0000000 CH3	0.0000000 CH4	0.0000000 CN	0.0020346 CO2
0.0000000 C2H2	0.0000000 C3	0.0000000 C3H	0.0000000 C2H
0.0000000 C4H	0.0054481 H	0.0000001 HN	0.0000307 HO
0.0000000 HSI	0.0000000 H4SI	0.0000000 N	0.0000010 NO
0.0000000 NO2	0.0000000 NSI	0.0000000 N2O	0.0000003 O
0.0000000 U2	0.0000048 SI	0.0000000 SI2	0.0000639 O2SI
0.4010091 CO	0.3187139 H2	0.0094089 H2O	0.0939510 N2
0.1693039 OSI			

PRESSURE,ATM 2.72000E 00 SURF.TEMP,K 2206.32 ENTH,CAL/GM-8.13879E 01
 MDOT P.G./CM 6.00000E-01 MOL.WEIGHT 25.6498 HW(1+M/CM) -4.55772E 02
 MDOT CHAR/CM 4.00000E 00 SPEC.HEAT 0.33842 SURFACE SIC 9

--- MOLE FRACTION - SPECIE ---

0.0000000 CH	0.0006017 CHN	0.0000091 CHU	0.0000000 CH2
0.0000012 CH3	0.0000041 CH4	0.0000000 CN	0.0000498 CO2
0.0000089 C2H2	0.0000000 C3	0.0000000 C3H	0.0000001 C2H
0.0000000 C4H	0.0017391 H	0.0000000 HN	0.0000001 HO
0.0000001 HSI	0.0000001 H4SI	0.0000000 N	0.0000000 NO
0.0000000 NO2	0.0000000 NSI	0.0000000 N2O	0.0000000 O
0.0000000 O2	0.0000939 SI	0.0000032 SI2	0.0000016 O2SI
0.4328691 CO	0.2440134 H2	0.0001467 H2O	0.0693722 N2
0.2510864 OSI			

PRESSURE,ATM 2.72000E 00 SURF.TEMP,K 2595.75 ENTH,CAL/GM 3.53855E 01
 MDOT P.G./CM 6.00000E-01 MOL.WEIGHT 27.5572 HW(1+M/CM) 2.68930E 02
 MDOT CHAR/CM 6.00000E 00 SPEC.HEAT 0.31893 SURFACE SI* 7

--- MOLE FRACTION - SPECIE ---

0.0000000 CH	0.0017728 CHN	0.0000180 CHO	0.0000000 CH2
0.0000030 CH3	0.0000015 CH4	0.0000022 CN	0.0000113 CO2
0.0000731 C2H2	0.0000000 C3	0.0000004 C3H	0.0000051 C2H
0.0000000 C4H	0.0098761 H	0.0000002 HN	0.0000004 HO
0.0000057 HSI	0.0000001 H4SI	0.0000001 N	0.0000000 NO
0.0000000 NO2	0.0000002 NSI	0.0000000 N2O	0.0000000 O
0.0000000 O2	0.0047504 SI	0.0004730 SI2	0.0000000 O2SI
0.4478545 CO	0.1882809 H2	0.0000302 H2O	0.0542602 N2
0.2925722 OSI			

ABLATING SURFACE THERMO-CHEMICAL EQUILIBRIA

PRESSURE,ATM	2.72000E 00	SURF.TEMP,K	2732.70	ENTH,CAL/GM	5.54762E 01		
MDOT P.G./CM	6.00000E-01	MOL.WEIGHT	29.7138	HW(1+M/CM)	6.43523E 02		
MDOT CHAR/CM	1.00000E 01	SPEC.HEAT	0.29614	SURFACE	SI*		
- - - - MOLE FRACTION - SPECIE - - - -							
0.0000001	CH	0.0013515	CHN	0.0000194	CHO	0.0000000	CH2
0.0000018	CH3	0.0000005	CH4	0.0000042	CN	0.0000107	C02
0.0000552	C2H2	0.0000000	C3	0.0000006	C3H	0.0000084	C2H
0.0000000	C4H	0.0139379	H	0.0000004	HN	0.0000006	HO
0.0000123	HSI	0.0000000	H4SI	0.0000002	N	0.0000000	NO
0.0000000	NO2	0.0000005	NSI	0.0000000	N2O	0.0000000	U
0.0000000	O2	0.0115677	SI	0.0012373	SI2	0.0000009	O2SI
0.4668777	CO	0.1294696	H2	0.0000197	H2O	0.0382862	N2
0.3371364	OSI						

PRESSURE,ATM	2.72000E 00	SURF.TEMP,K	2712.75	ENTH,CAL/GM	9.83902E 02		
MDOT P.G./CM	1.00000E 00	MOL.WEIGHT	14.4398	HW(1+M/CM)	1.97764E 03		
MDOT CHAR/CM	10.00000E-03	SPEC.HEAT	0.62737	SURFACE	C*		
- - - - MOLE FRACTION - SPECIE - - - -							
0.0000009	CH	0.0332974	CHN	0.0000266	CHO	0.0000009	CH2
0.0001122	CH3	0.0000607	CH4	0.0000482	CN	0.0000007	C02
0.0140332	C2H2	0.0000020	C3	0.0006064	C3H	0.0010077	C2H
0.0001815	C4H	0.0252819	H	0.0000010	HN	0.0000001	HO
0.0000005	HSI	0.0000000	H4SI	0.0000003	N	0.0000000	NO
0.0000000	NO2	0.0000000	NSI	0.0000000	N2O	0.0000000	U
0.0000000	O2	0.0002543	SI	0.0000007	SI2	0.0000000	O2SI
0.3376401	CO	0.4941020	H2	0.0000067	H2O	0.0926052	N2
0.0007287	OSI						

PRESSURE,ATM	2.72000E 00	SURF.TEMP,K	2708.86	ENTH,CAL/GM	9.64355E 02		
MDOT P.G./CM	1.00000E 00	MOL.WEIGHT	14.5997	HW(1+M/CM)	1.97693E 03		
MDOT CHAR/CM	5.00000E-02	SPEC.HEAT	0.61984	SURFACE	C*		
- - - - MOLE FRACTION - SPECIE - - - -							
0.0000008	CH	0.0327705	CHN	0.0000265	CHO	0.0000009	CH2
0.0001101	CH3	0.0000601	CH4	0.0000467	CN	0.0000007	C02
0.0137312	C2H2	0.0000019	C3	0.0005845	C3H	0.0009739	C2H
0.0001736	C4H	0.0248192	H	0.0000010	HN	0.0000001	HO
0.0000025	HSI	0.0000001	H4SI	0.0000003	N	0.0000000	NO
0.0000000	NO2	0.0000001	NSI	0.0000000	N2O	0.0000000	U
0.0000000	O2	0.0012236	SI	0.0000159	SI2	0.0000000	O2SI
0.3396280	CO	0.4902703	H2	0.0000068	H2O	0.0919207	N2
0.0036241	OSI						

ABLATING SURFACE THERMO-CHEMICAL EQUILIBRIA

PRESSURE,ATM	2.72000E 00	SURF.TEMP,K	2741.42	ENTH,CAL/GM	9.79401E 02
MDOT P.G./CM	1.00000E 00	MOL.WEIGHT	14.7634	HW(1+M/CM)	2.05674E 03
MDOT CHAR/CM	1.00000E-01	SPEC.HEAT	0.61212	SURFACE	SIC
- - - - MOLE FRACTION - SPECIE - - -					
0.0000010	CH	0.0320040	CHN	0.0000278	CHO
0.0001061	CH ₃	0.0000514	CH ₄	0.0000544	CN
0.0129815	C ₂ H ₂	0.0000023	C ₃	0.0006018	C ₃ H
0.0001761	C ₄ H	0.0277990	H	0.0000011	HN
0.0000055	HSI	0.0000001	H ₄ SI	0.0000004	N
0.0000000	N ₂ O	0.0000002	NSI	0.0000000	N ₂ O
0.0000000	O ₂	0.0026635	SI	0.0000624	S ₁ 2
0.3416268	CO	0.4830114	H ₂	0.0000068	H ₂ O
0.0068444	OSI				0.0909088 N ₂
PRESSURE,ATM 2.72000E 00 SURF.TEMP,K 2836.02 ENTH,CAL/GM 1.05072E 03					
MDOT P.G./CM	1.00000E 00	MOL.WEIGHT	15.0215	HW(1+M/CM)	2.31158E 03
MDOT CHAR/CM	2.00000E-01	SPEC.HEAT	0.59871	SURFACE	SIC
- - - - MOLE FRACTION - SPECIE - - -					
0.0000019	CH	0.0298711	CHN	0.0000318	CHO
0.0000957	CH ₃	0.0000333	CH ₄	0.0000824	CN
0.0109547	C ₂ H ₂	0.0000036	C ₃	0.0006358	C ₃ H
0.0001766	C ₄ H	0.0381781	H	0.0000018	HN
0.0000140	HSI	0.0000001	H ₄ SI	0.0000008	N
0.0000000	N ₂ O	0.0000005	NSI	0.0000000	N ₂ O
0.0000000	O ₂	0.0066551	SI	0.0002324	S ₁ 2
0.3455765	CO	0.4656480	H ₂	0.0000069	H ₂ O
0.0115879	OSI				0.0888843 N ₂
PRESSURE,ATM 2.72000E 00 SURF.TEMP,K 2913.26 ENTH,CAL/GM 1.06295E 03					
MDOT P.G./CM	1.00000E 00	MOL.WEIGHT	15.5712	HW(1+M/CM)	2.59909E 03
MDOT CHAR/CM	4.00000E-01	SPEC.HEAT	0.57184	SURFACE	SIC
- - - - MOLE FRACTION - SPECIE - - -					
0.0000028	CH	0.0257395	CHN	0.0000353	CHO
0.0000788	CH ₃	0.0000210	CH ₄	0.0001045	CN
0.0080834	C ₂ H ₂	0.0000041	C ₃	0.0005253	C ₃ H
0.0001304	C ₄ H	0.0480547	H	0.0000025	HN
0.0000298	HSI	0.0000001	H ₄ SI	0.0000014	N
0.0000000	N ₂ O	0.0000011	NSI	0.0000000	N ₂ O
0.0000000	O ₂	0.0141418	SI	0.0007050	S ₁ 2
0.3549579	CO	0.4402681	H ₂	0.0000074	H ₂ O
0.0199978	OSI				0.0857669 N ₂

TABLE II
CHEMICAL EROSION PROGRAM TEST SERIES, MIXTURES 4 AND 5

Mixture	Nominal Test Conditions		Nozzle Material or Test Type	Nozzle No.	Test No.
	Total Temperature (°K)	Initial Plenum Pressure* (psia)			
4	3500	300 (0.3)	Graphite GX graphite	E17	939
4	3500	300 (.3)	Graphite GX graphite	E10	940
4	3500	300 (.3)	Graphite GX graphite	E19	997
4	3500	175 (.4)	Graphite GX graphite	E31	998
4	3500	300 (.3)	ATJ graphite	E43	1000
4	3500	300 (.3)	MX4500 graphite phenolic	E34	999
4	3500	300 (.3)	MX4500 graphite phenolic	E38	1001
4	3500	300 (.3)	MX2600 silica phenolic	E22	941
4	2750	300 (.3)	Graphite GX graphite	E13	1039
4	2750	300 (.3)	MX4500 graphite phenolic	E39	1040
4	2750	300 (.3)	MX2600 silica phenolic	E26	1038

* Number in parenthesis indicates initial nozzle throat diameter in inches.

TABLE II (Continued)

Nominal Test Conditions		Initial Plenum Pressure* (psia)	Nozzle Material or Test Type	Nozzle No.	Test No.
Mixture	Total Temperature (°K)				
4	2000	300	(.3) Graphitite GX graphite	E12	1023
	2000	300	(.3) MX4500 graphite phenolic	E36	1024
4	2000	300	(.3) MX2600 silica phenolic	E23	1017 and 1020
	3500	300	(.3) Graphitite GX graphite	E18	957 and 958
5	3500	300	(.3) Graphitite GX graphite	E11	959
	3500	175	(.4) Graphitite GX graphite	E32	1004
5	3500	300	(.3) ATJ graphite	E42	1005
	3500	300	(.3) MX4500 graphite phenolic	E35	1006
5	3500	300	(.3) MX2600 silica phenolic	E24	960
	2750	300	(.3) MX4500 graphite	E40	1043
5	2750	300	(.3) MX2600 silica phenolic	E27	1042
	2000	300	(.3) MX4500 graphite phenolic	E37	1026 and 1028

*Number in parenthesis indicates initial nozzle throat diameter in inches.

TABLE II (Continued)

Nominal Test Conditions		Nozzle Material or Test Type	Nozzle No.	Test No.
Mixture	Total Temperature (°K)			
5	2000	300 (.3)	MX-600 silica phenolic	E25
	3500	300 (.3)		
4	3500	175 (.4)	Pressure distribution calibration	.3PD
	3500	110 (.5)		
4	2000	175 (.4)	Pressure distribution calibration	.4PD
	3500	300 (.3)		
5	3500	175 (.4)	Pressure distribution calibration	.5PD
	3500	110 (.5)		
5	2000	175 (.4)	Pressure distribution calibration	.4PD
	3500	300 (.3)		
5	3500	175 (.4)	Pressure distribution calibration	.3PD
	3500	110 (.5)		
5	2000	175 (.4)	Pressure distribution calibration	.4PD
	3500	300 (.3)		
4	3500	175 (.4)	Heat-transfer calibration	.3HT
	3500	350 (.4)		

* Number in parenthesis indicates initial nozzle throat diameter in inches.

TABLE II (Concluded)

Nominal Test Conditions			Nozzle Material or Test Type	Nozzle No.	Test No.
Mixture	Total Temperature (°K)	Initial Plenum Pressure* (psia)			
4	3500	110 (.5)	Heat-transfer calibration	.5HT	946
	2000	175 (.4)	Heat-transfer calibration	.4HT	1022
5	3500	300 (.3)	Heat-transfer calibration	.3HT	948
	3500	175 (.4)	Heat-transfer calibration	.4HT	949
5	3500	110 (.5)	Heat-transfer calibration	.5HT	945
	2000	175 (.4)	Heat-transfer calibration	.4HT	1032

*Number in parenthesis indicates initial nozzle throat diameter in inches.

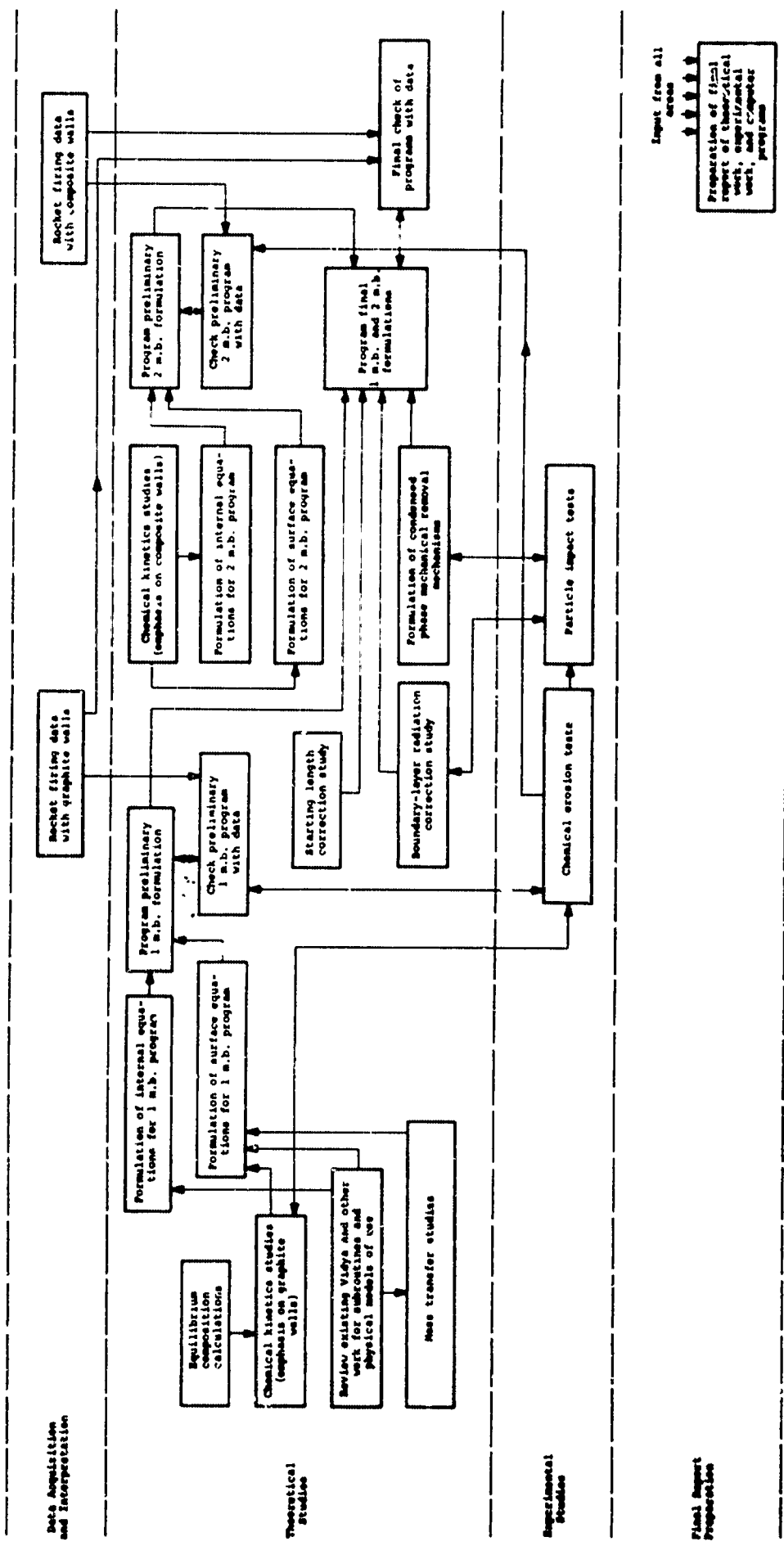


Figure 1.- Program flow chart.

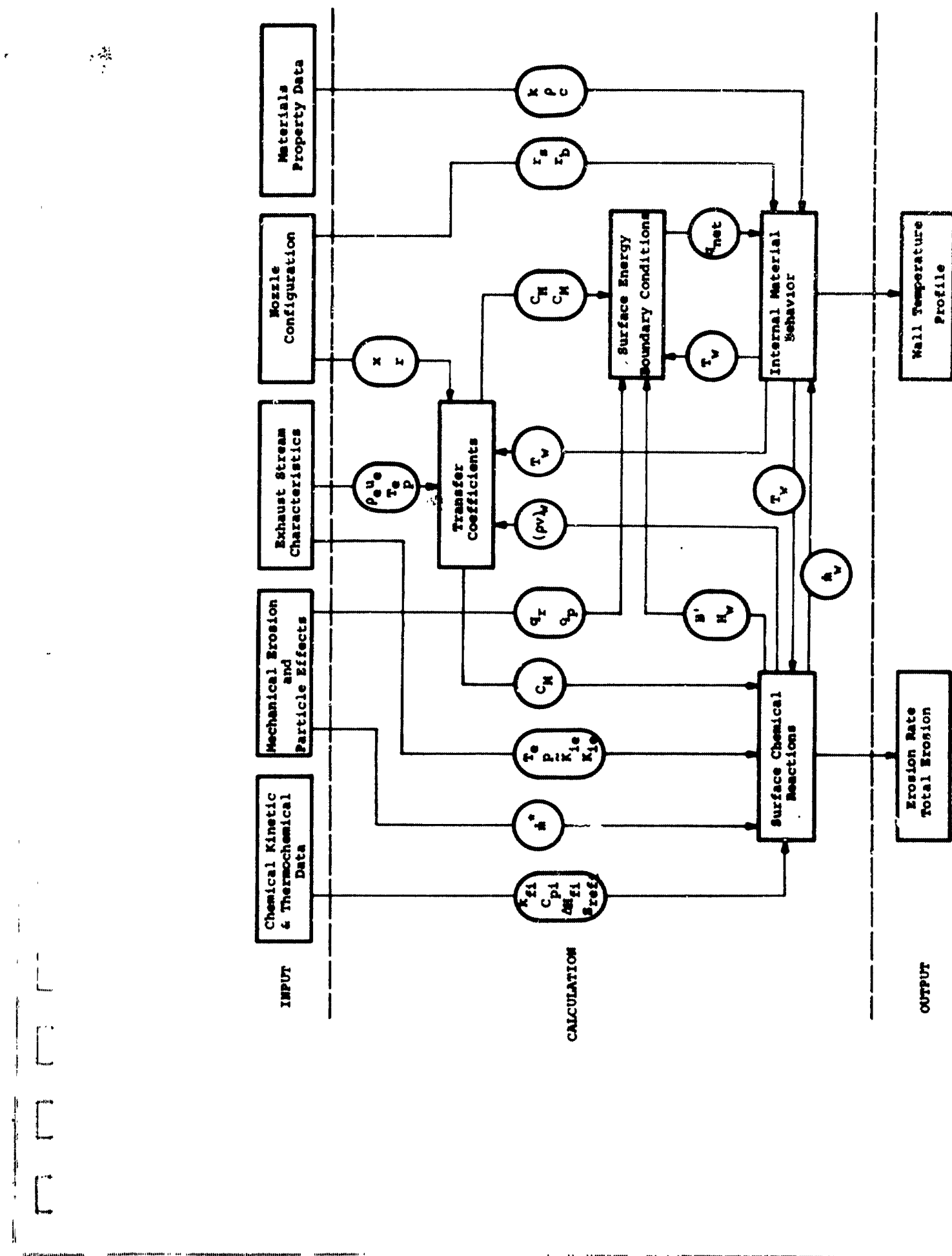


Figure 2.- Flow diagram of wall-erosion calculation.

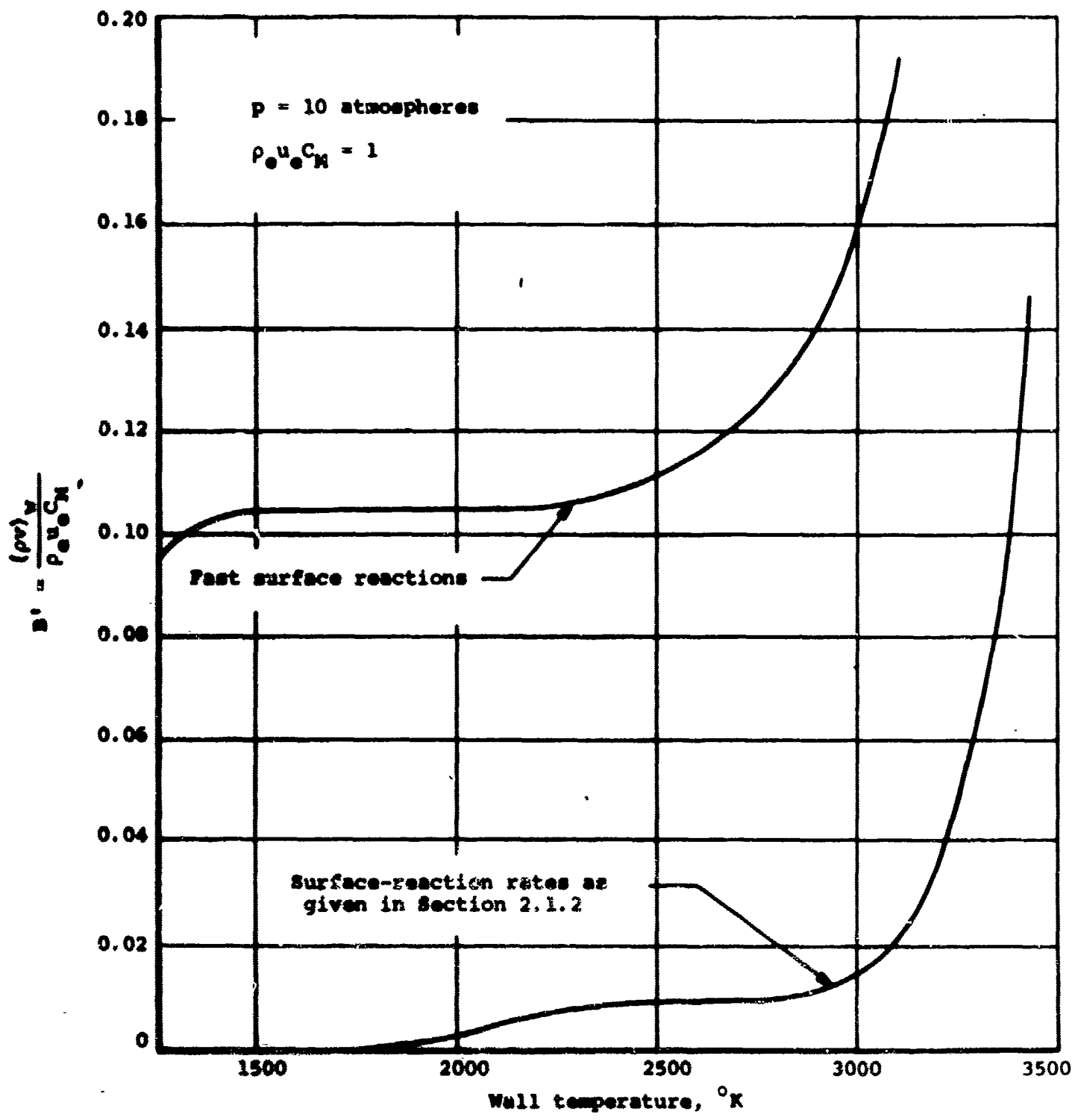
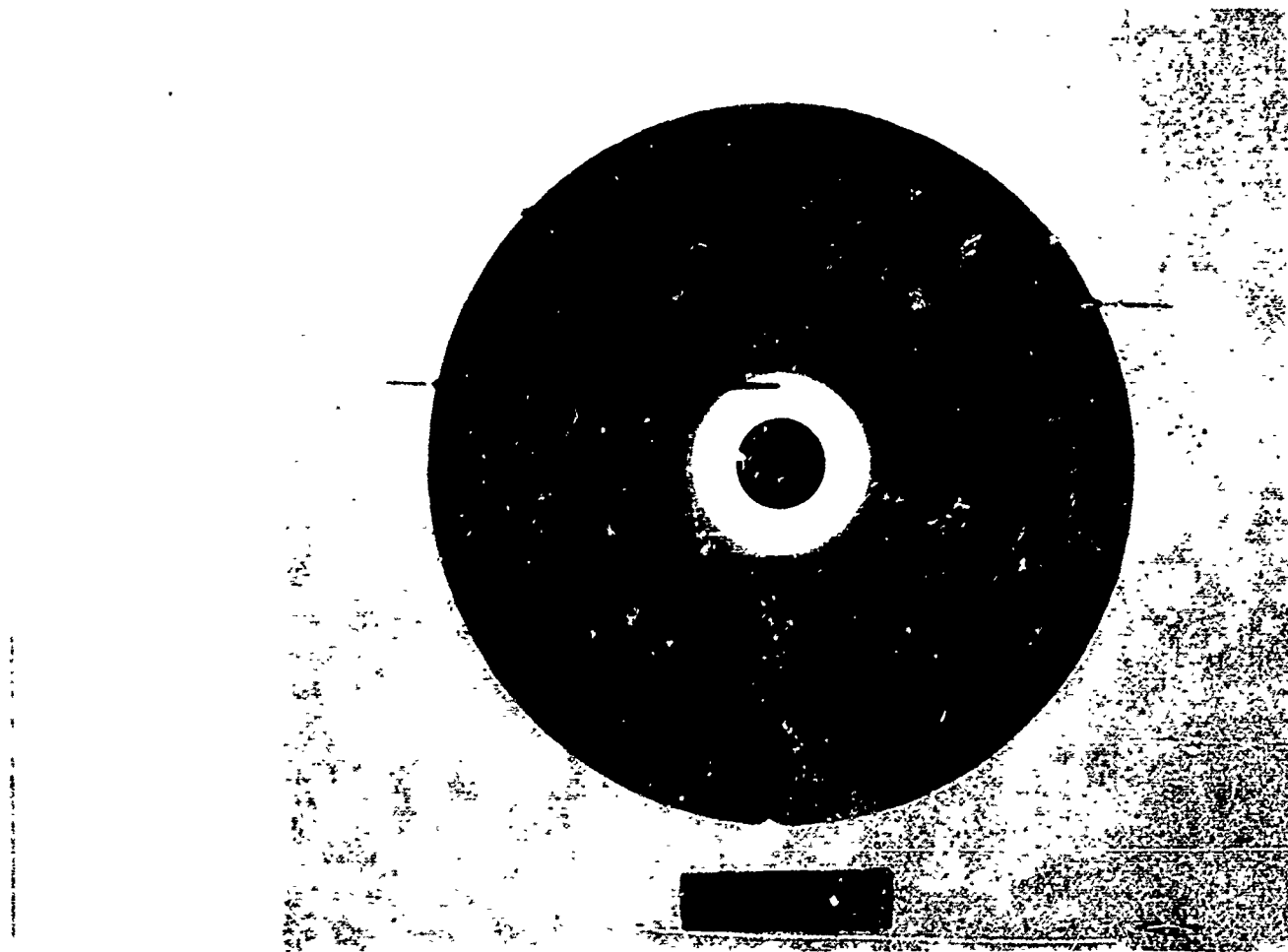


Figure 3.- Theoretical chemical erosion of graphite in an H, C, N, O, Cl exhaust.



0
Figure 4.- Typical X-ray photograph for determining thermocouple locations.

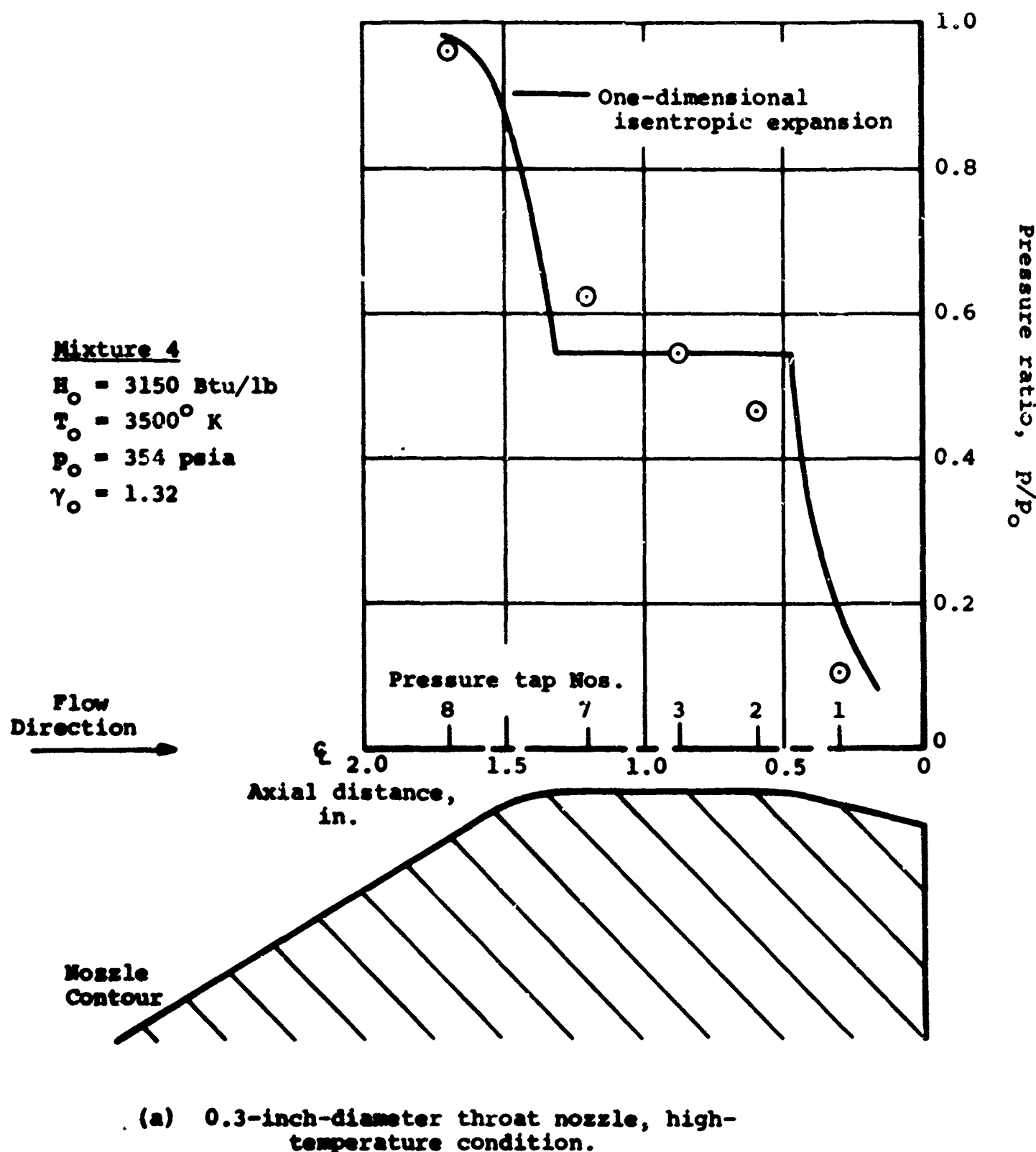
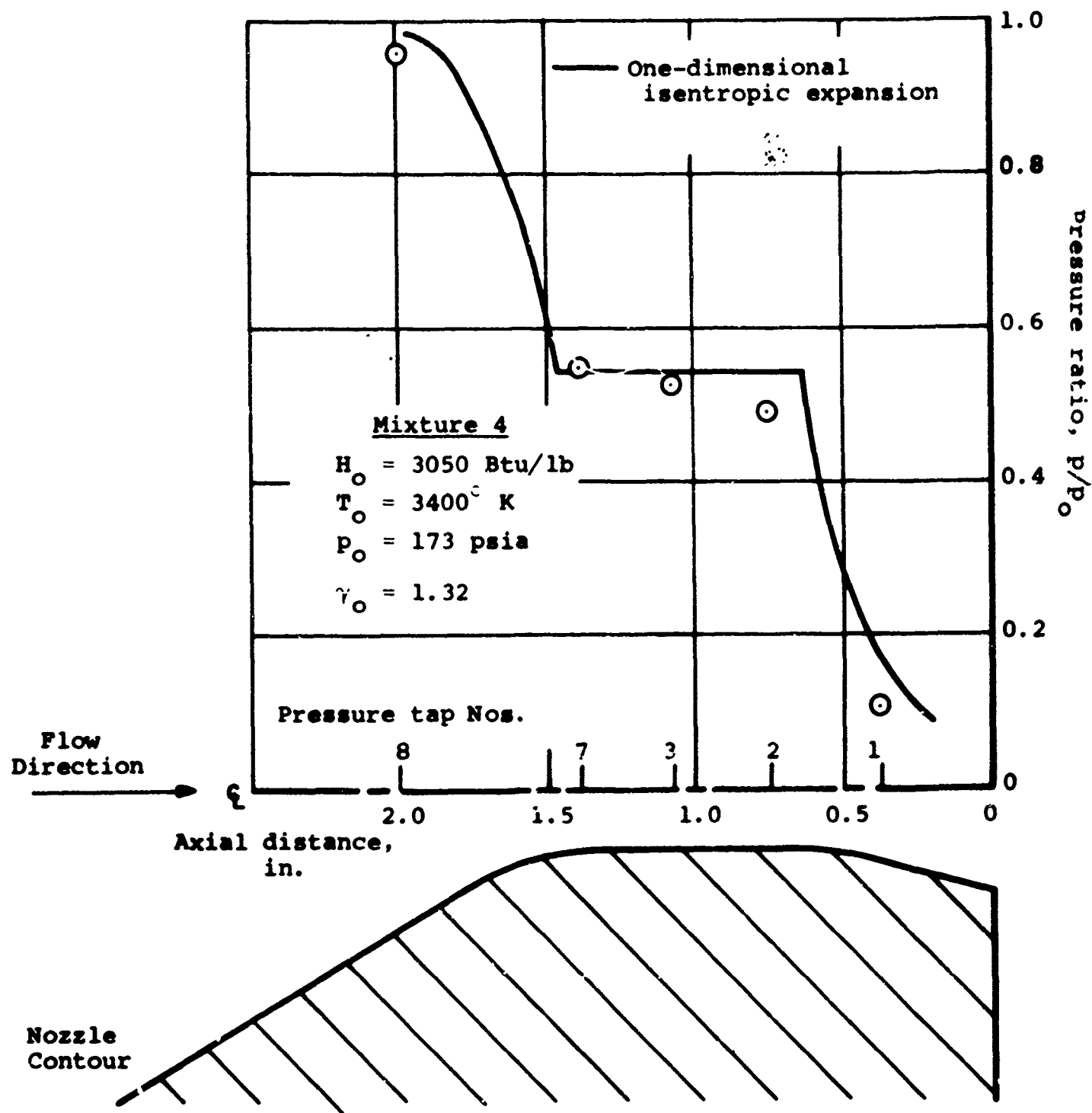
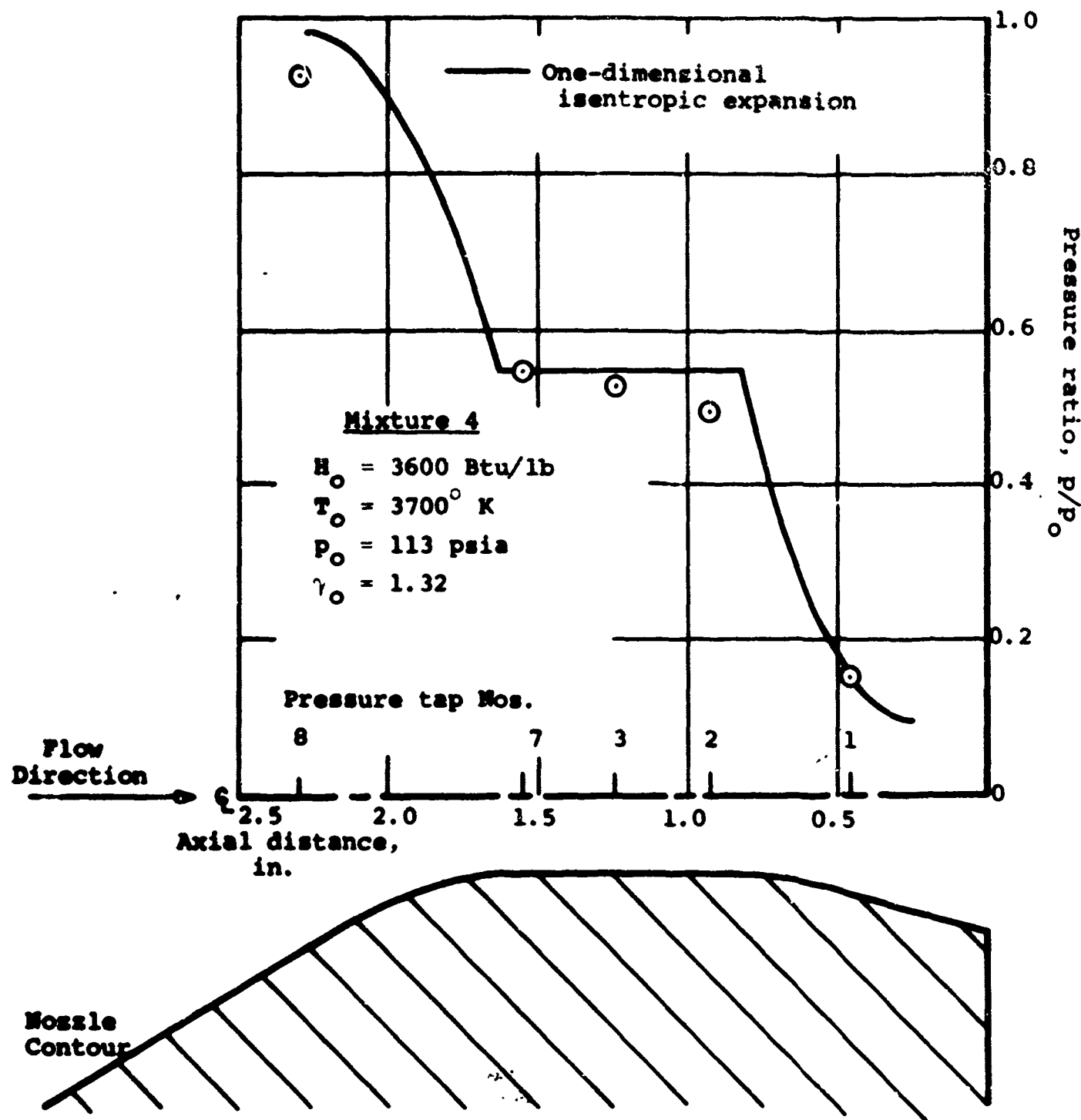


Figure 5.- Pressure distribution, Mixture 4.



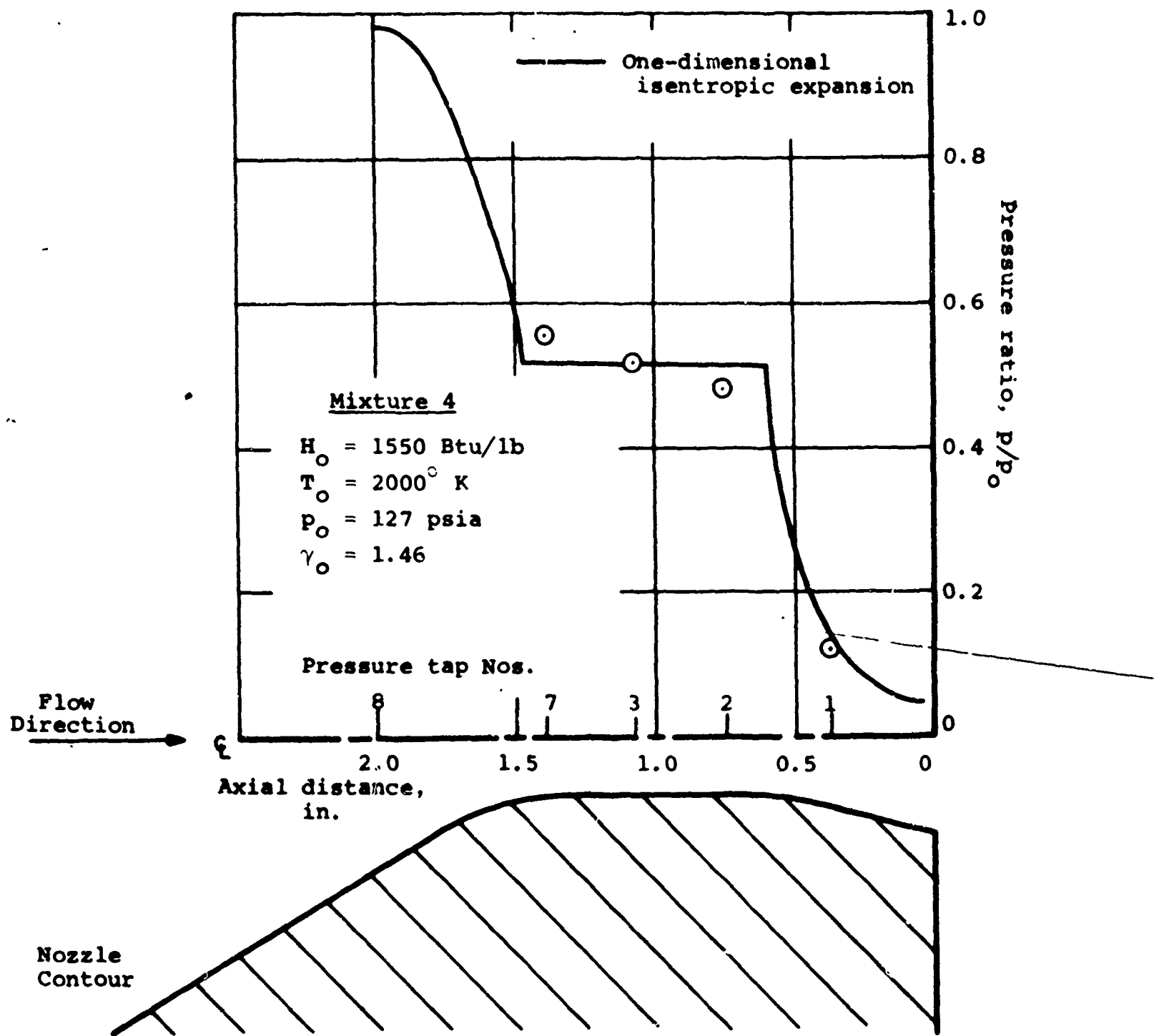
(b) 0.4-inch-diameter throat nozzle, high-temperature condition.

Figure 5.- Continued.



(c) 0.5-inch-diameter throat nozzle, high-temperature condition.

Figure 5.- Continued.



(d) 0.4-inch-diameter throat nozzle, low-temperature condition.

Figure 5.- Concluded.

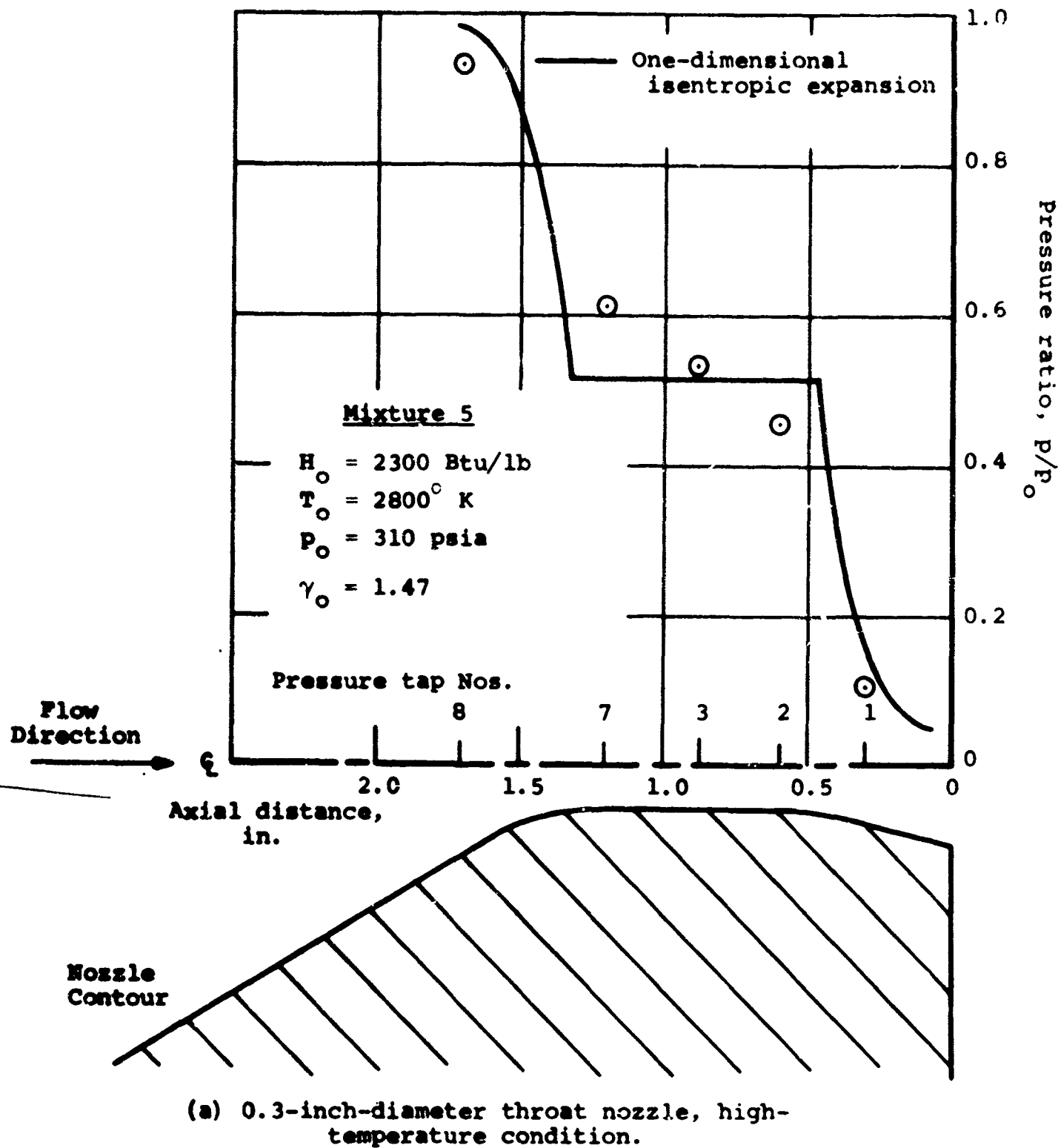


Figure 6.- Pressure distribution, Mixture 5.

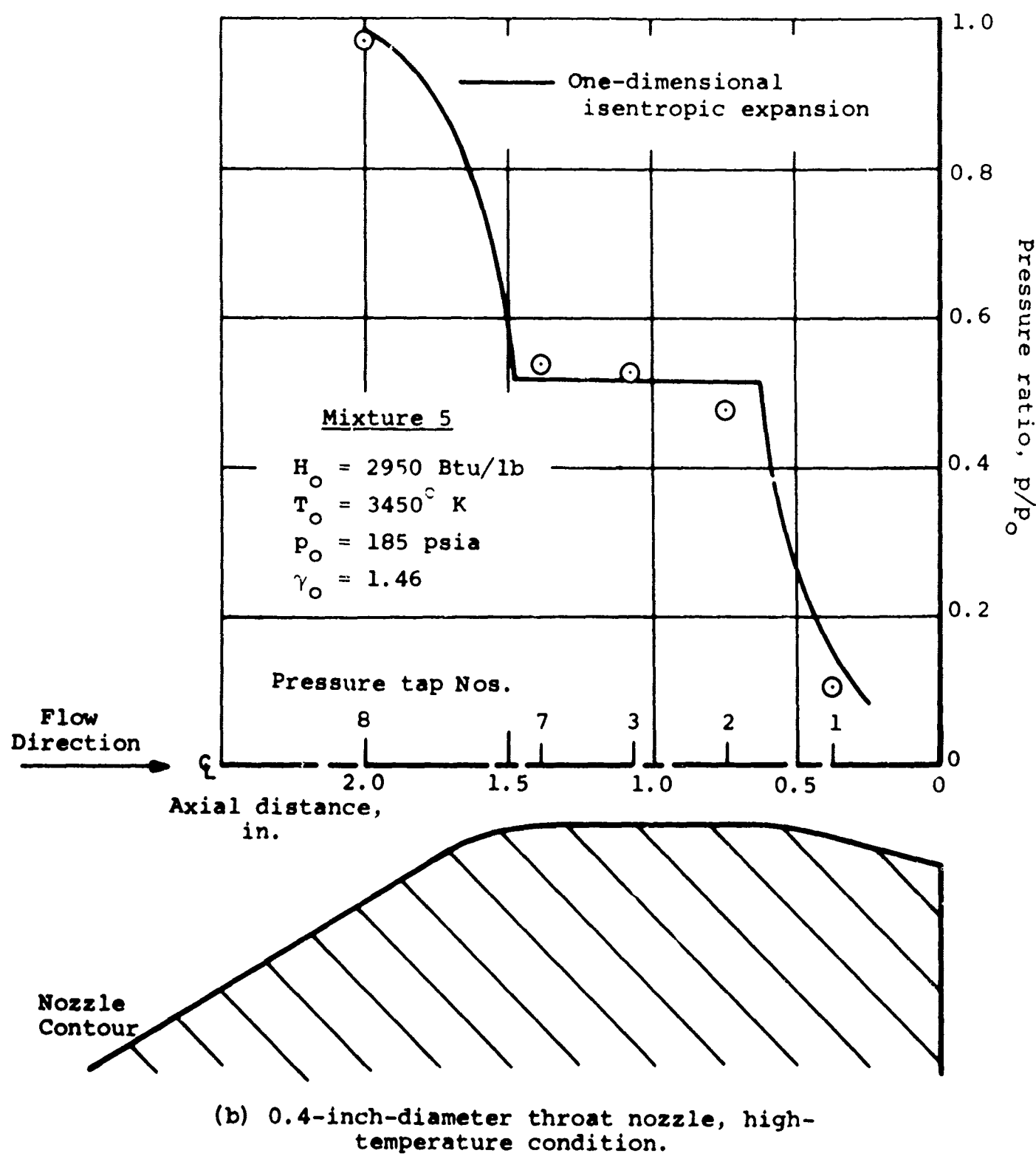
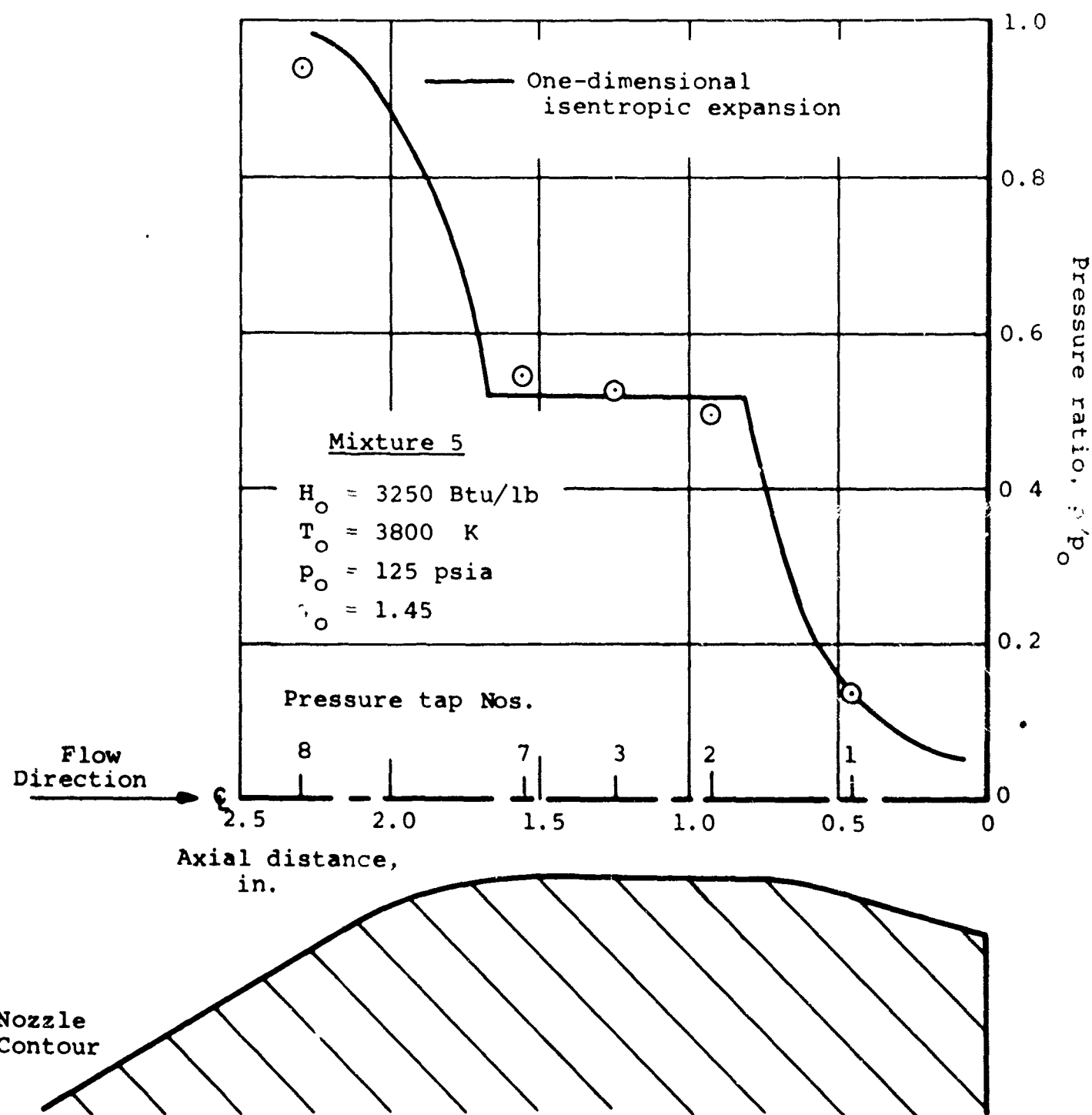
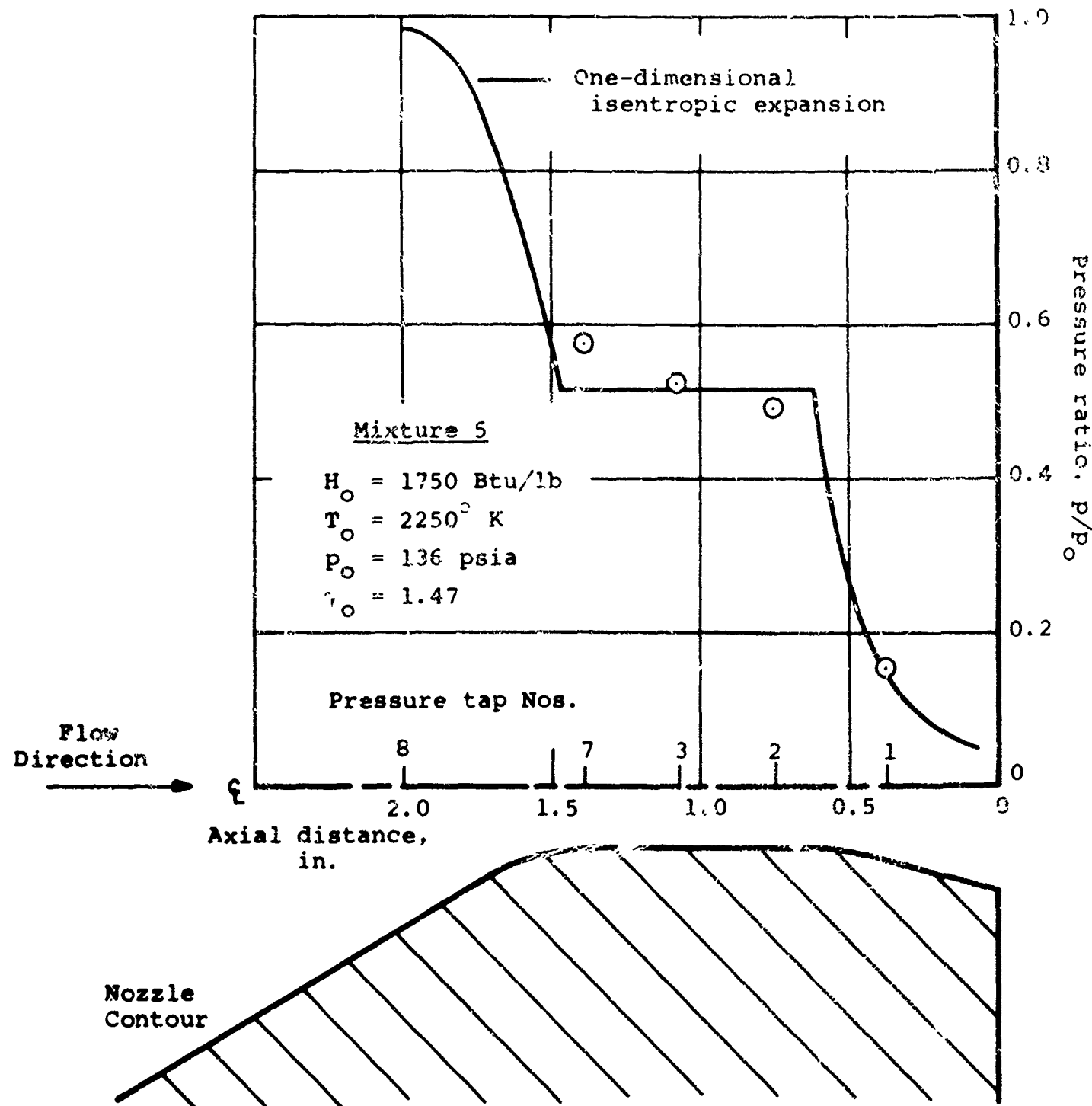


Figure 6.- Continued.



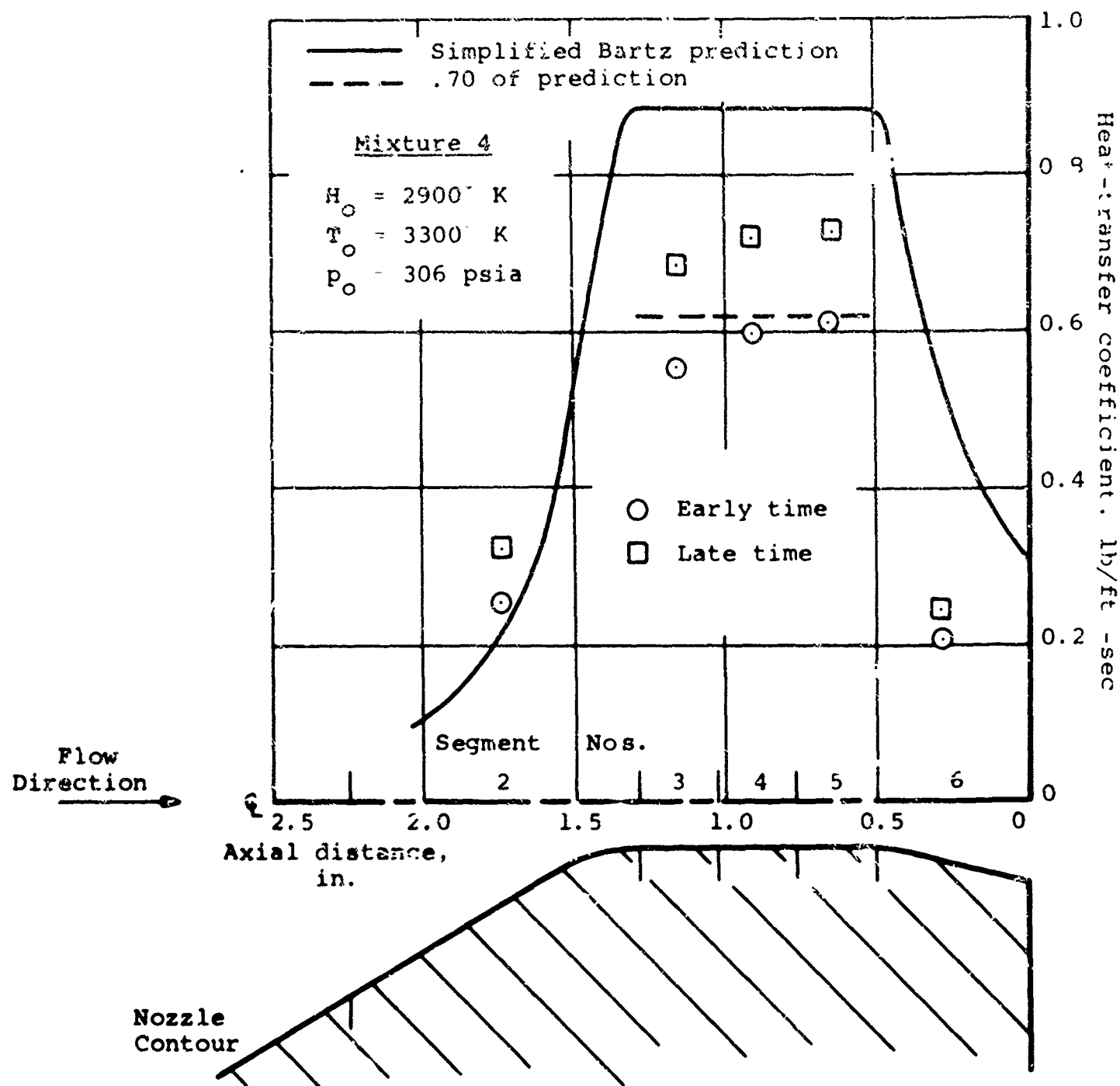
(c) 0.5-inch-diameter throat nozzle, high-temperature condition.

Figure 6.- Continued.



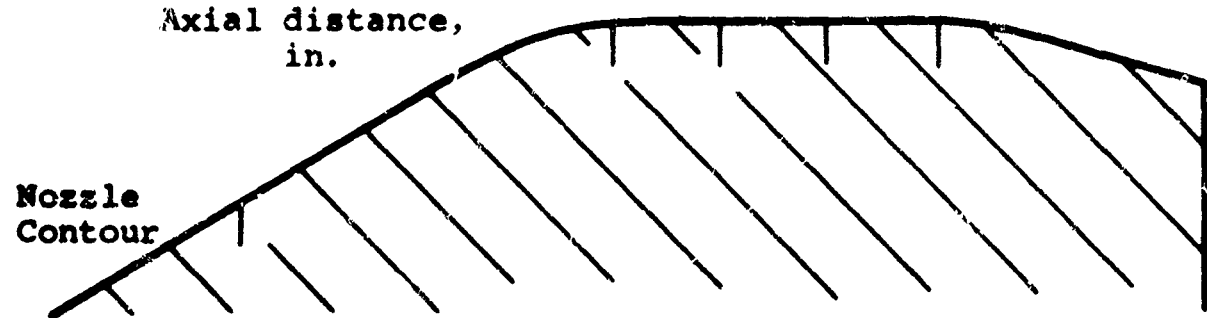
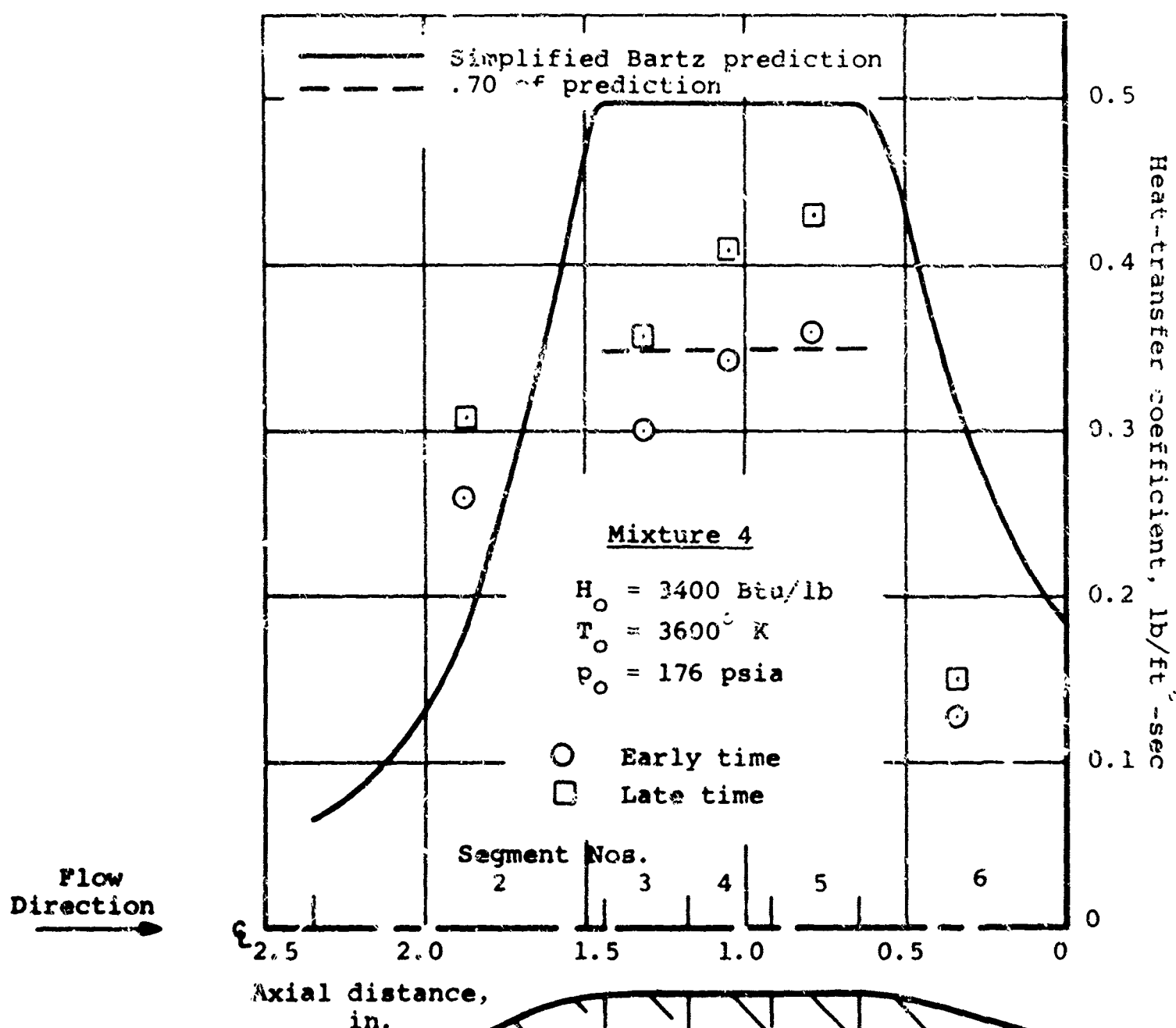
(d) 0.4-inch-diameter throat nozzle, low-temperature condition.

Figure 6.- Concluded.



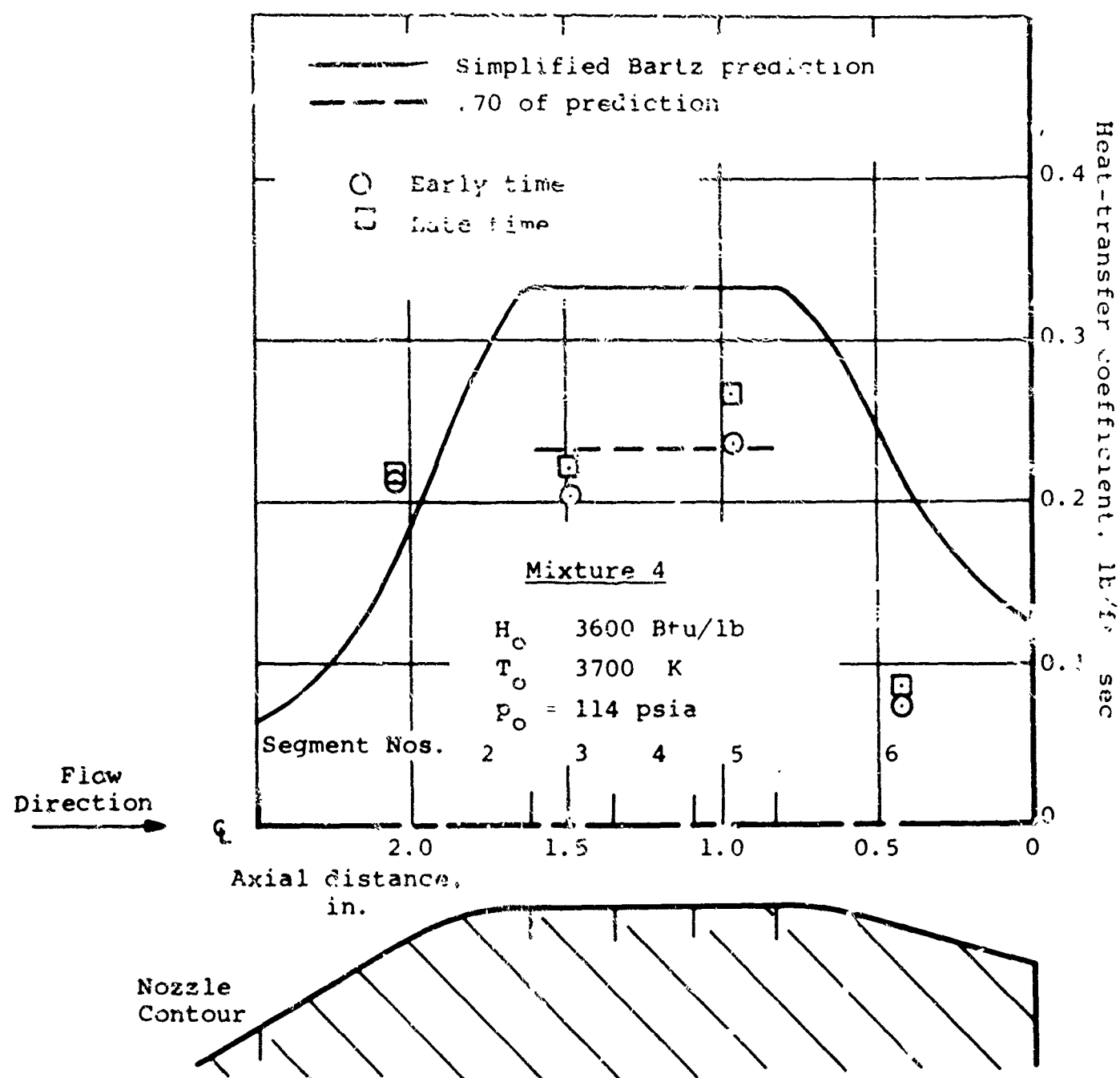
(a) 0.3-inch-diameter throat nozzle, high-temperature condition.

Figure 7.- Heat-transfer coefficient axial distribution, Mixture 4.



(b) 0.4-inch-diameter throat nozzle, high-temperature condition.

Figure 7.- Continued.



(c) 0.5-inch-diameter throat nozzle, high-temperature condition.

Figure 7. - Concluded.

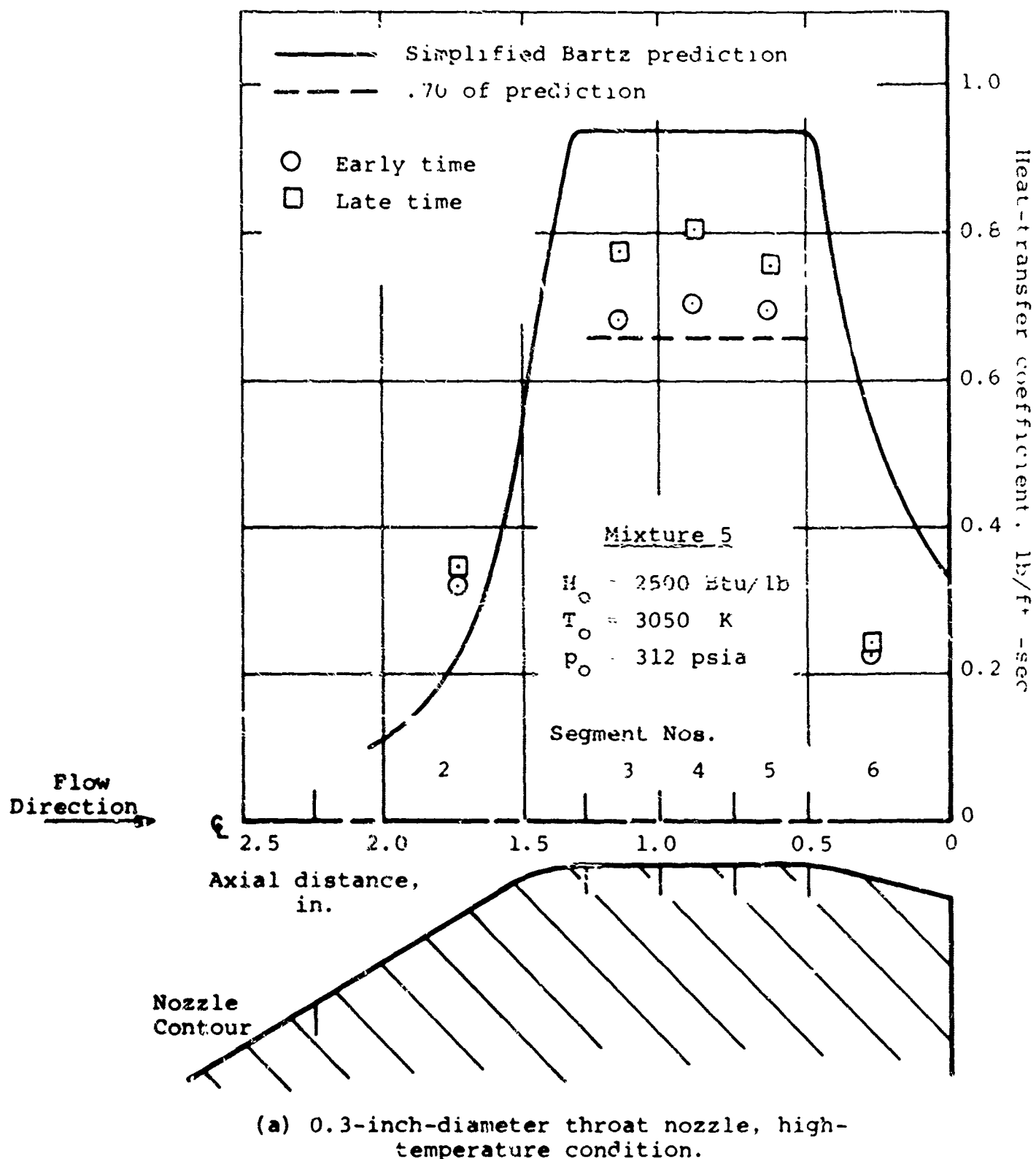
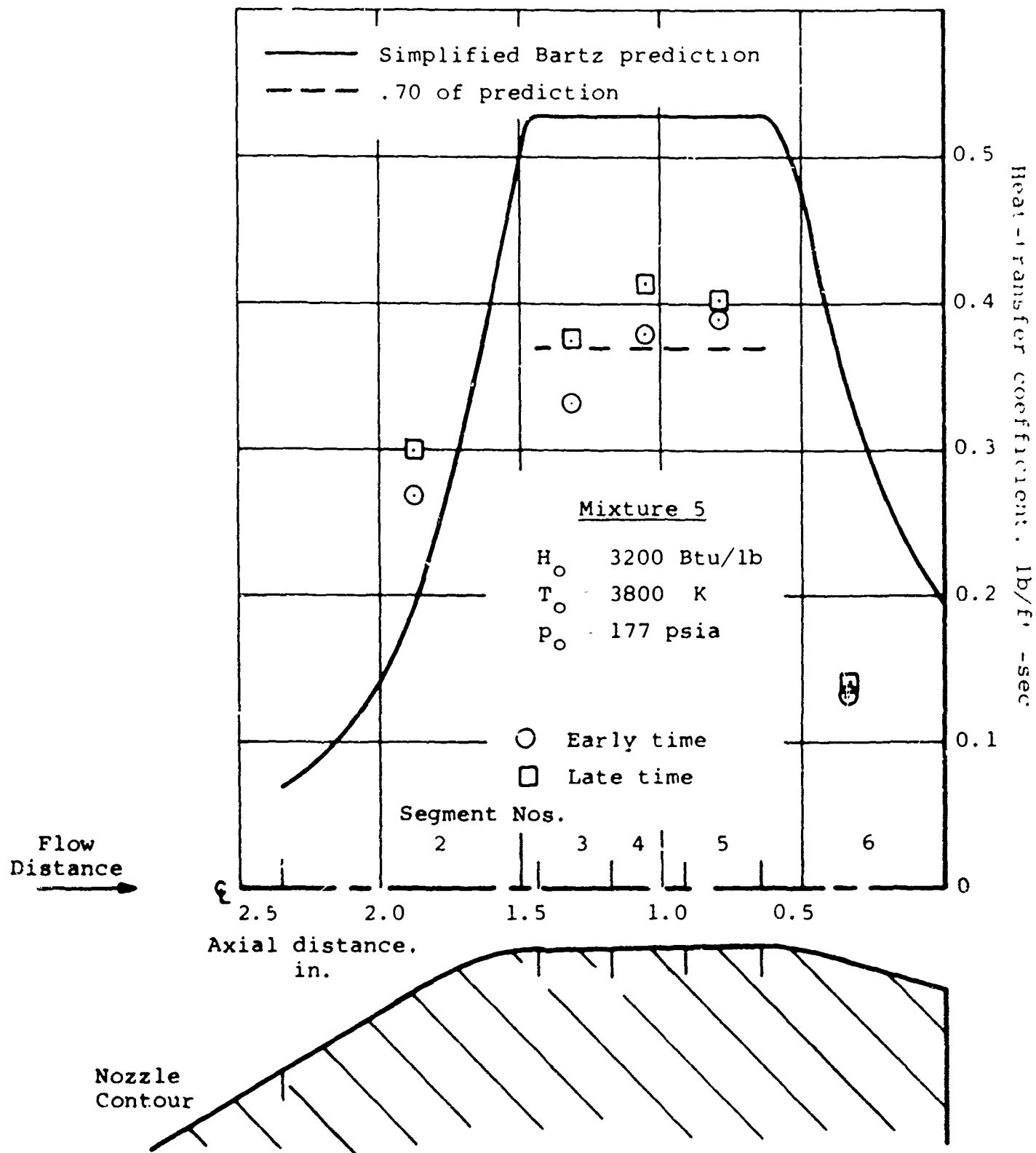
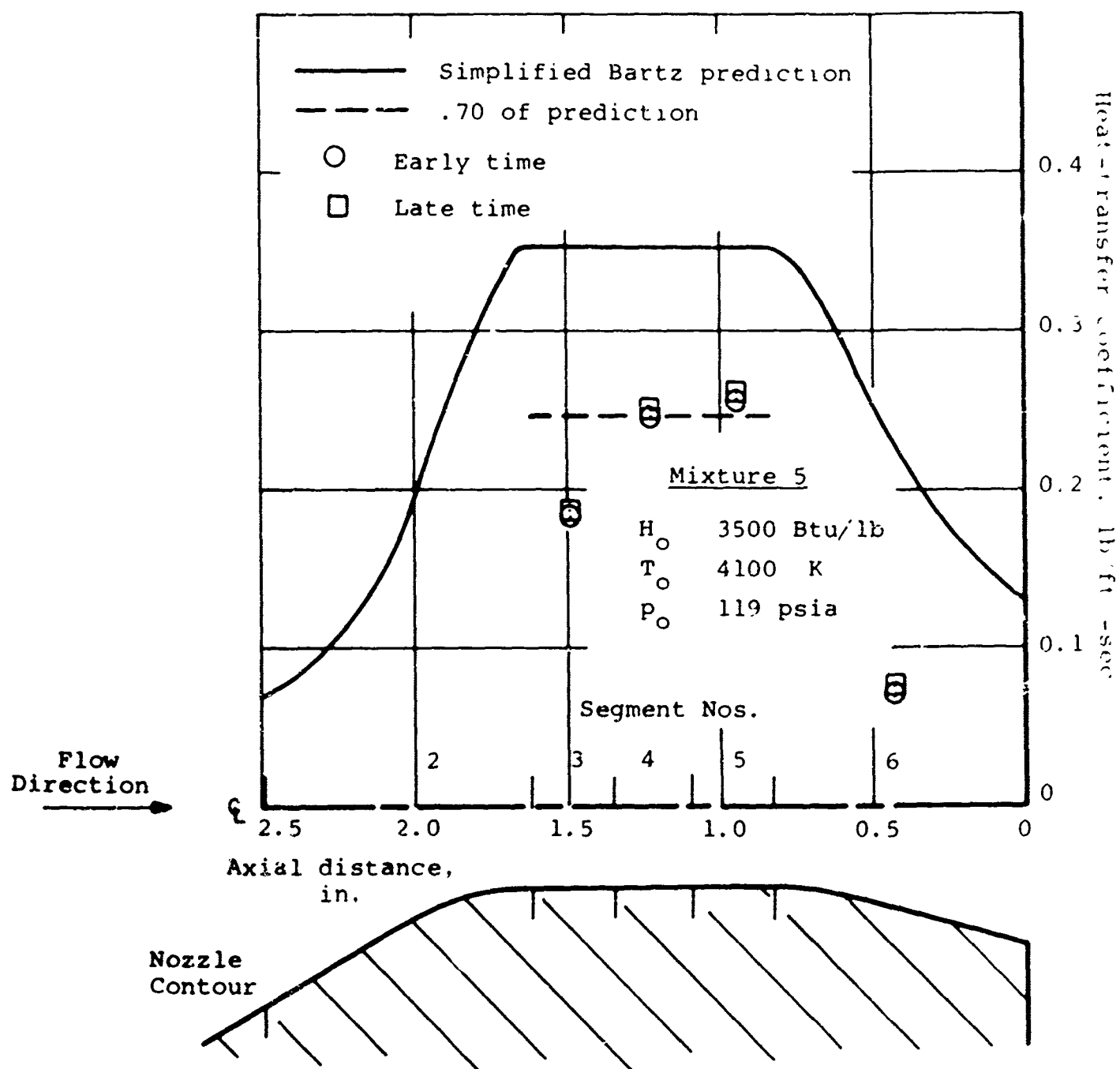


Figure 8.- Heat-transfer coefficient axial distribution, Mixture 5.



(b) 0.4-inch-diameter throat nozzle, high-temperature condition.

Figure 8.- Continued.



(c) 0.5-inch-diameter throat nozzle, high-temperature condition.

Figure 8.- Concluded.

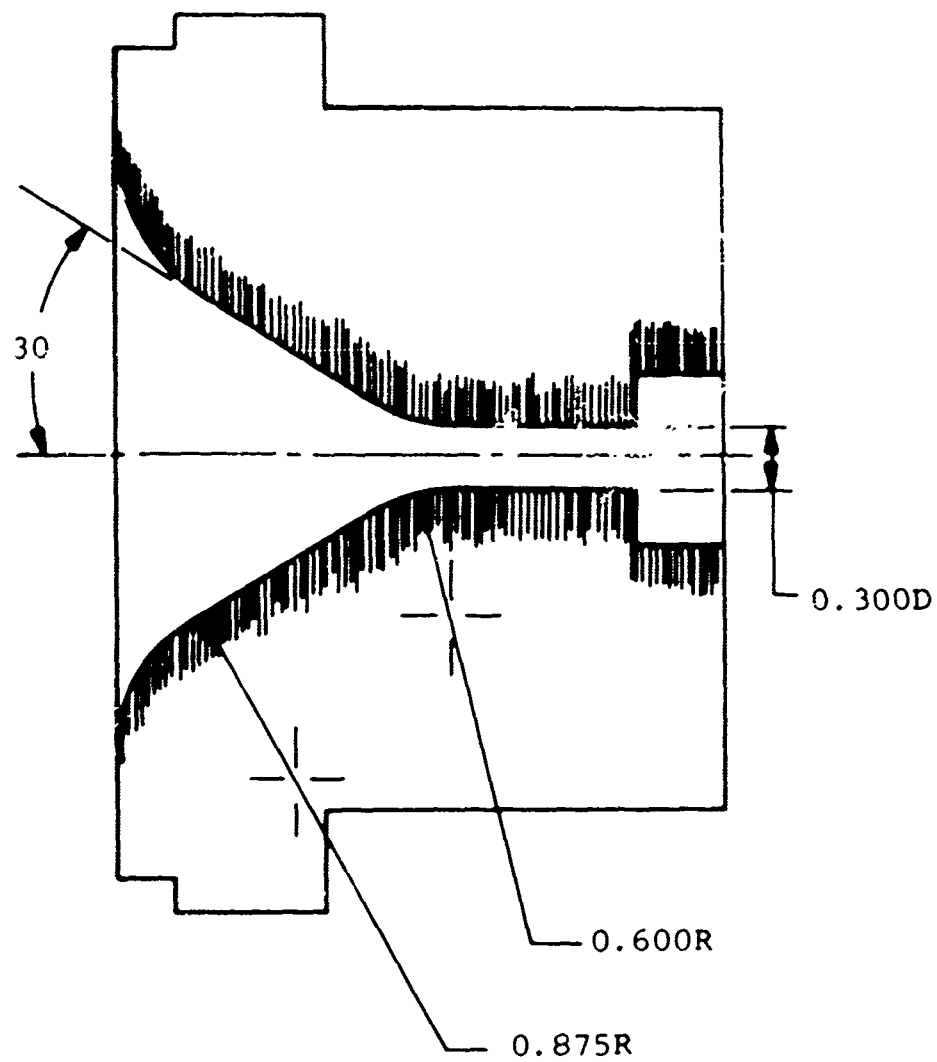


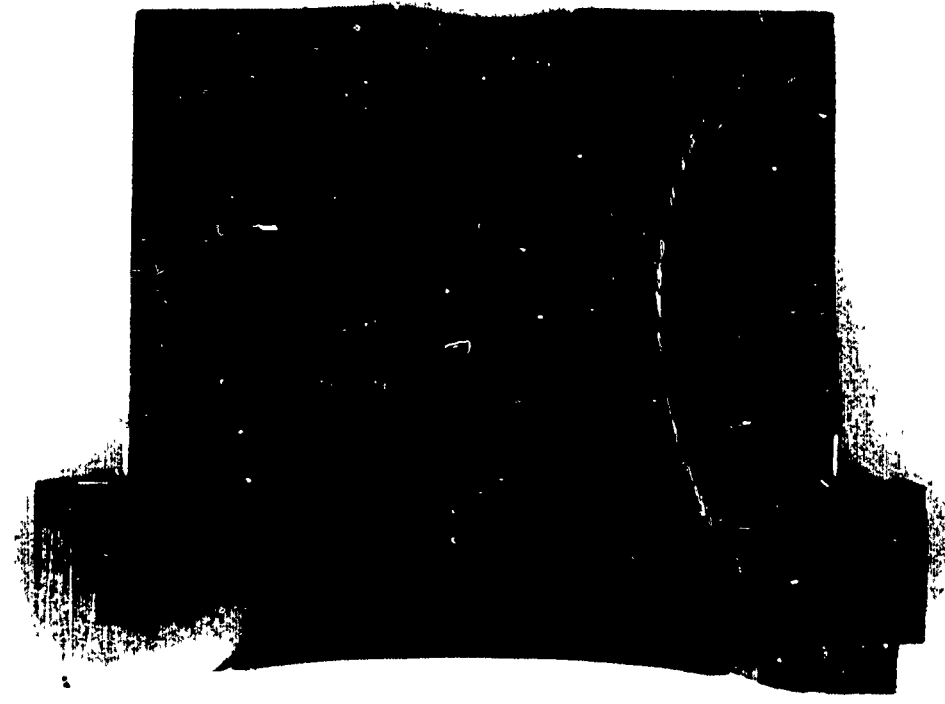
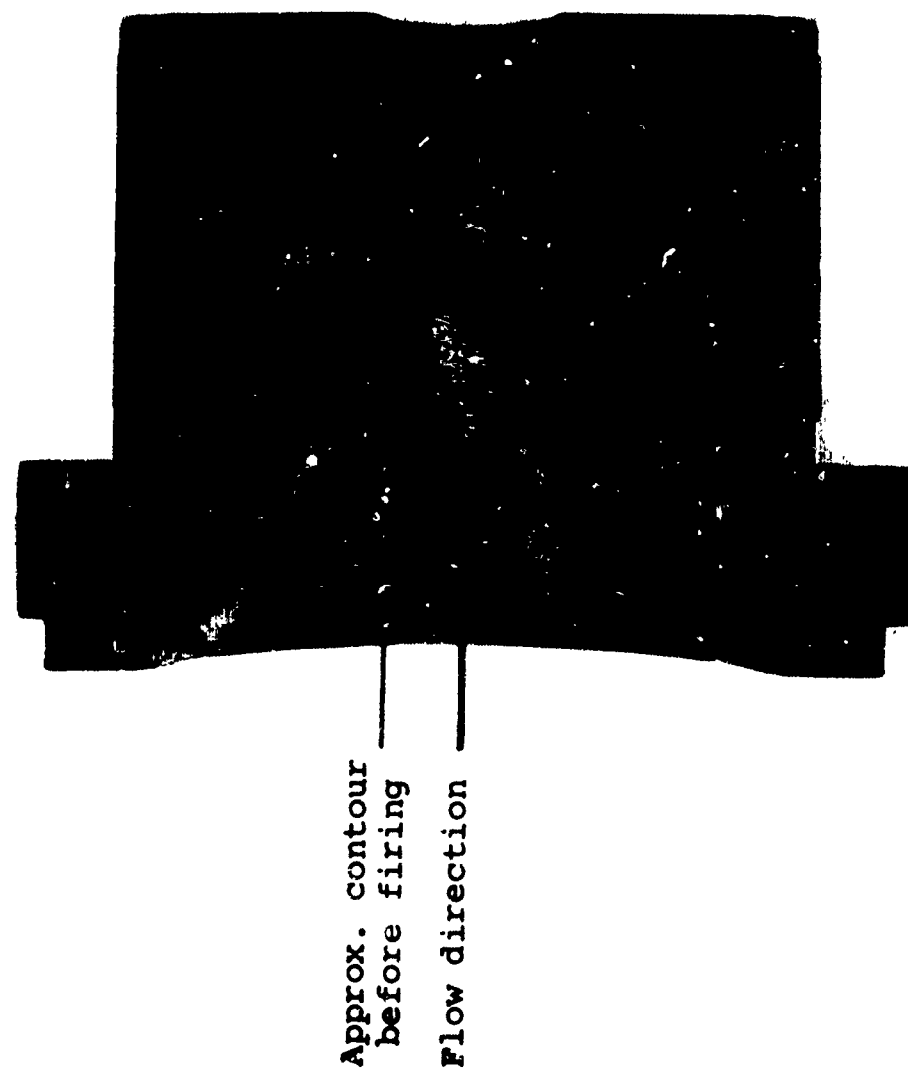
Figure 9.- Test-nozzle configuration,
0.3-inch-diameter throat.



(a) Nozzle E17, nominal conditions of $T_o = 3500^{\circ}$ K and $(p_o)_{\theta=0} = 300$ psia, $\theta_f = 30.7$ sec, Test No. 939.

(b) Nozzle E10, nominal conditions of $T_o = 3500^{\circ}$ K and $(p_o)_{\theta=0} = 300$ psia, $\theta_f = 30.8$ sec, Test No. 940.

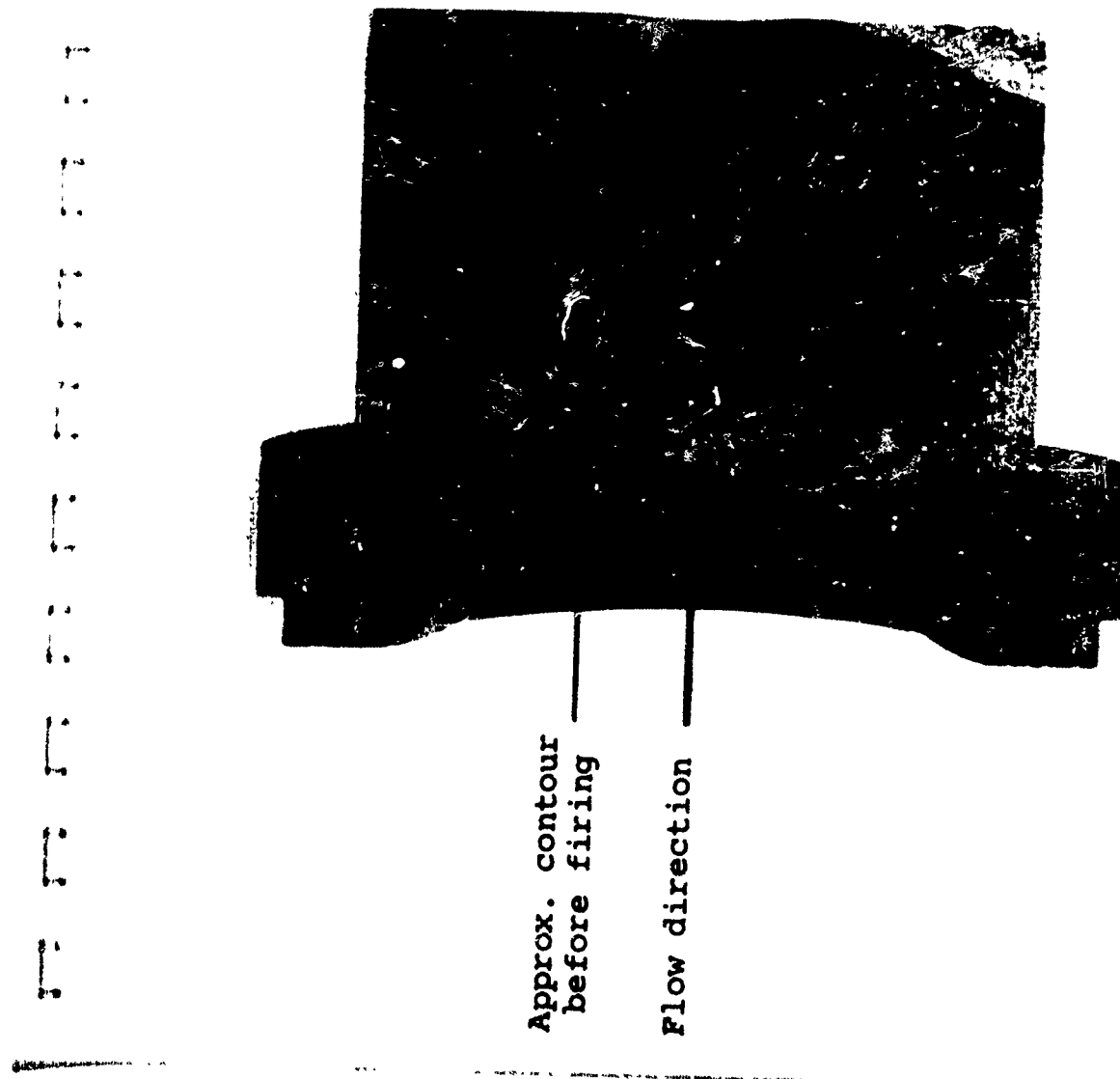
Figure 10.- Cut-away of fired nozzle, Graphite GX graphite, Mixture 4.



(c) Nozzle E19 nominal conditions of
 $T_o = 3500^{\circ}$ K and $(p_o)_{\theta=0} = 300$ psia,
 $\theta_f = 30.2$ sec, Test No. 997.

(d) Nozzle E31 nominal conditions of
 $T_o = 3500^{\circ}$ K and $(p_o)_{\theta=0} = 175$ psia,
 $\theta_f = 30.4$ sec, Test No. 998.

Figure 10.- Continued.



(e) Nozzle E13 nominal conditions of
 $T_o = 27500$ K and $(p_o)_{\theta=0} = 300$ psia,
 $\theta_f = 31.1$ sec, Test No. 1039.

(f) Nozzle E12, nominal conditions of
 $T_o = 20000$ K and $(p_o)_{\theta=0} = 300$ psia,
 $\theta_f = 30.7$ sec, Test No. 1023.

Figure 10.- Concluded.

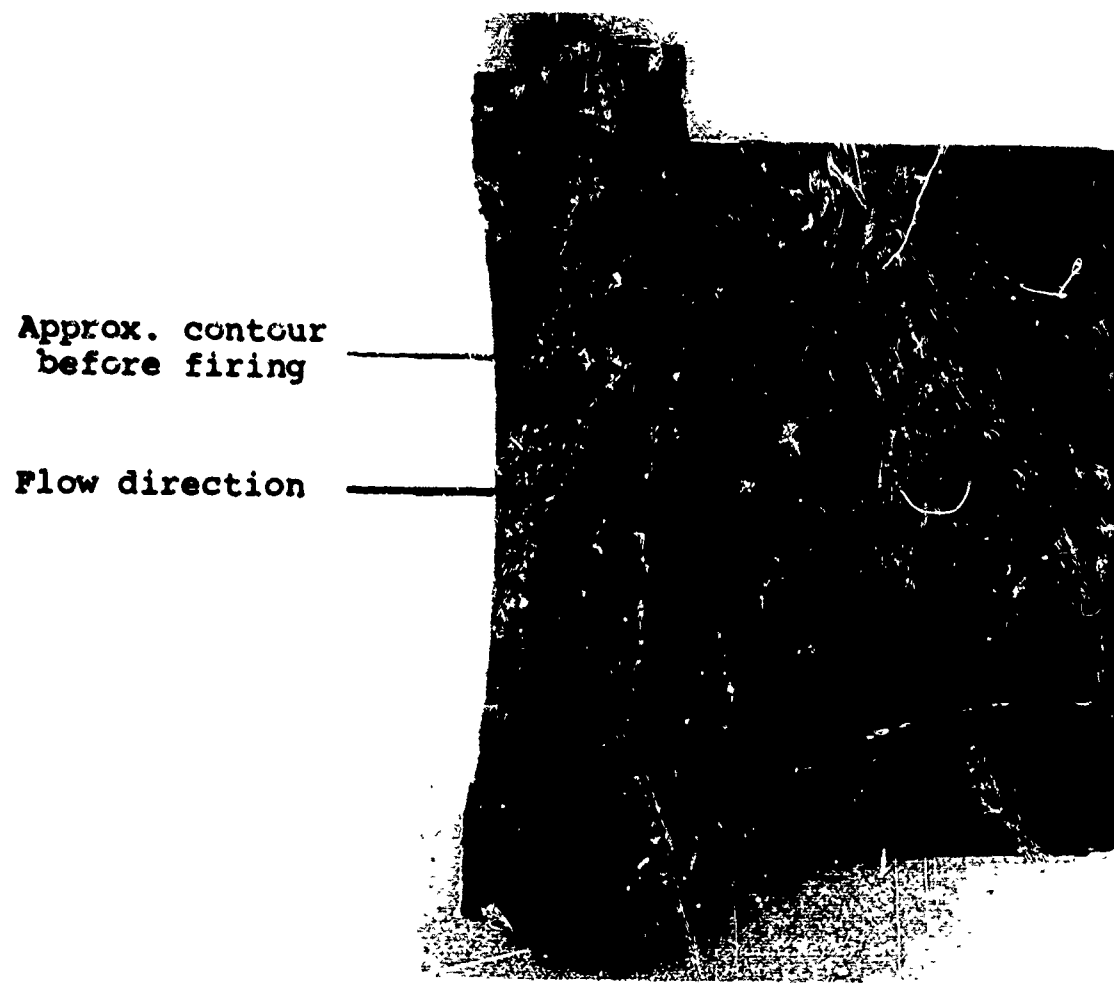
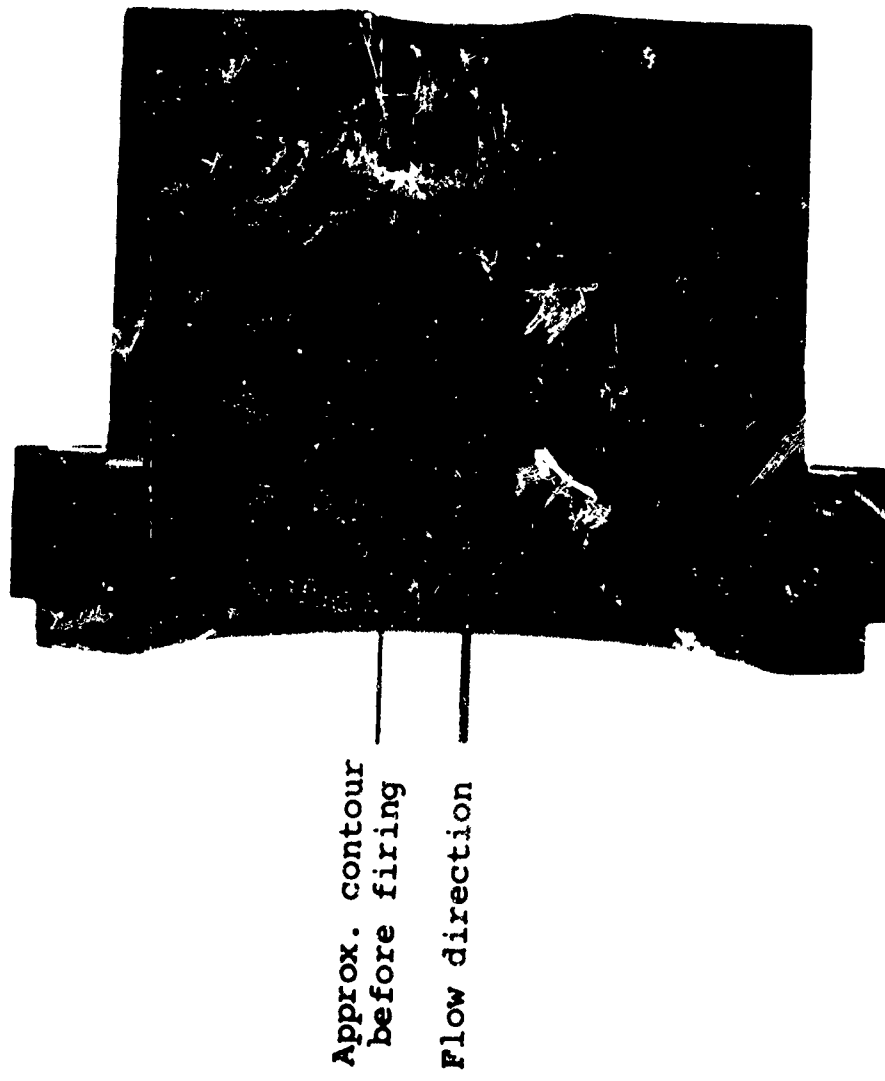


Figure 11.- Cut-away of fired nozzle, ATJ graphite,
Mixture 4. Nozzle E43, nominal conditions of
 $T_o = 3500^\circ \text{ K}$ and $(p_o)_{\theta=0} = 300 \text{ psia}$, $\theta_f = 30.2 \text{ sec}$,
Test No. 1000.

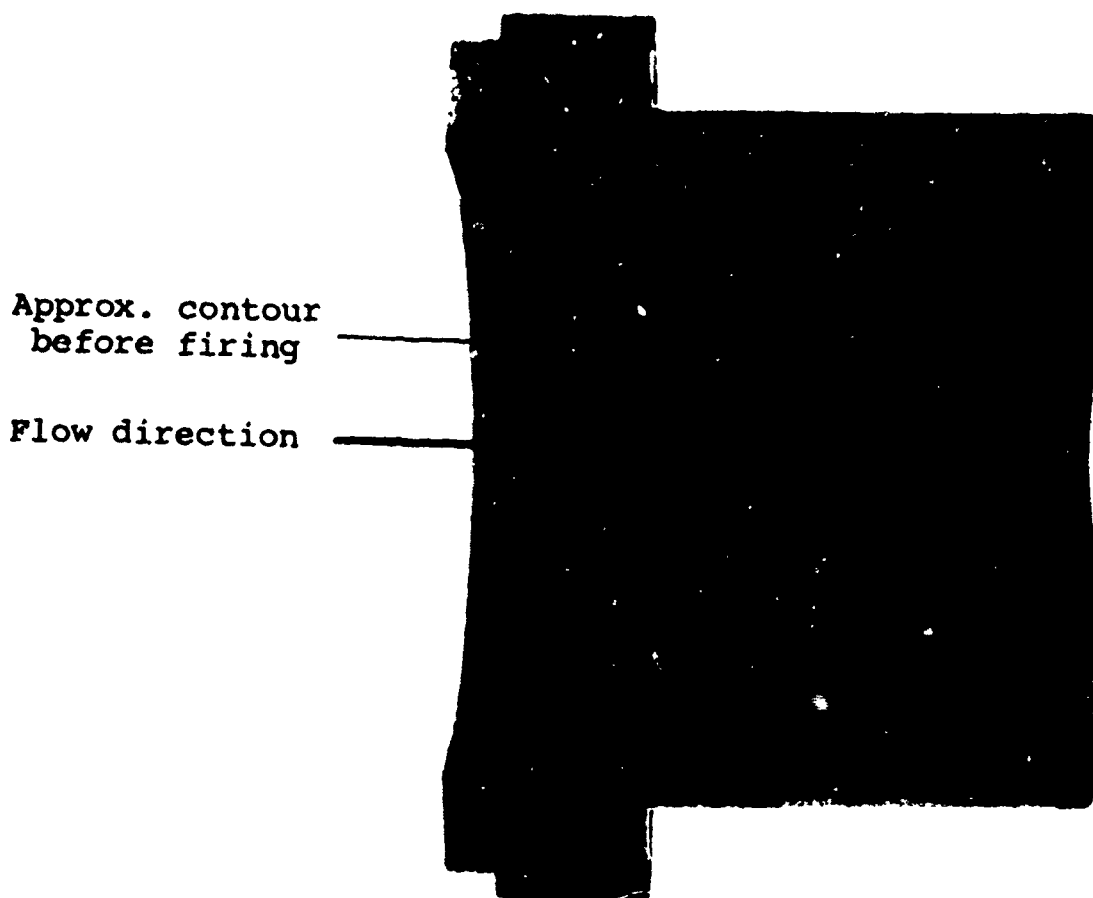
BLANK PAGE



(a) Nozzle E38, nominal conditions of $T_o = 3500^\circ K$ and $(p_o)_{\theta=0} = 300$ psia, $\theta_f = 30.3$ sec, Test No. 1001

(b) Nozzle E39, nominal conditions of $T_o = 2750^\circ K$ and $(p_o)_{\theta=0} = 300$ psia, $\theta_f = 30.5$ sec, Test No. 1040.

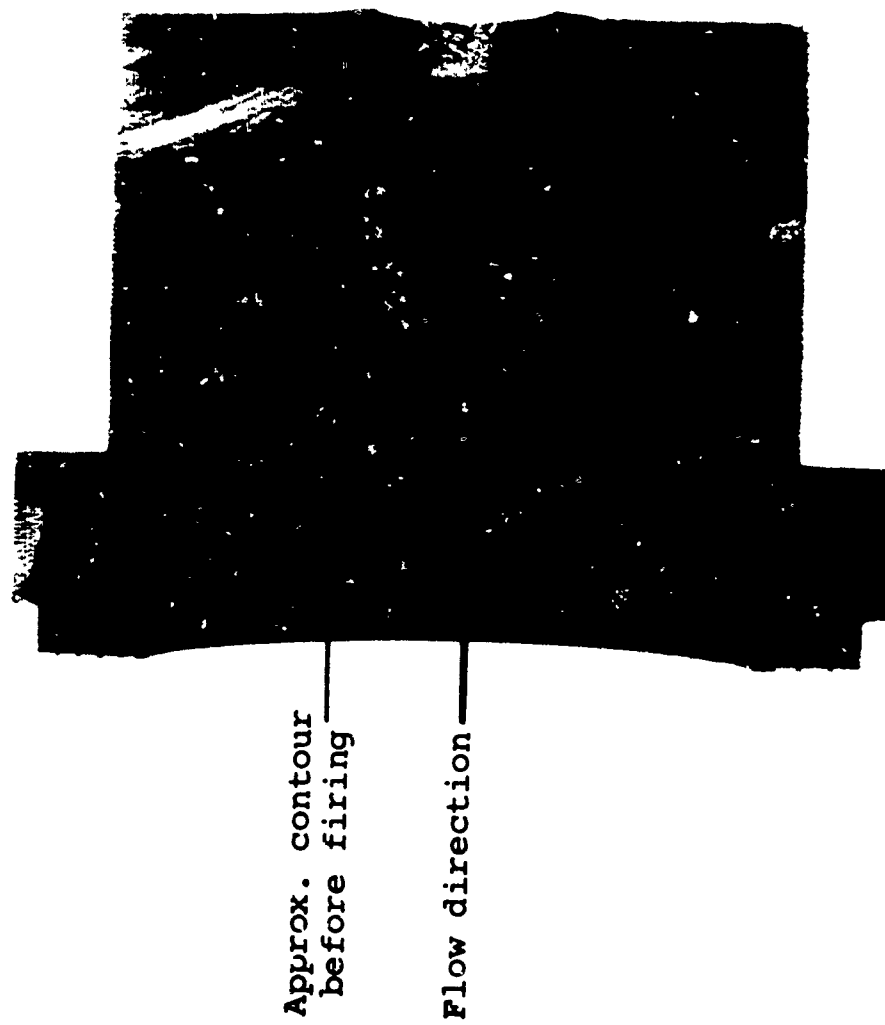
Figure 12.- Cut-away of fired nozzle, MK4500 graphite phenolic, Mixture 4.



(c) Nozzle E36, nominal conditions of
 $T_o = 2000^{\circ} \text{ K}$ and $(p_o)_{\theta=0} = 300 \text{ psia}$,
 $\theta_f = 30.7 \text{ sec}$, Test No. 1024.

Figure 12.- Concluded.

BLANK PAGE



(a) Nozzle E22, nominal conditions of $T_o = 3500^{\circ}$ K and $(p_o)_{\theta=0} = 300$ psia, $\theta_f = 19.4$ sec, Test No. 941.

(b) Nozzle E26, nominal conditions of $T_o = 2750^{\circ}$ K and $(p_o)_{\theta=0} = 300$ psia, $\theta_f = 30.6$ sec, Test No. 1038.

Figure 13.- Cut-away of fired nozzle, MX2600 silica phenolic, Mixture 4.



Approx. contour
before firing

Flow direction

(a) Nozzle E18, nominal conditions of $T_o = 3500^\circ K$ and $(p_o)_{\theta=0} = 300$ psia, $\theta_f = 14.1$ and 14.5 sec, Test Nos. 957 and 958.

(b) Nozzle E32, nominal conditions of $T_o = 3500^\circ K$ and $(p_o)_{\theta=0} = 175$ psia, $\theta_f = 30.4$ sec, Test No. 1004.

Figure 14.- Cut-away of fired nozzle, Graphite GX graphite, Mixture 5.

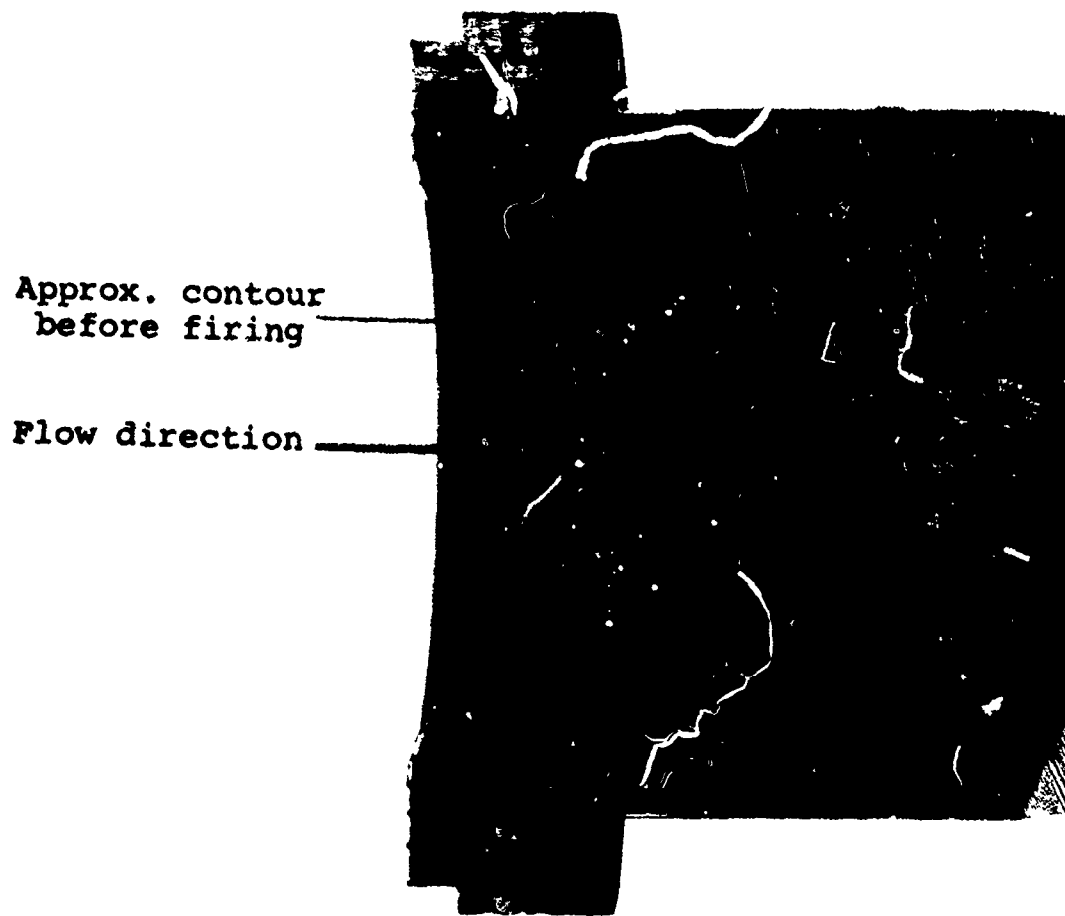
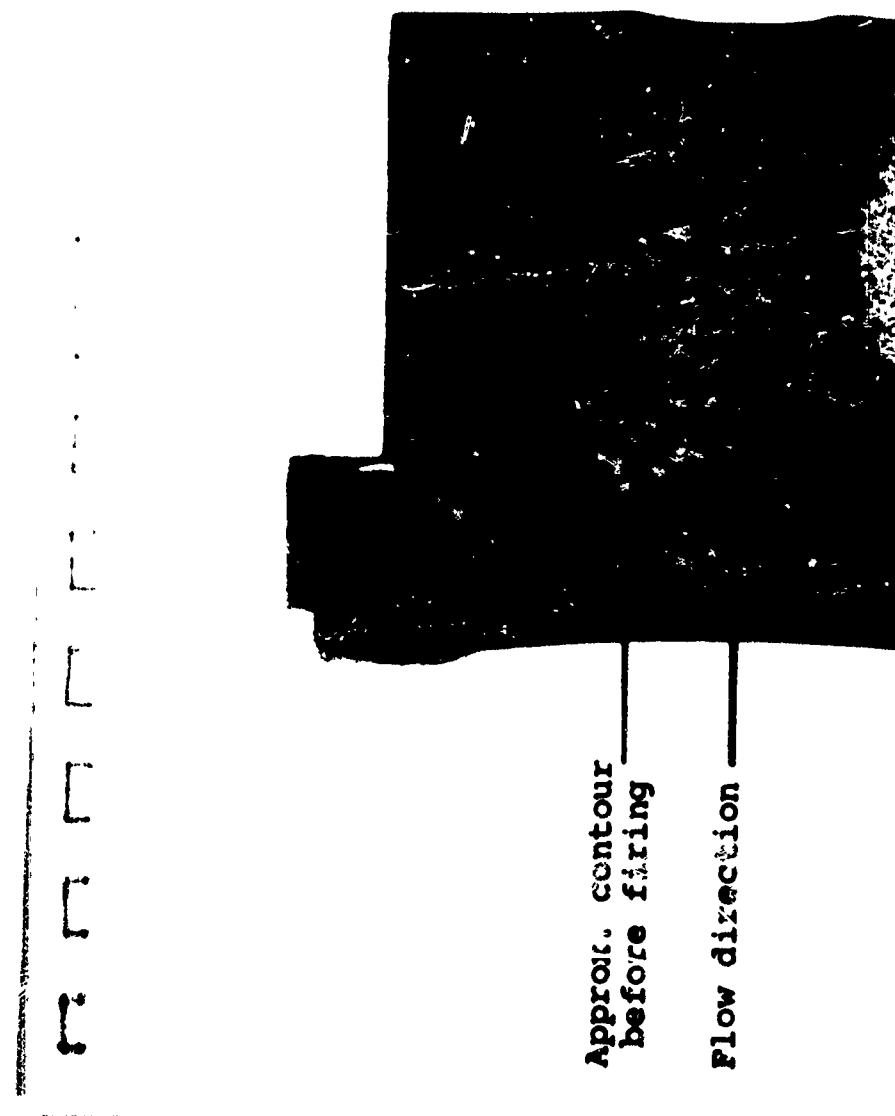


Figure 15.- Cut-away of fired nozzle, ATJ graphite,
Mixture 5. Nozzle E42, nominal conditions of
 $T_o = 3500^\circ \text{ K}$ and $(p_o)_{\theta=0} = 300 \text{ psia}$, $\theta_f = 30.4 \text{ sec}$,
Test No. 1005.

BLANK PAGE

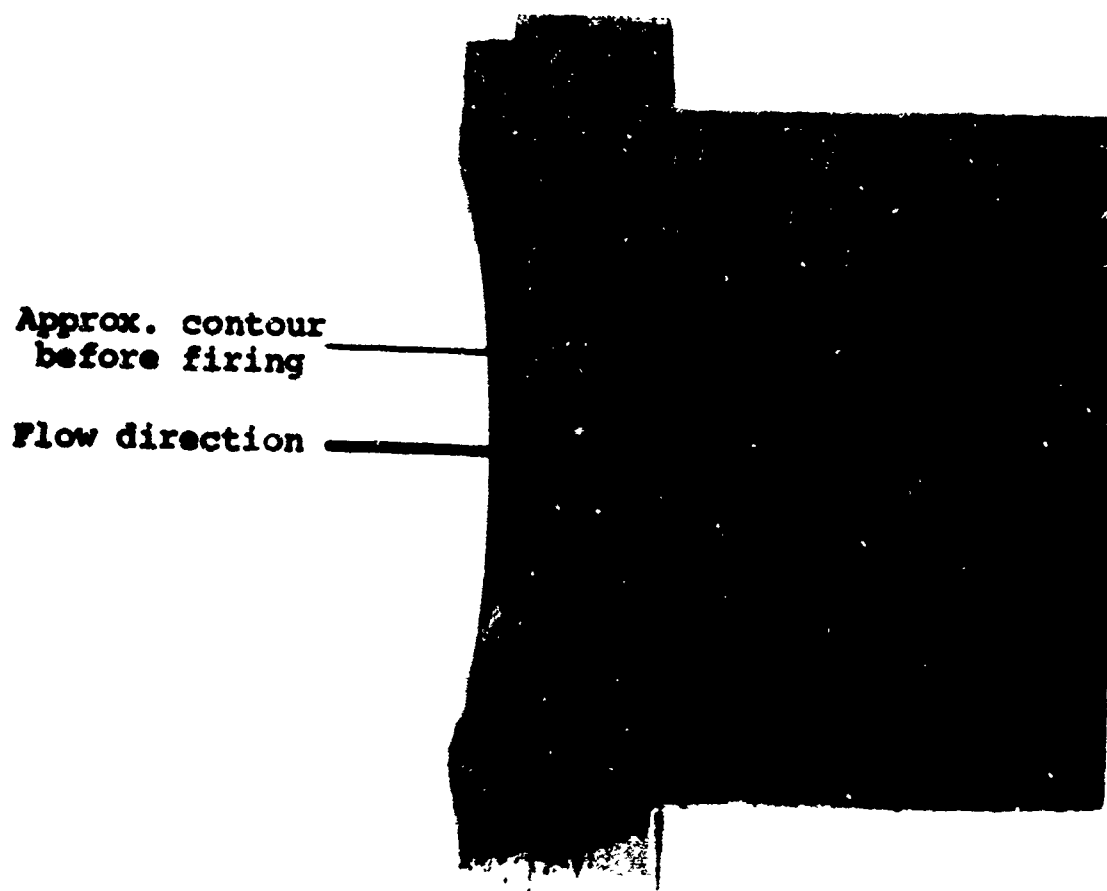


(a) Nozzle E35, nominal conditions of $T_o = 35000^\circ K$ and $(P_o)_{\theta=0} = 300$ psia, $\theta_f = 26.2$ sec, Test No. 1006.



(b) Nozzle E40 nominal conditions of $T_o = 27500^\circ K$ and $(P_o)_{\theta=0} = 300$ psia, $\theta_f = 35.3$ sec, Test No. 1043.

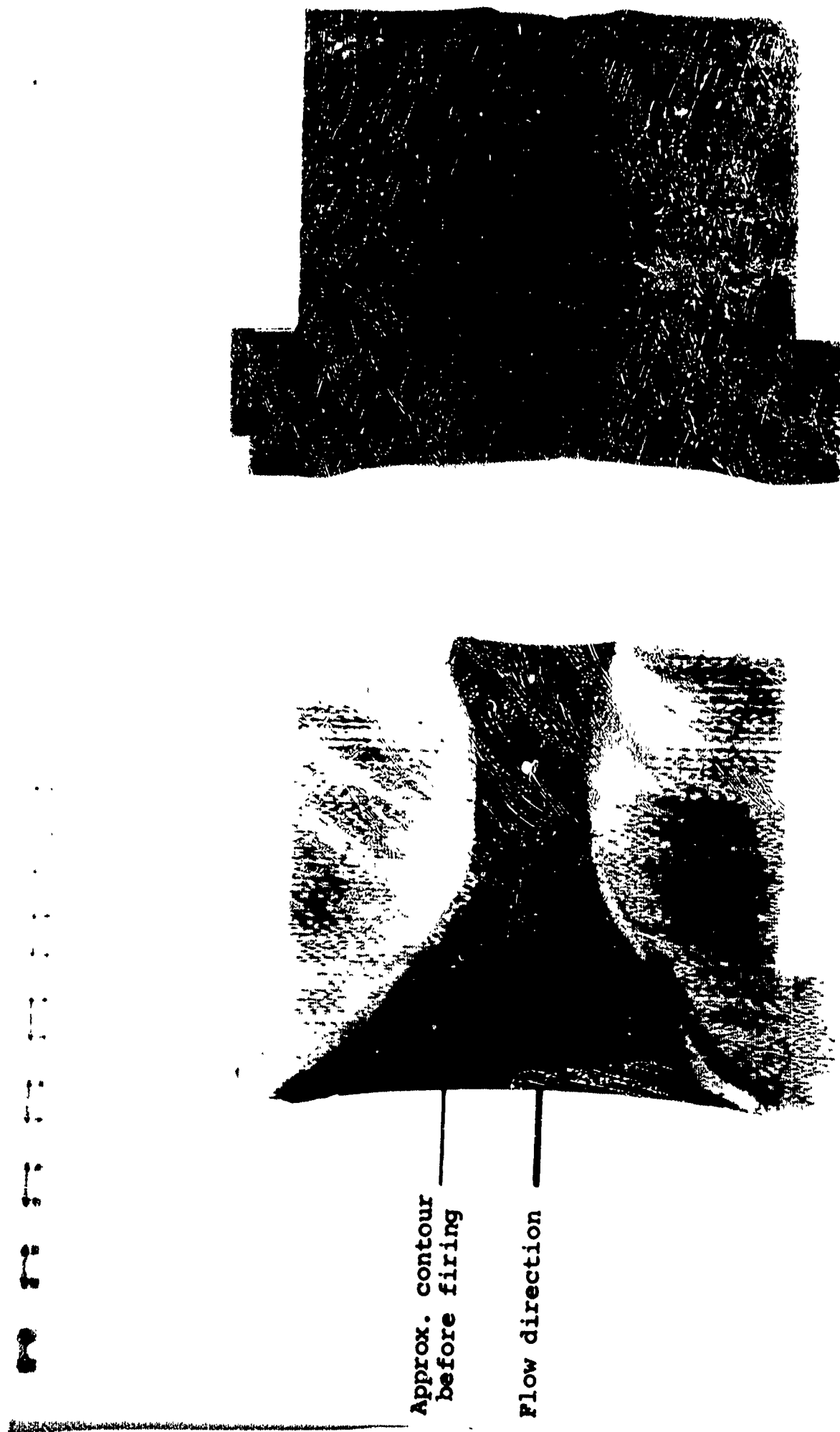
Figure 16.- Cut-away of fixed nozzle, MK4500 : aphite no. 1040 mixture 5.



(c) Nozzle E37, nominal conditions of
 $T_o = 2000^{\circ}$ K and $(p_o)_{\theta=0} = 300$ psia,
 $\theta_f = 6.5$ and 16.1 sec, Test Nos.
1026 and 1028.

Figure 16.- Concluded.

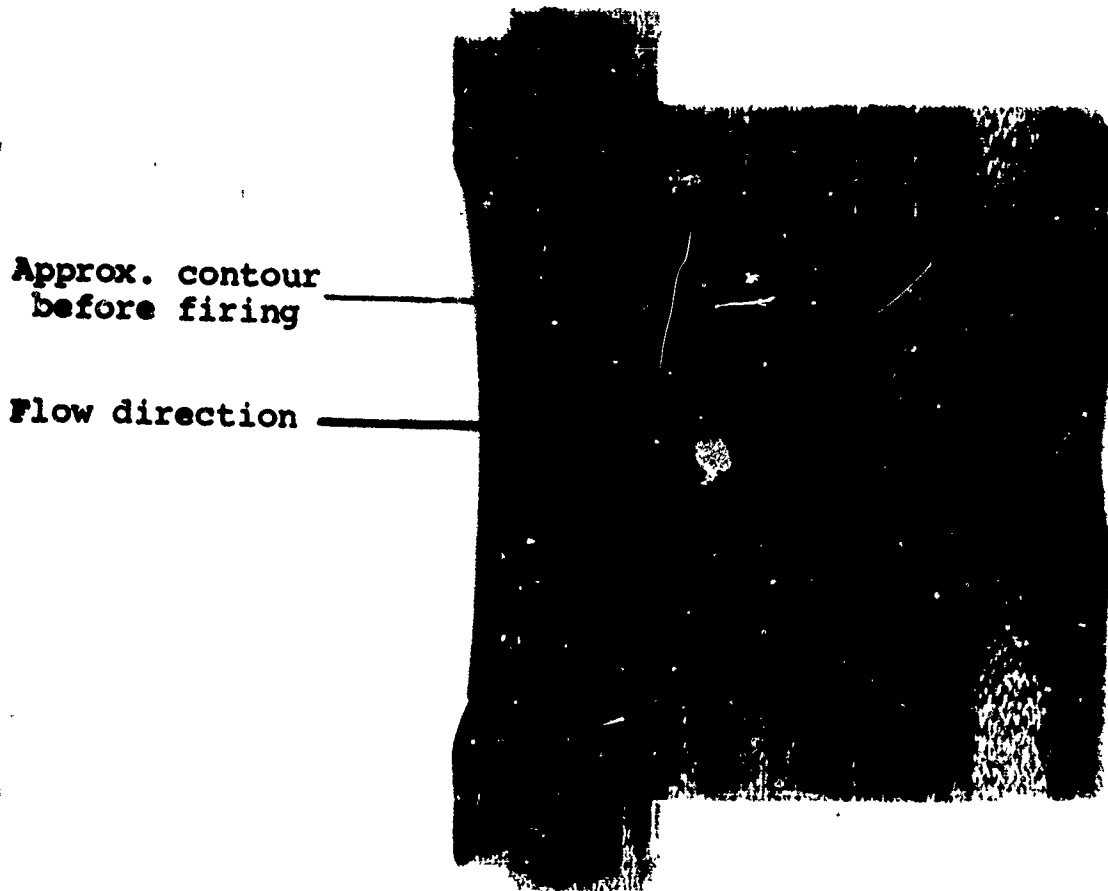
BLANK PAGE



(a) Nozzle E24, nominal conditions of $T_o = 3500^{\circ}$ K and $(p_o)_{\theta=0} = 300$ psia, $\theta_f = 20.8$ sec, Test No. 960.

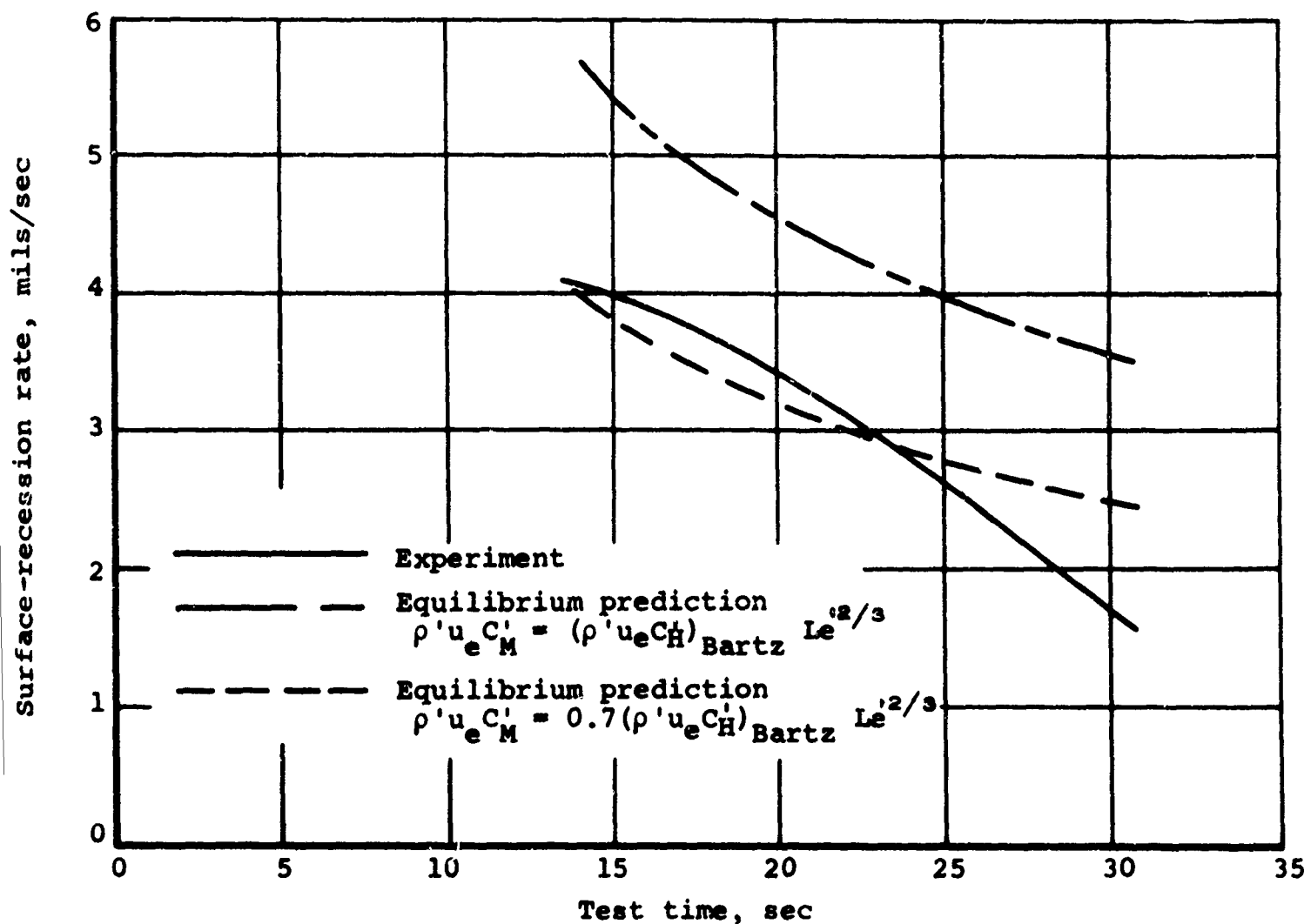
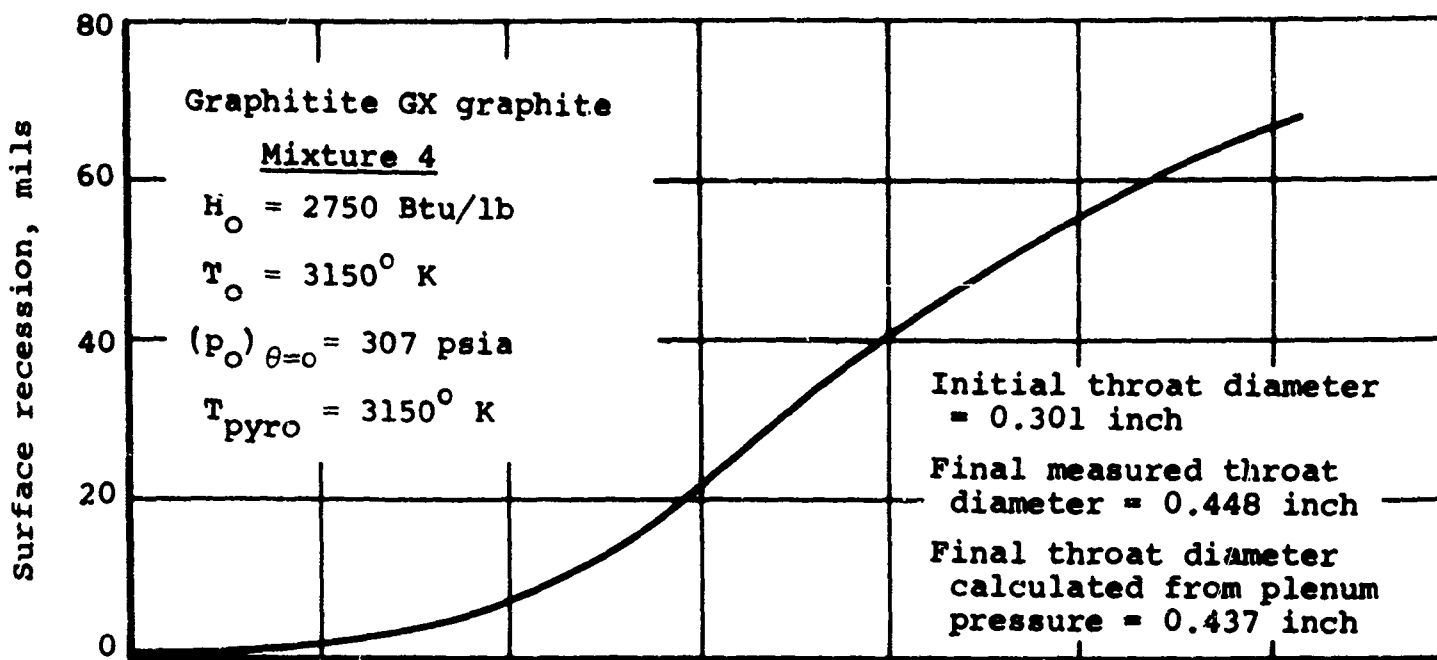
(b) Nozzle E27, nominal conditions of $T_o = 2750^{\circ}$ K and $(p_o)_{\theta=0} = 300$ psia, $\theta_f = 30.6$ sec, Test No. 1042.

Figure 17.-- Cut-away of fired nozzle, MX2600 silica phenolic, Mixture 5.



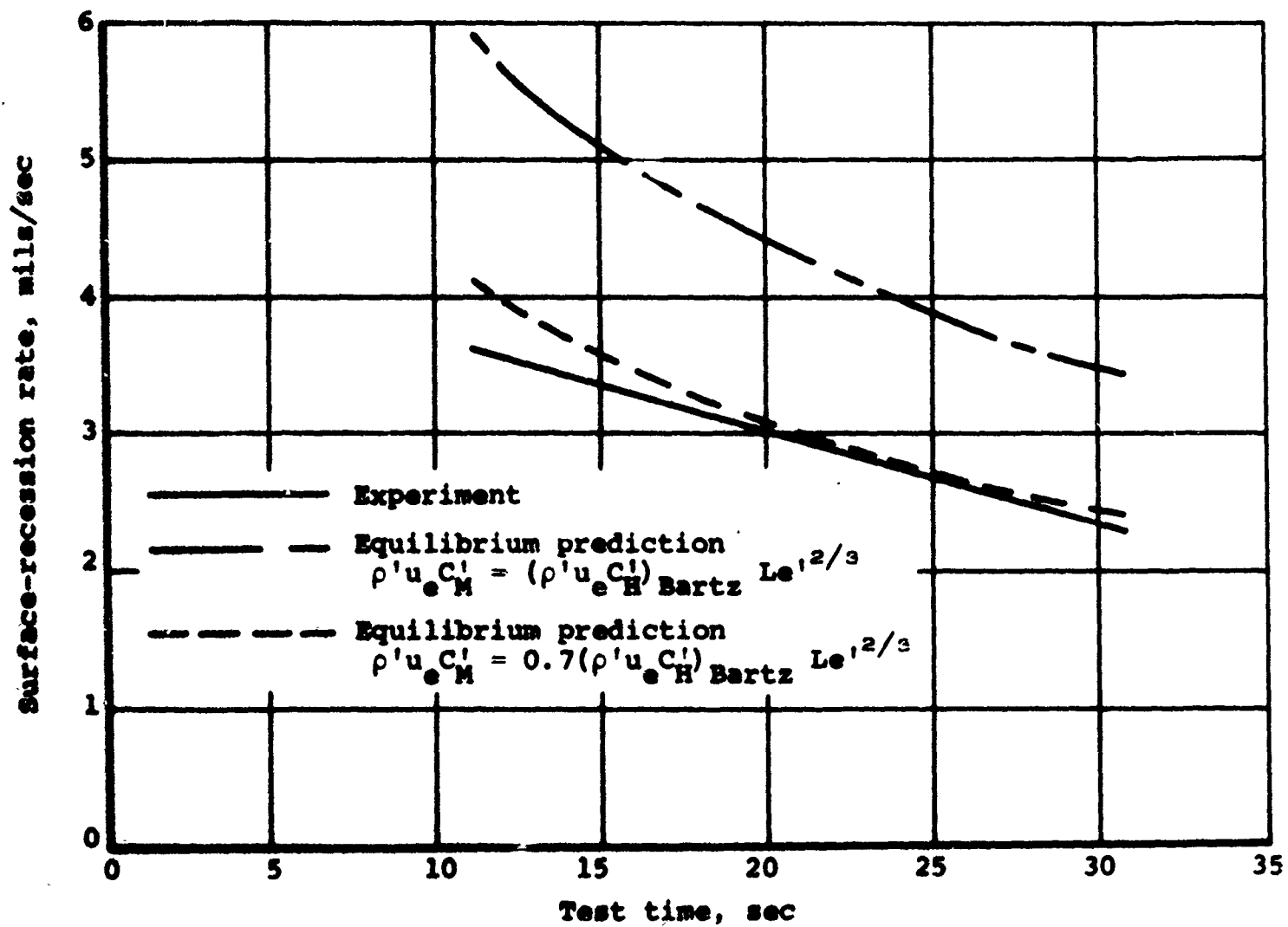
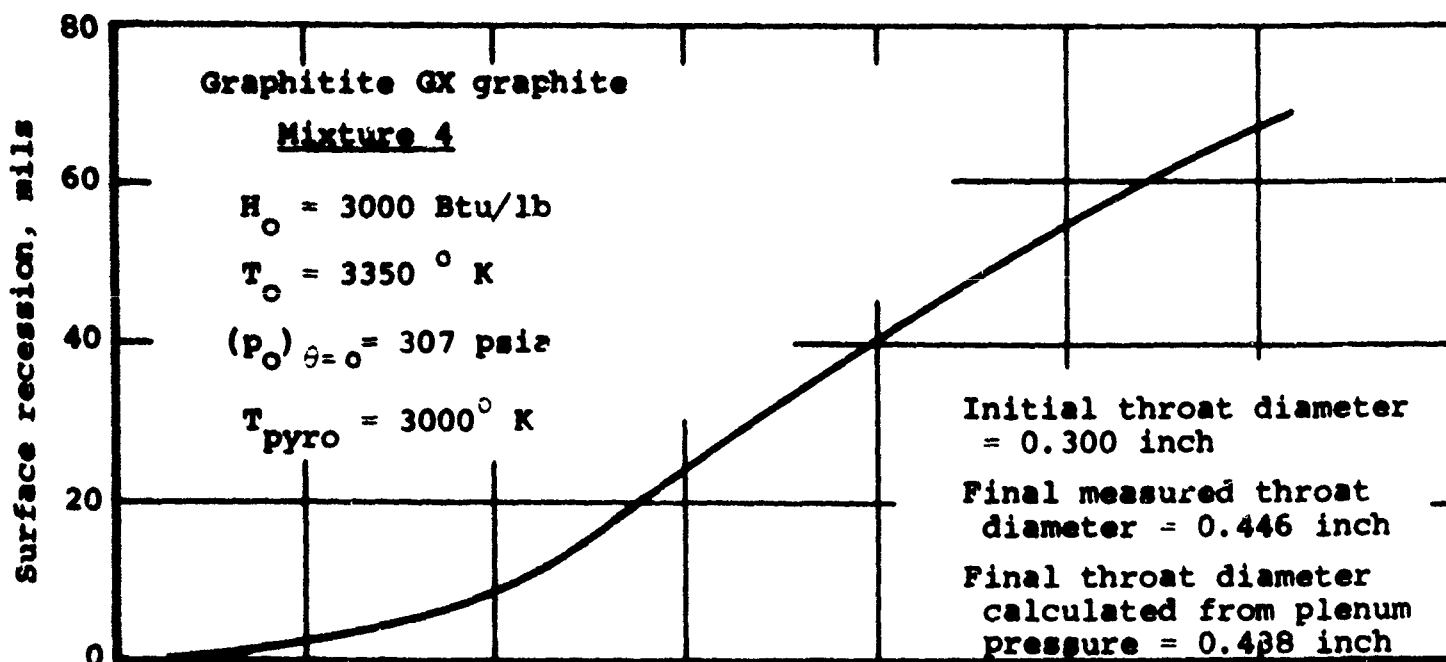
(c) Nozzle E25, nominal conditions of
 $T_o = 2000^{\circ} \text{ K}$ and $(p_o)_{\theta=0} = 300 \text{ psia}$,
 $\theta_f = 29.7 \text{ sec}$, Test No. 1031.

Figure 17.- Concluded.



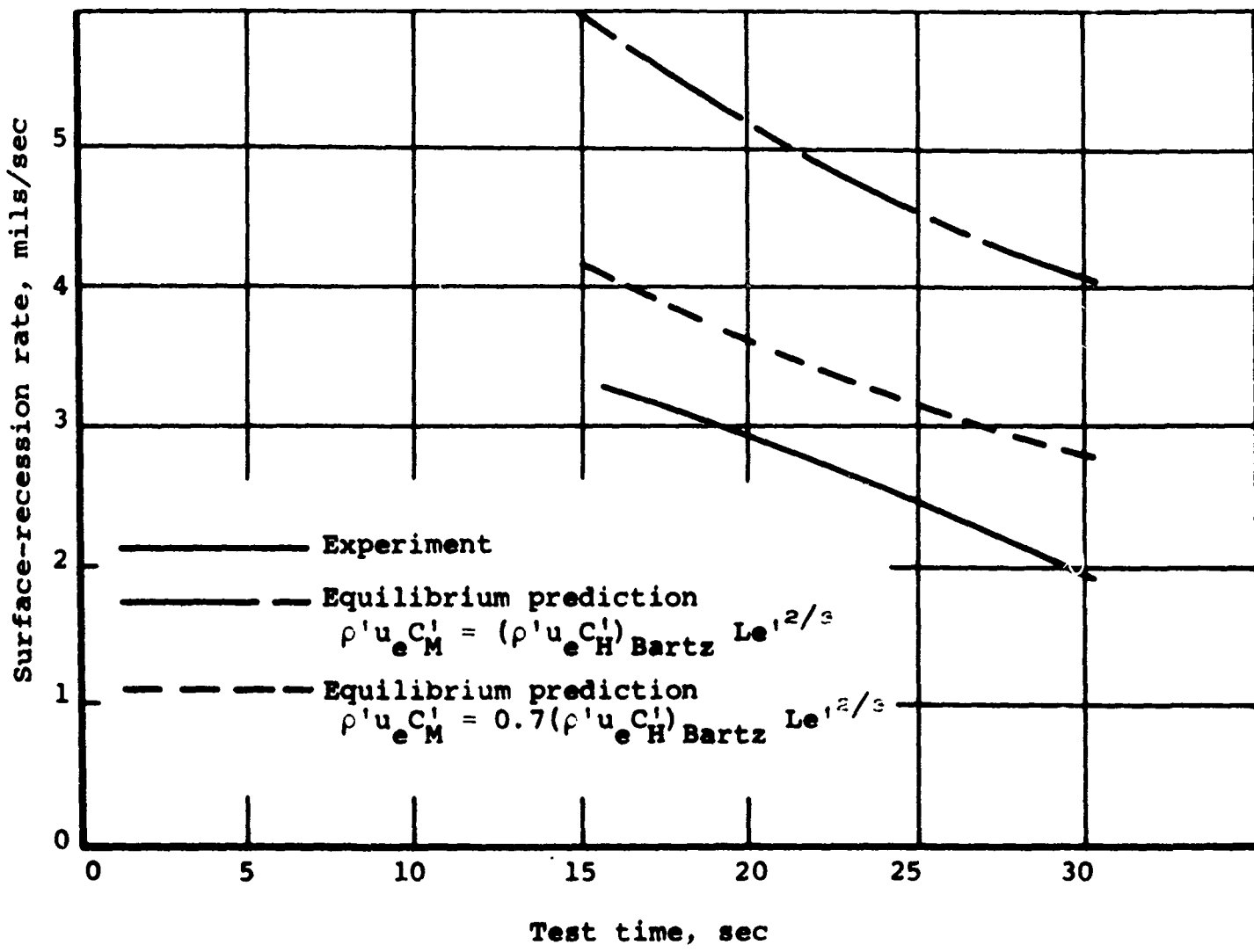
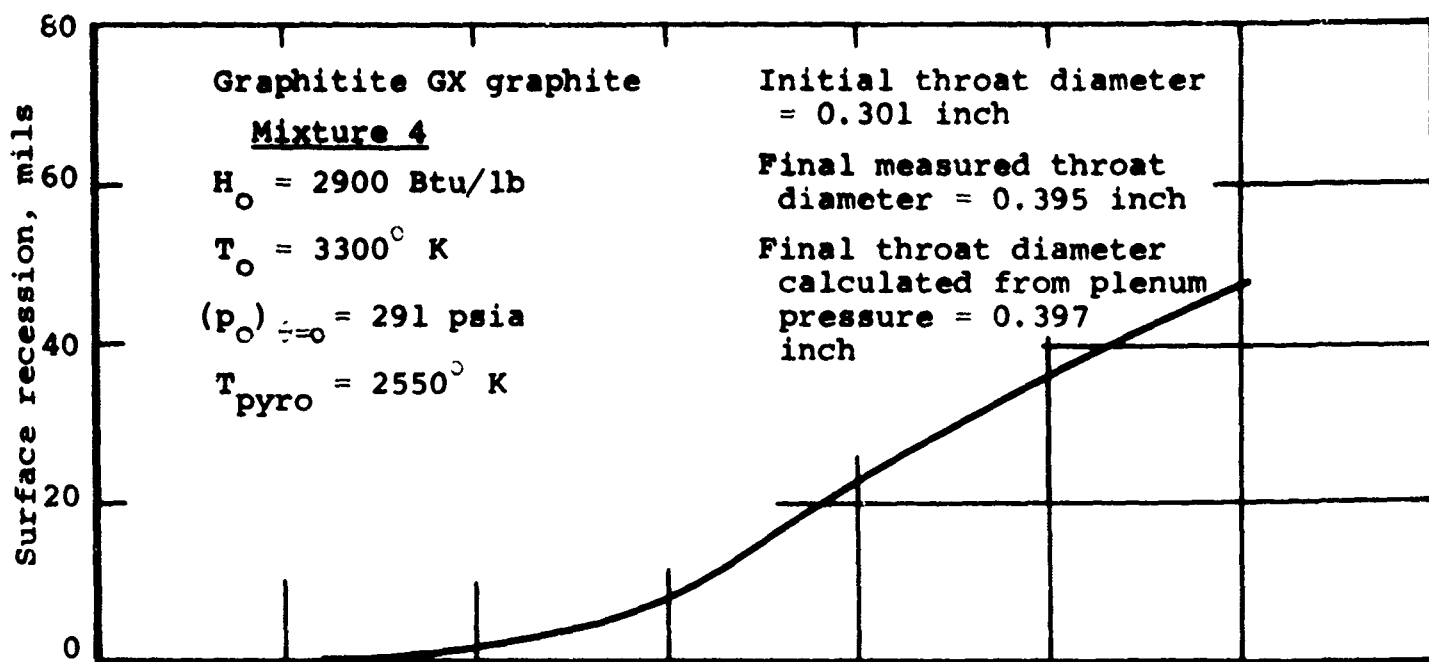
(a) Nozzle E17, Test No. 939.

Figure 18.- Surface recession and surface recession rate, Graphite GX graphite, Mixture 4.



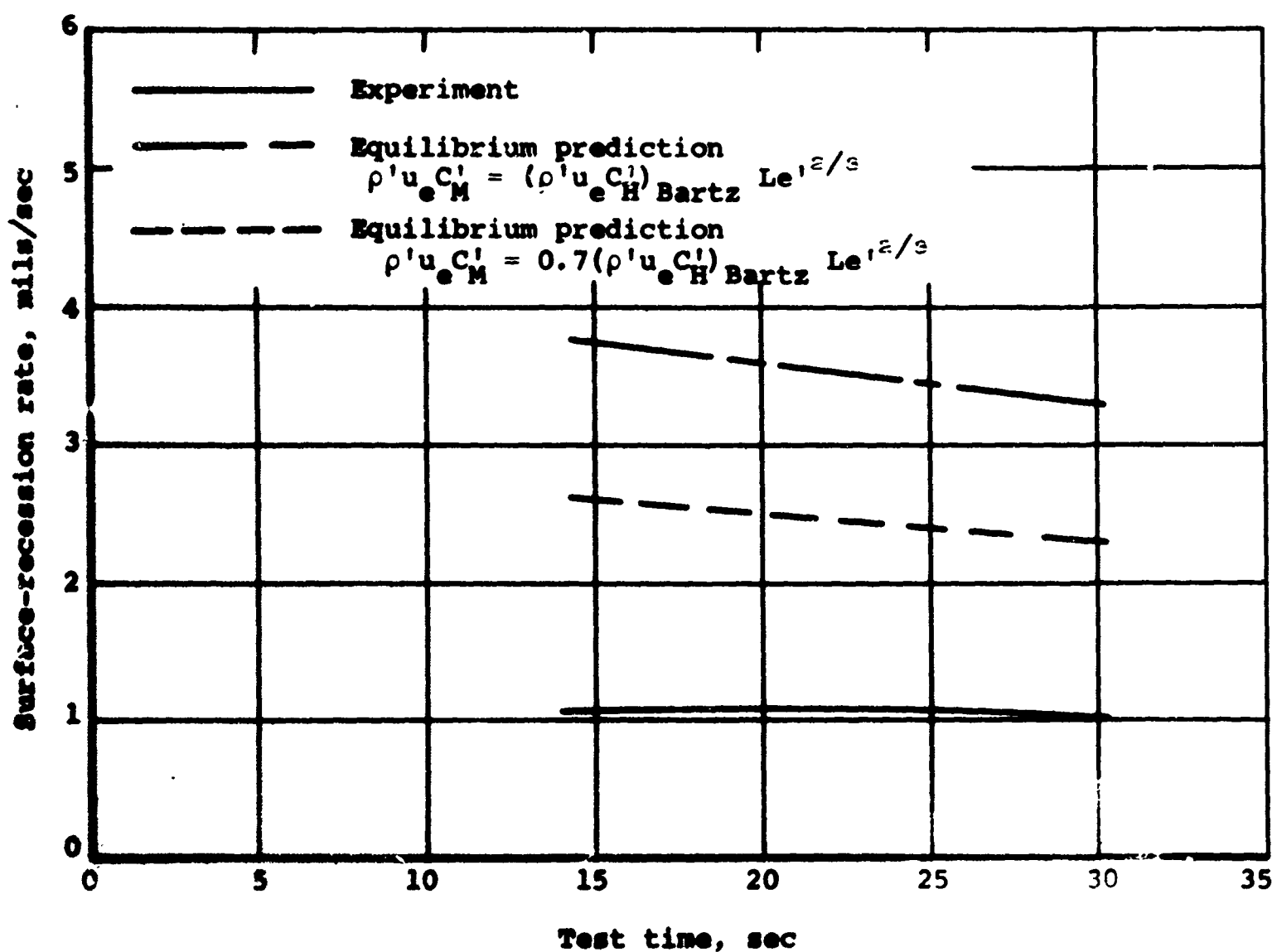
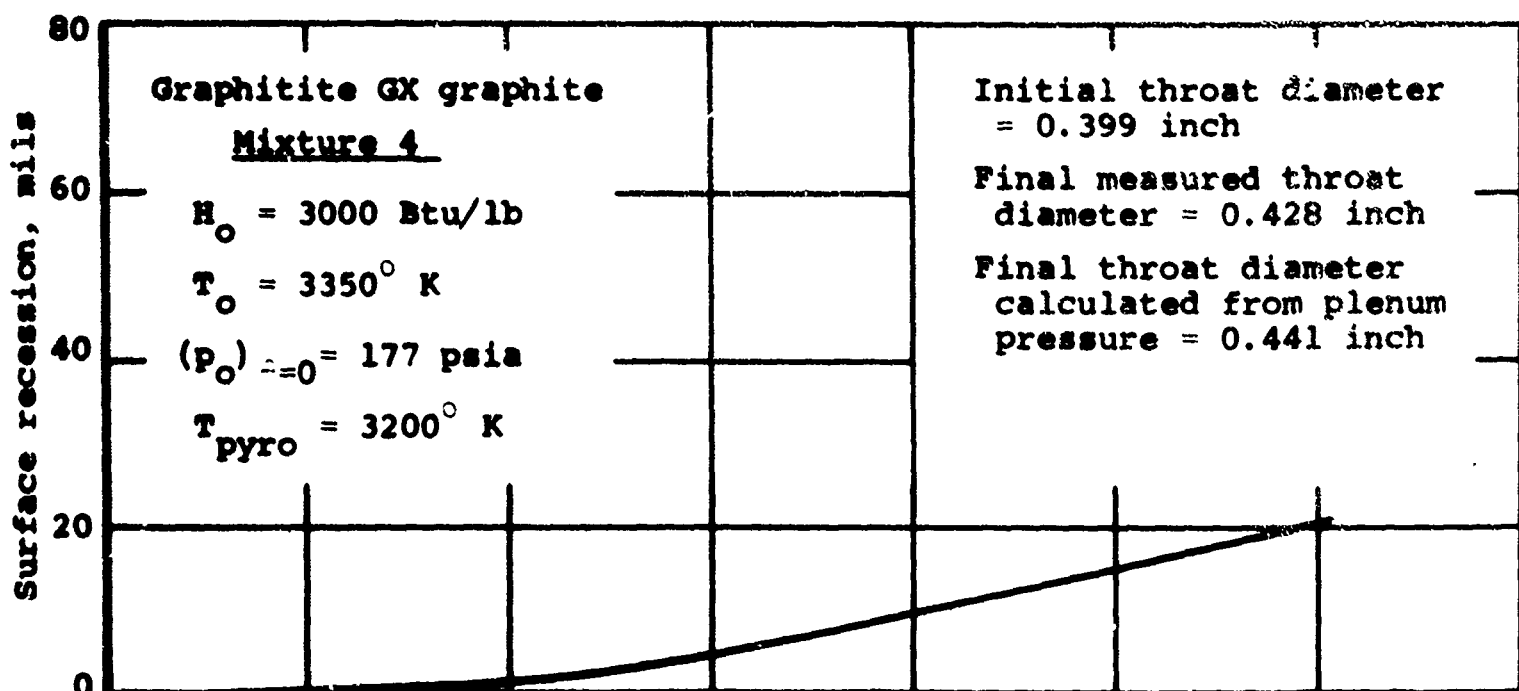
(b) Nozzle E10, Test No. 940.

Figure 18.- Continued.



(c) Nozzle E19, Test No. 997.

Figure 18.- Continued.



(d) Nozzle E31, Test No. 998.

Figure 18.- Concluded.

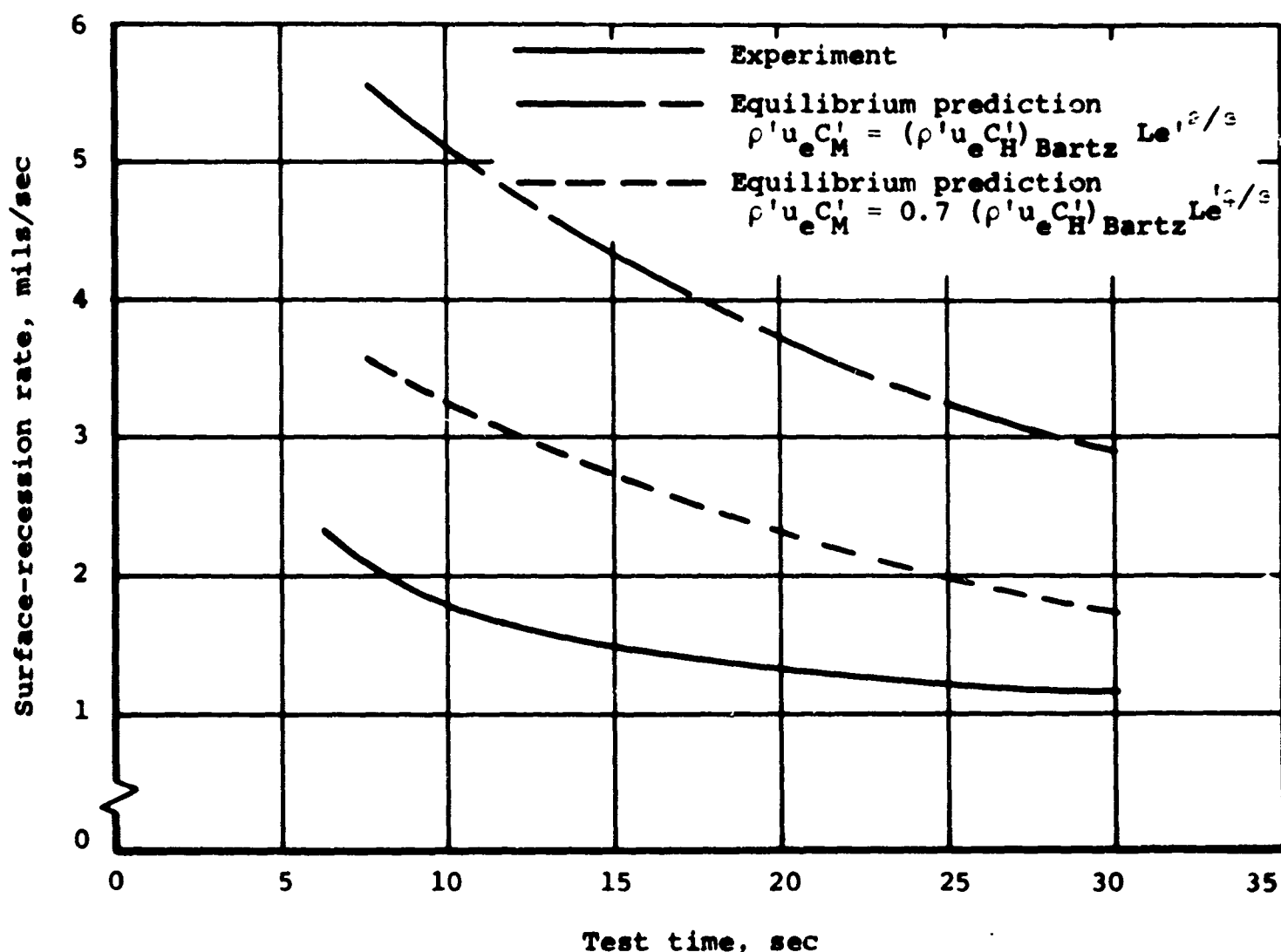
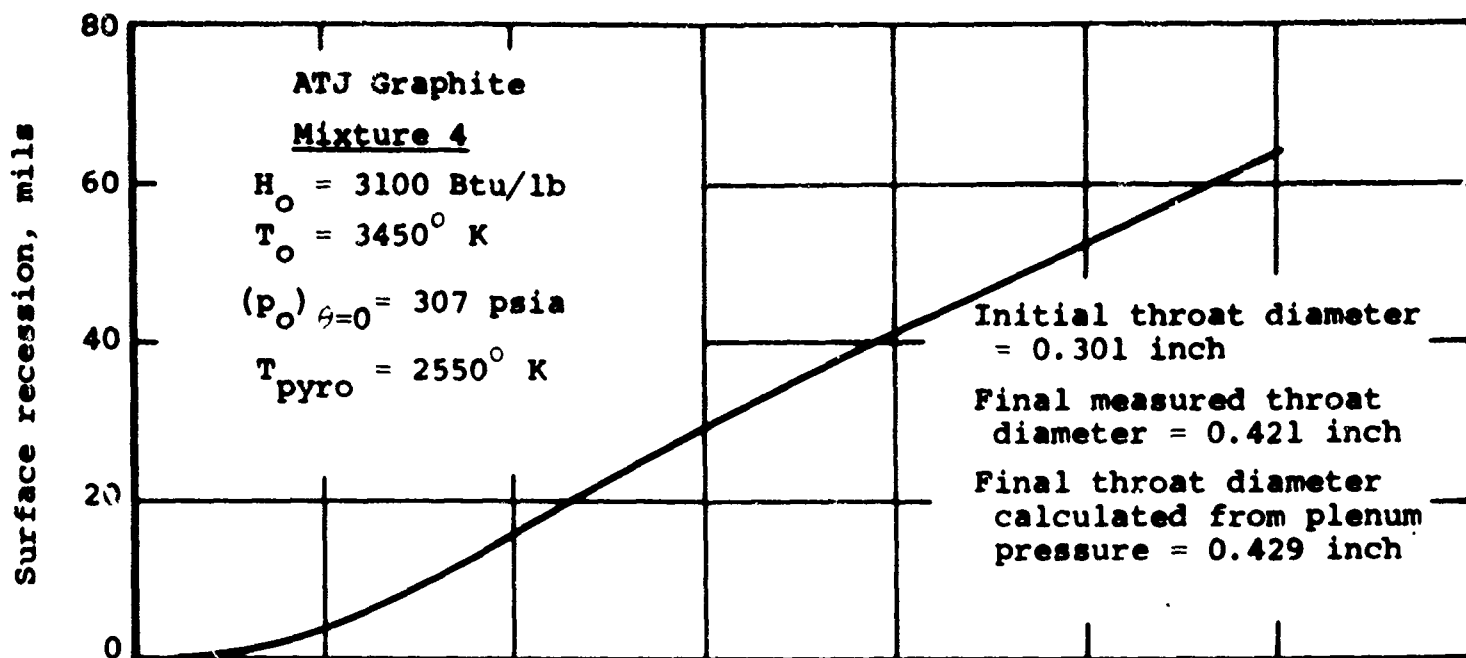


Figure 19.- Surface recession and surface-recession rate, ATJ graphite, Mixture 4, Nozzle E43, Test No. 1000.

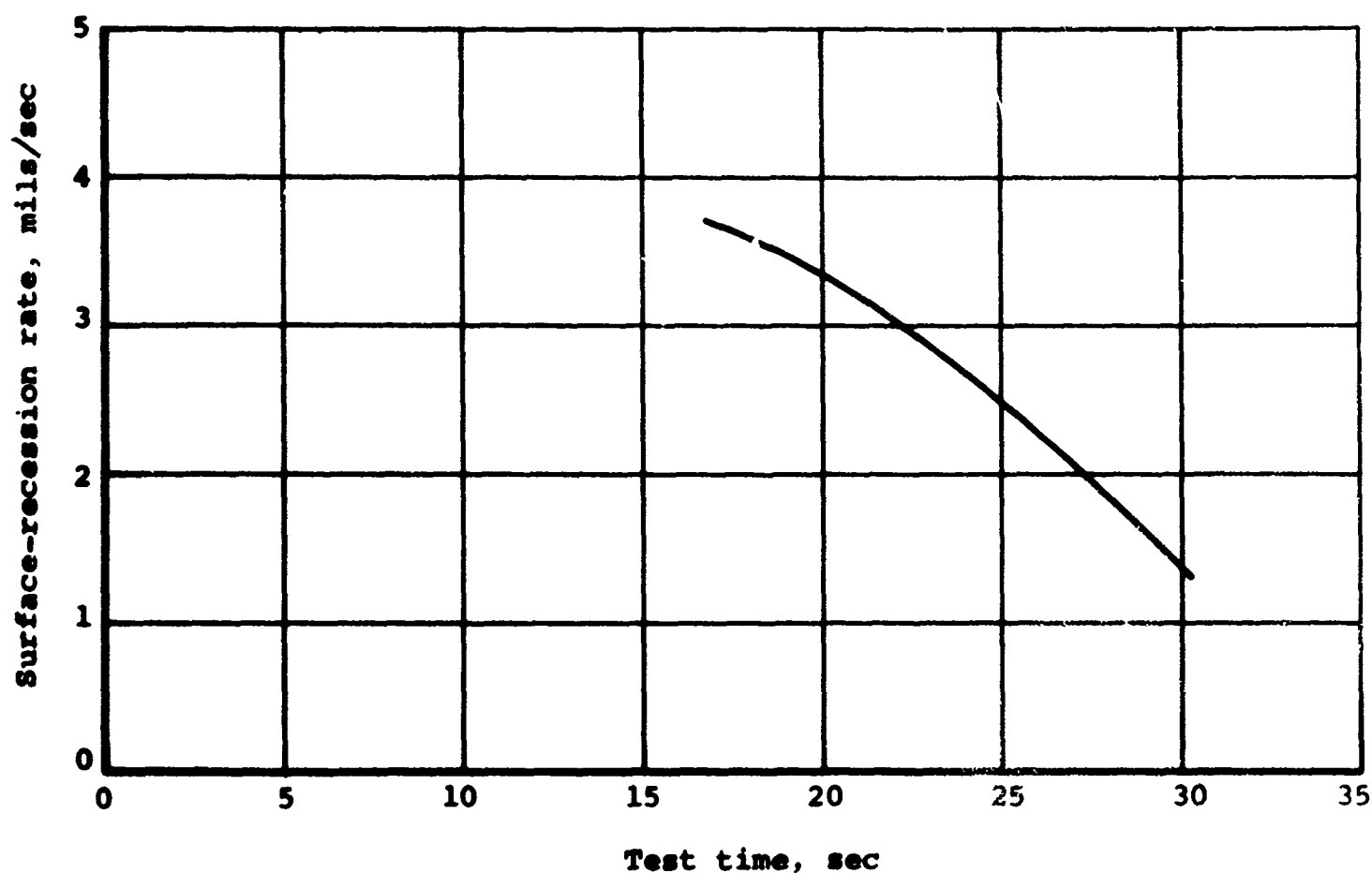
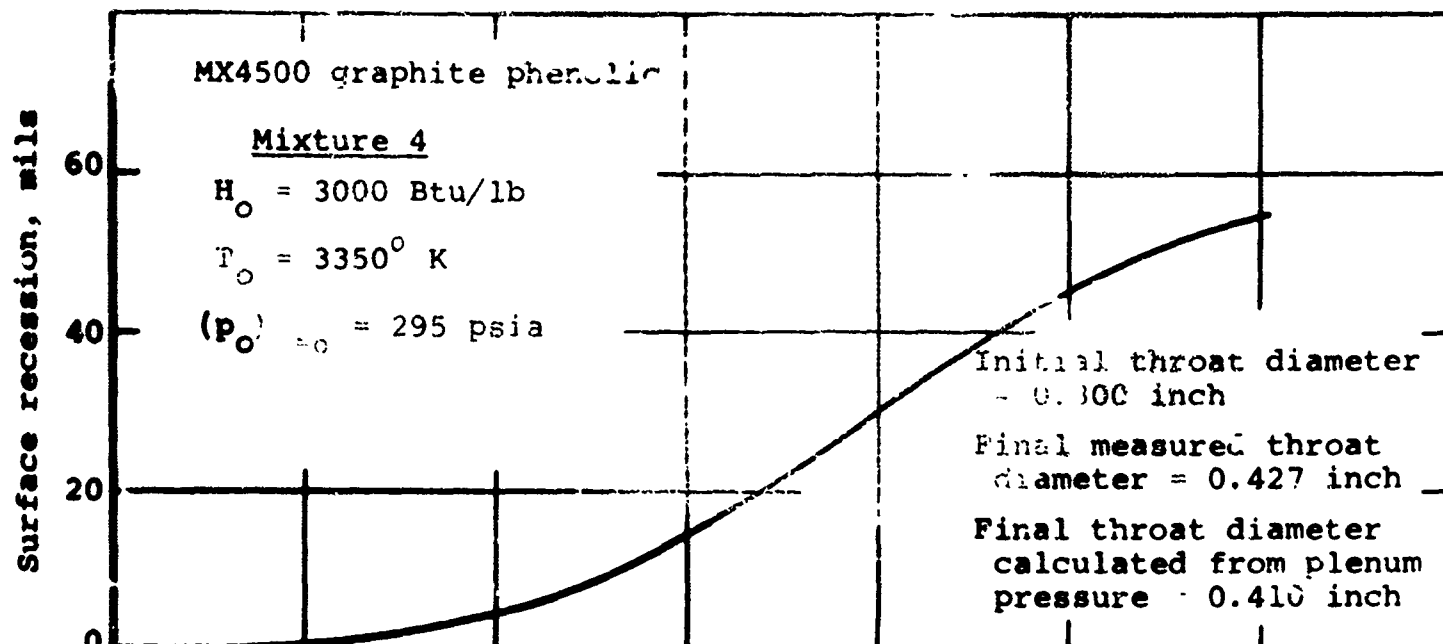


Figure 20.- Surface recession and surface-recession rate, MX4500 graphite phenolic, Mixture 4, nozzle E38, Text No. 1001.

BLANK PAGE

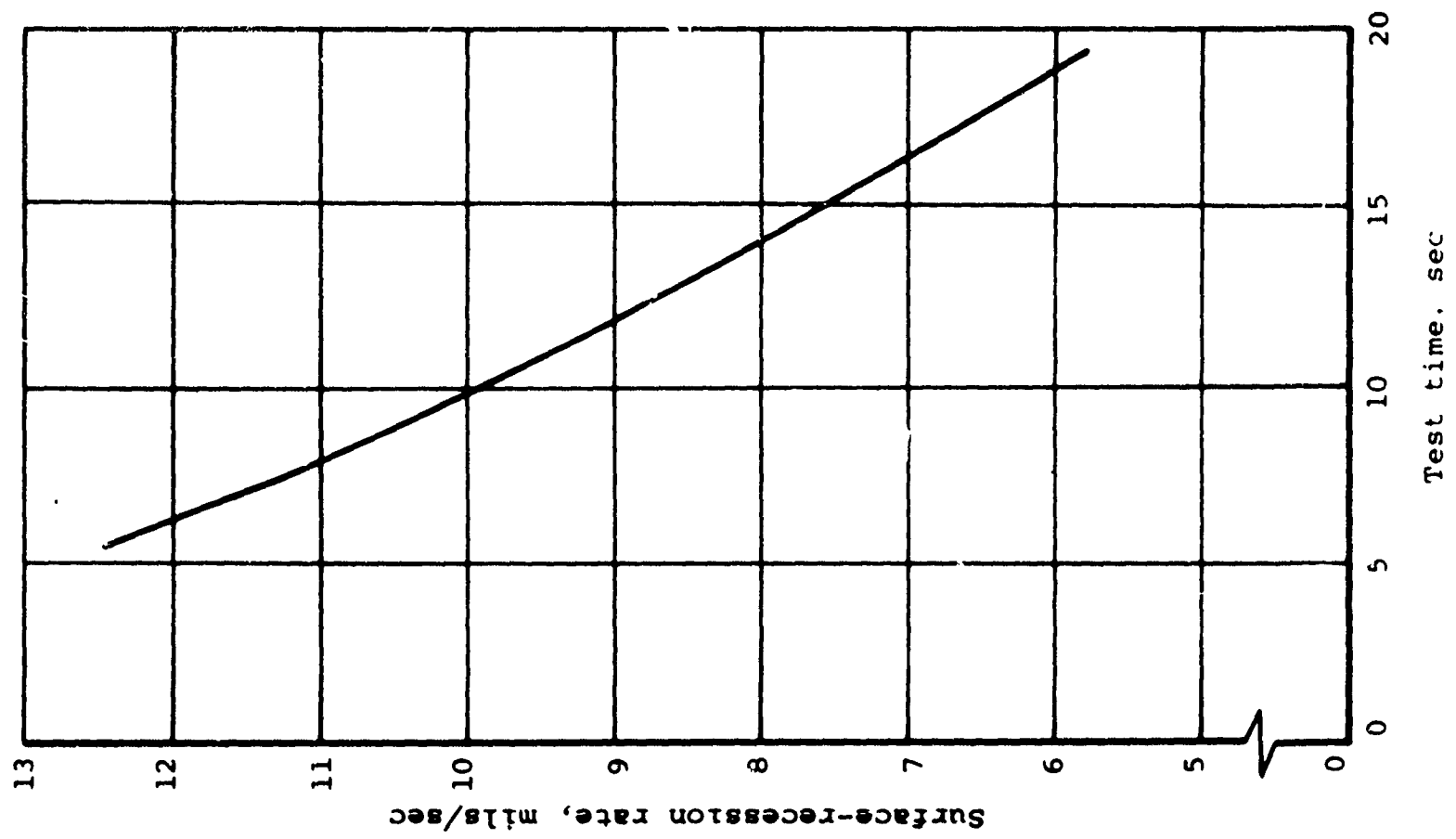


Figure 21.—Surface recession and surface-recession rate. MX2600 silica phenolic.
Mixture 4. Nozzle E22. Test No. 941.

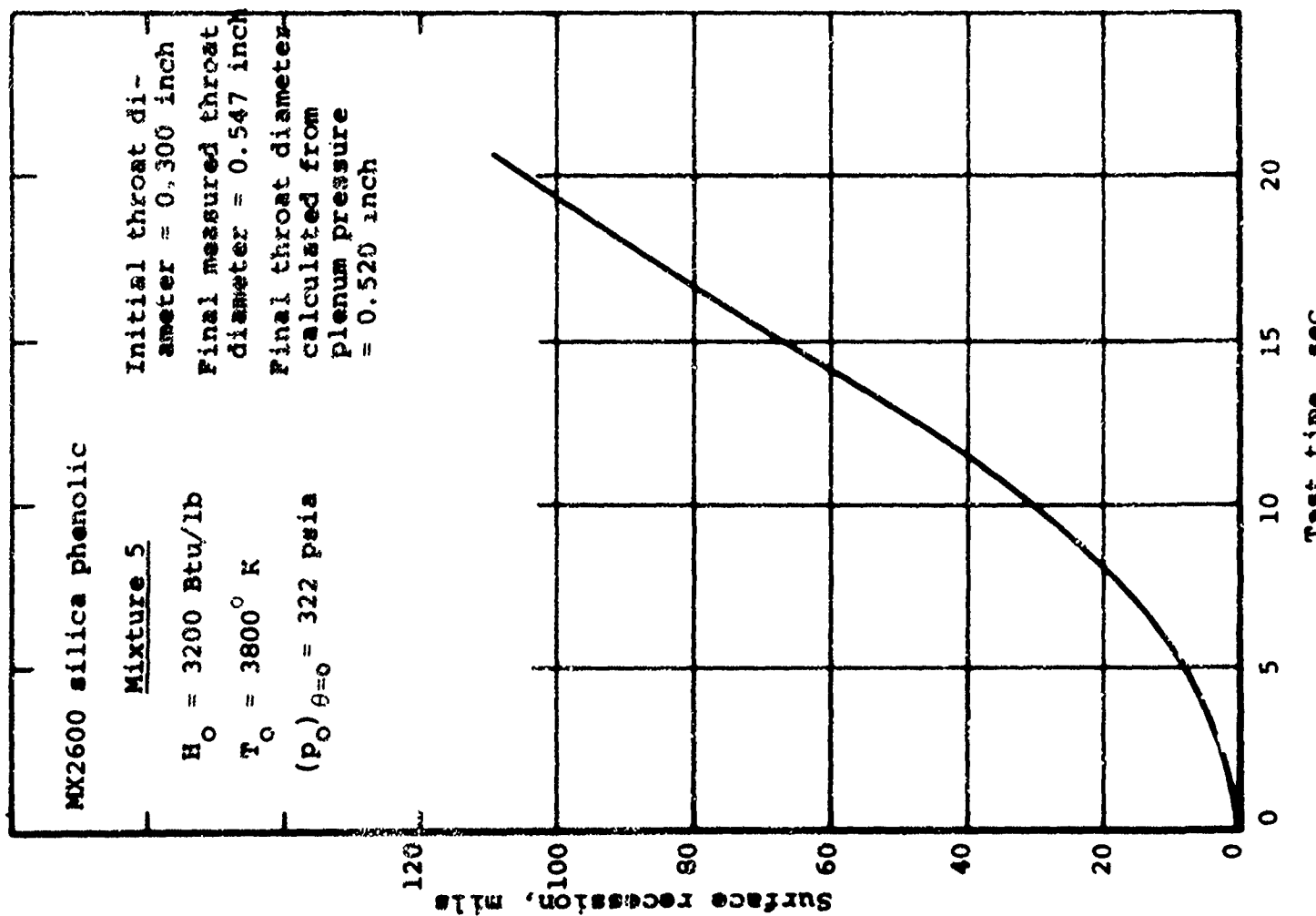
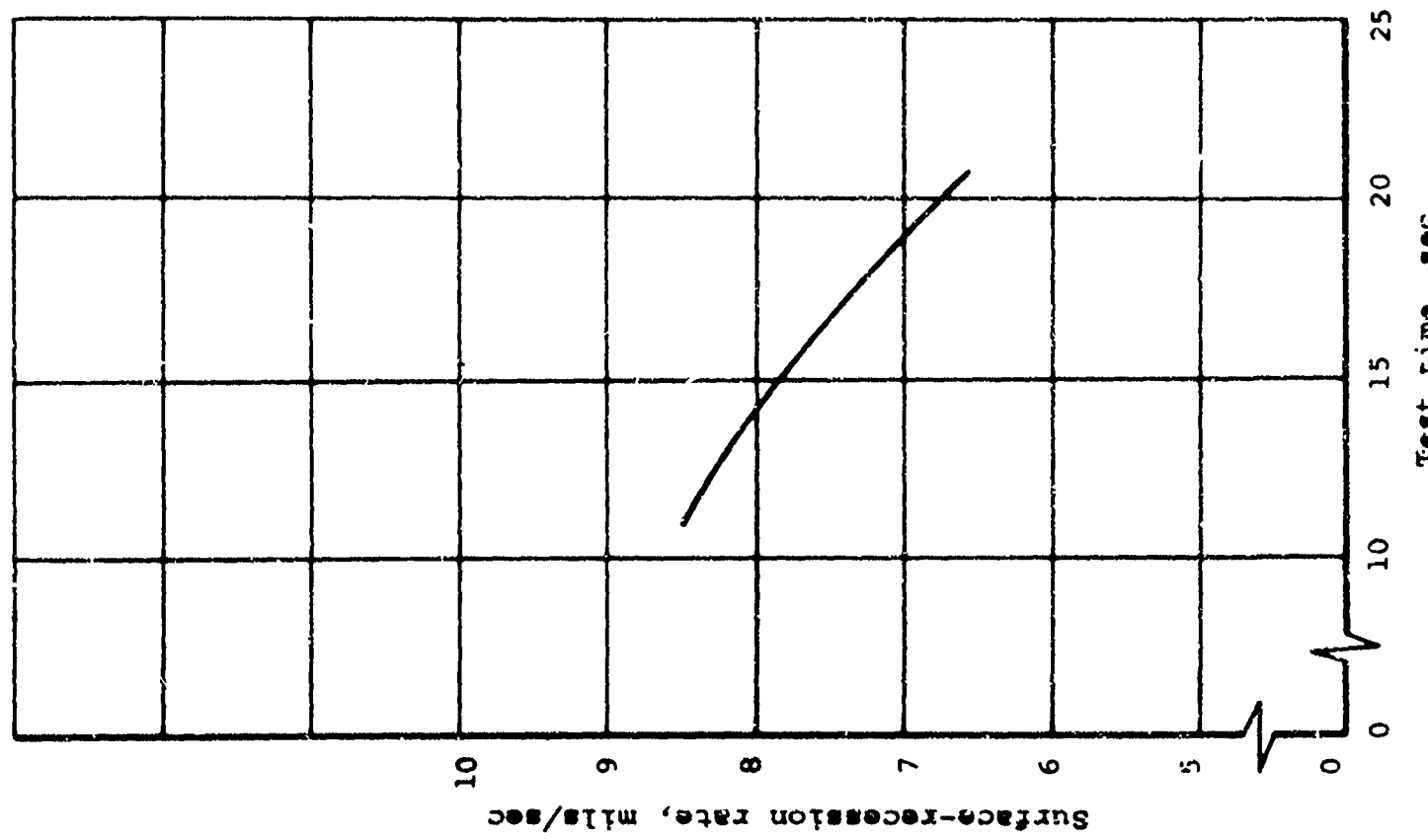


Figure 22.- Surface recession and surface-recession rate, MX2600 silica phenolic, Mixture 5, nozzle E24. Test No. 960.

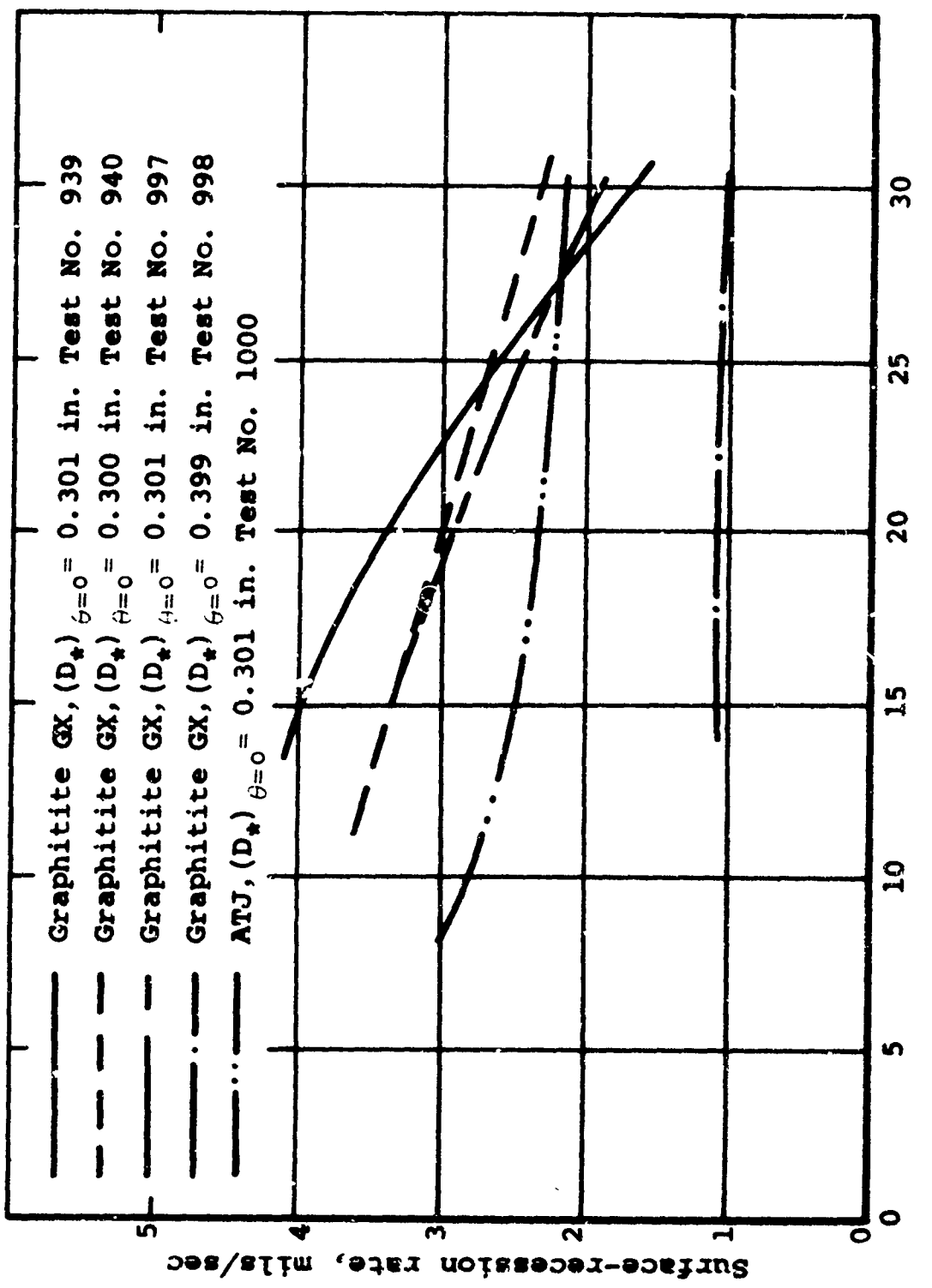


Figure 23.- Comparison of surface-recession rate for graphite-nozzle firings.

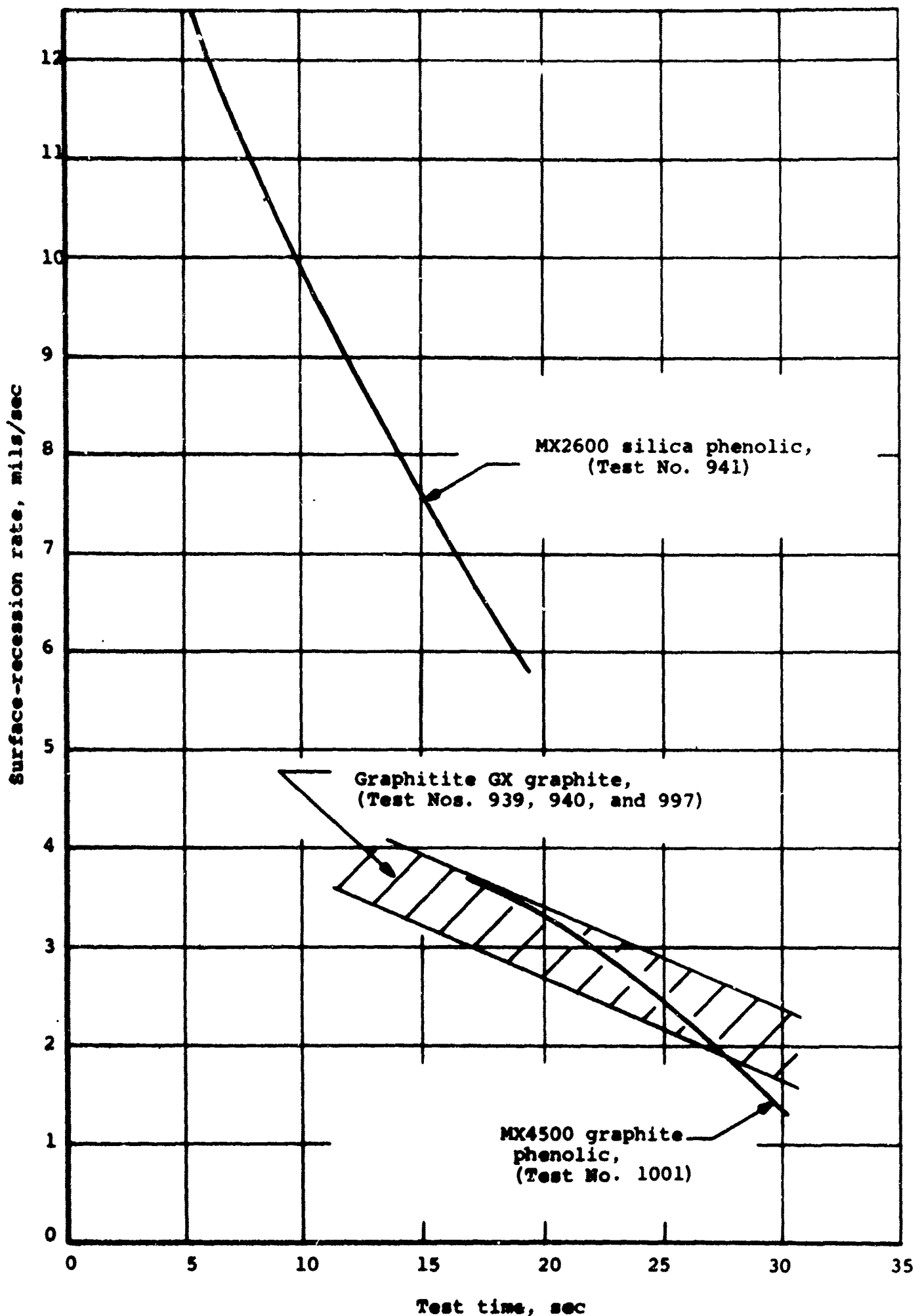


Figure 24.- Comparison of surface-recession rate for graphite, graphite phenolic, and silica phenolic.

BLANK PAGE

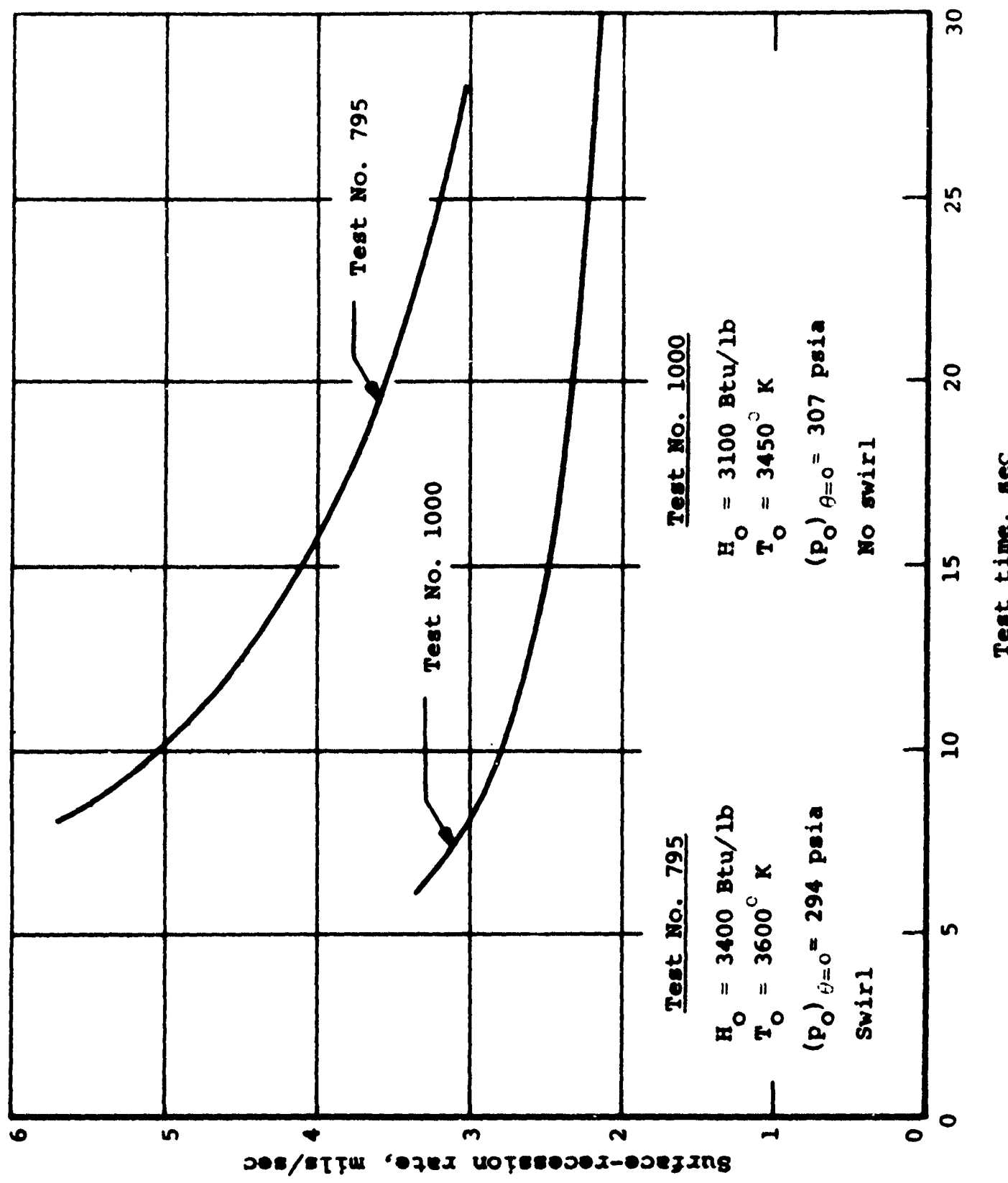


Figure 25. - Comparison of surface recession with and without swirl.

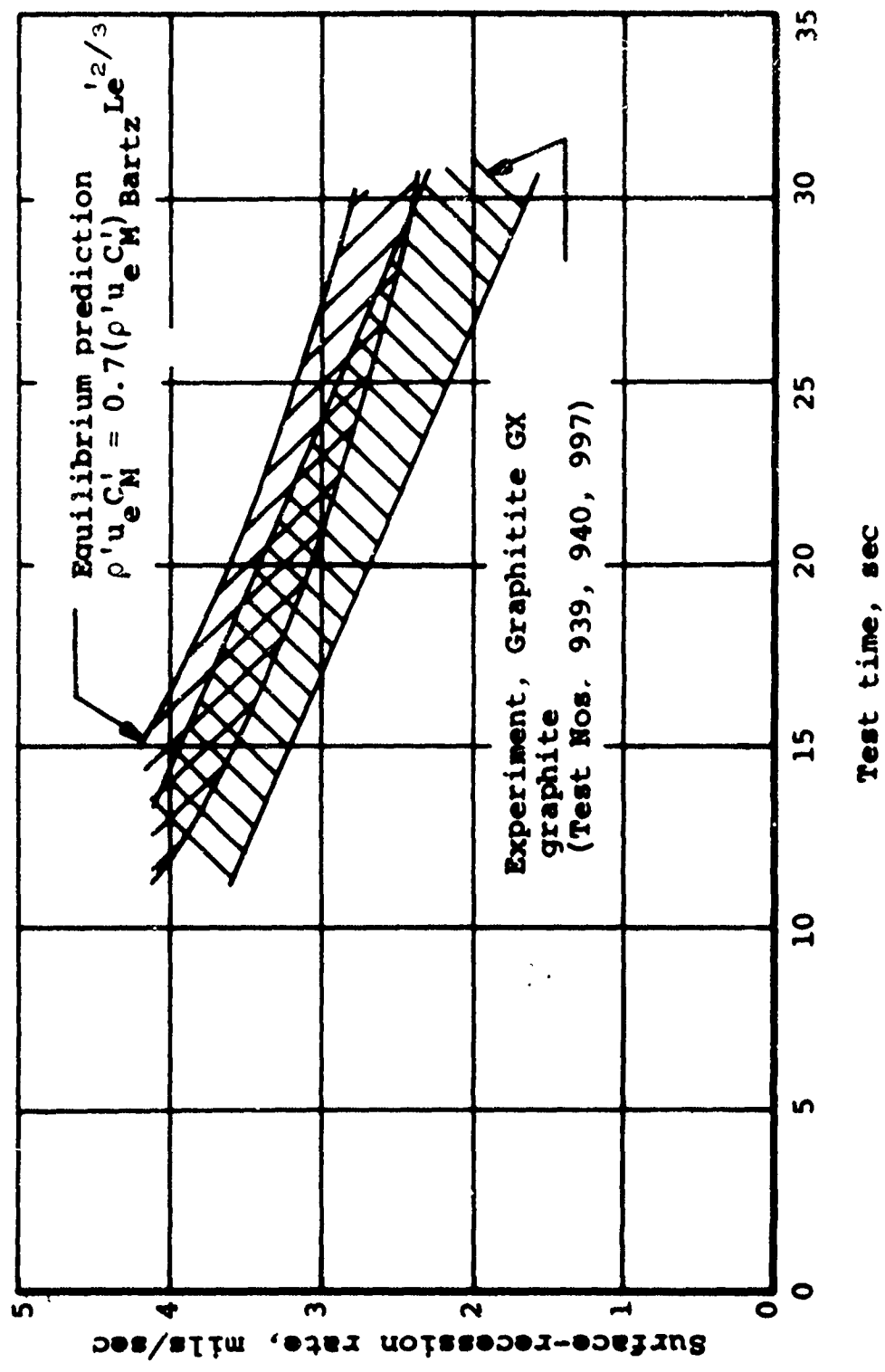
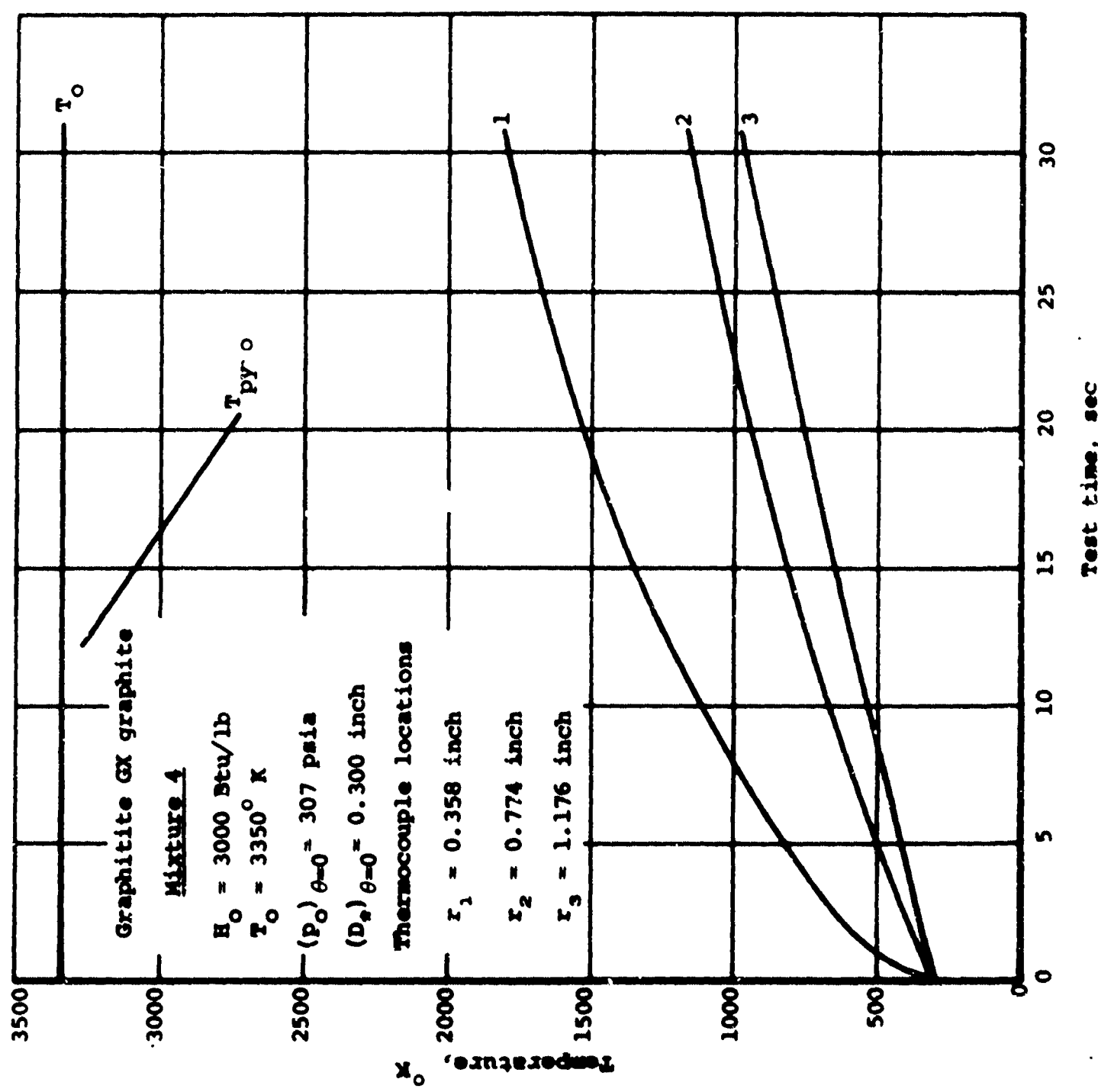
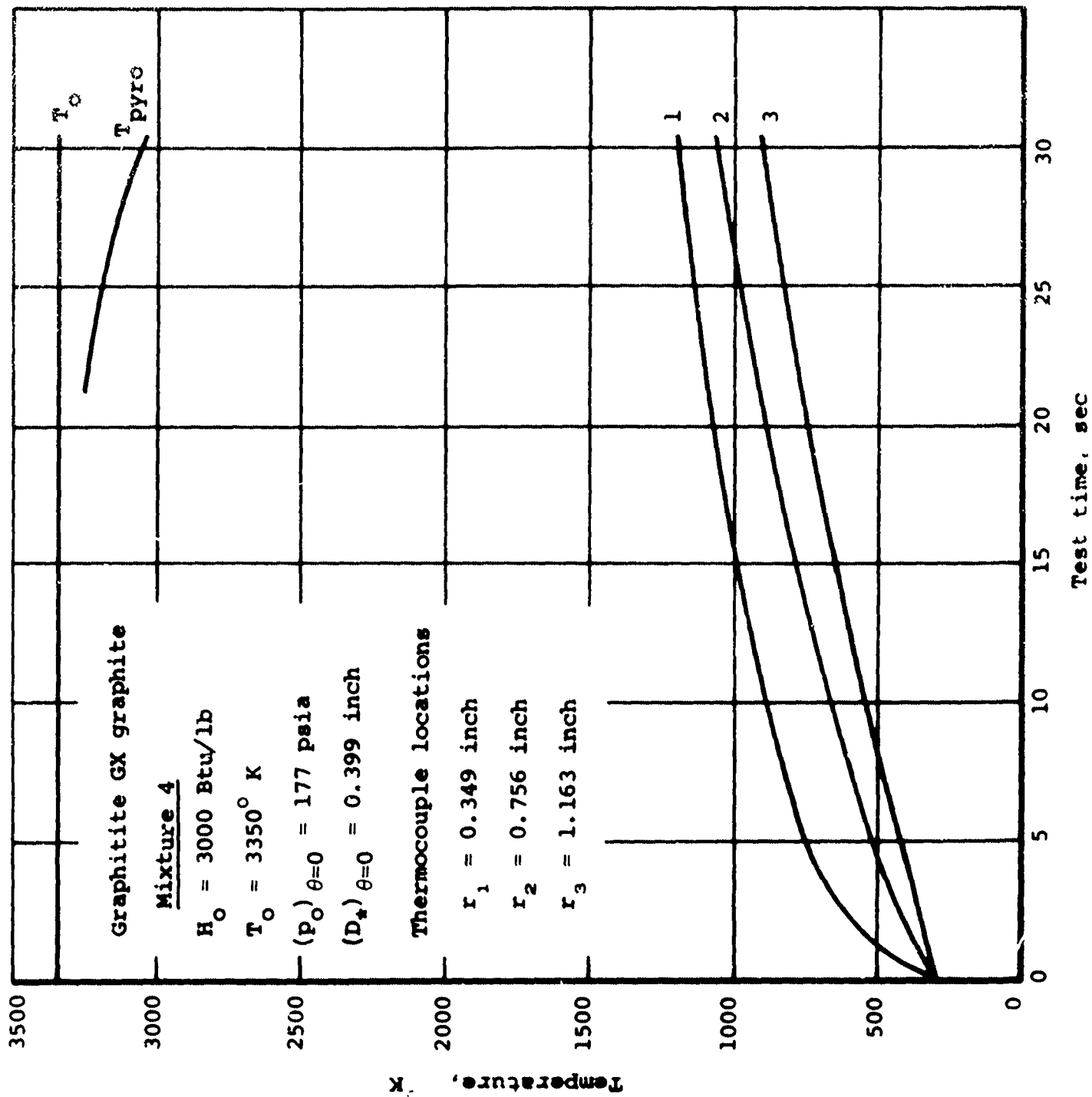


Figure 26.- Comparison of chemical equilibrium surface-recession rate prediction with experiment, graphite.



(a) Nozzle E10, Test No. 940.
 Figure 27. - Temperature histories, Graphitite GX graphite, Mixture 4.



(b) Nozzle E31, Test No. 998.

Figure 27. - (concluded).

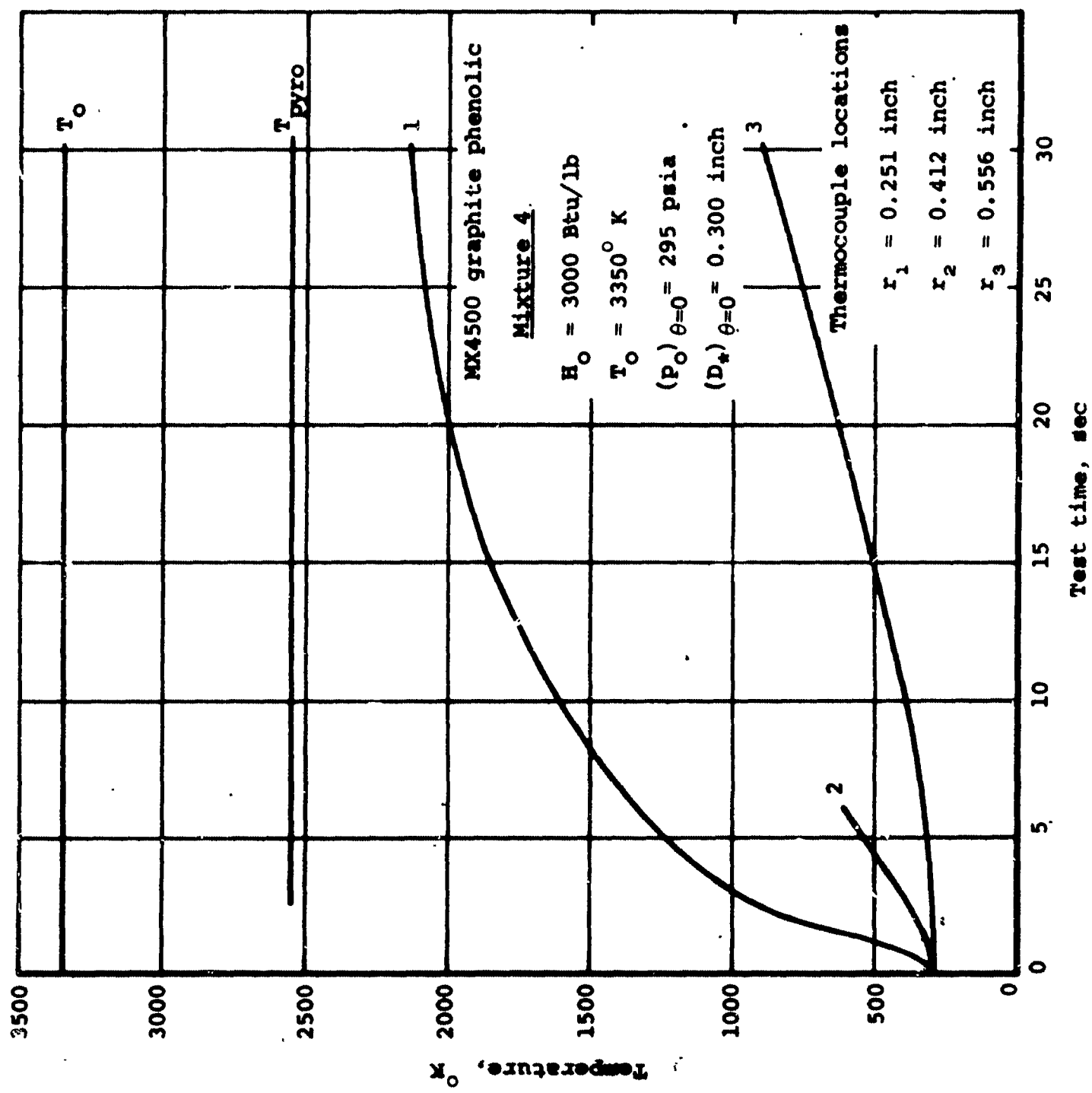


Figure 26. - Temperature histories, MX4500 graphite phenolic, Mixture 4, Nozzle E22, test No. 941.

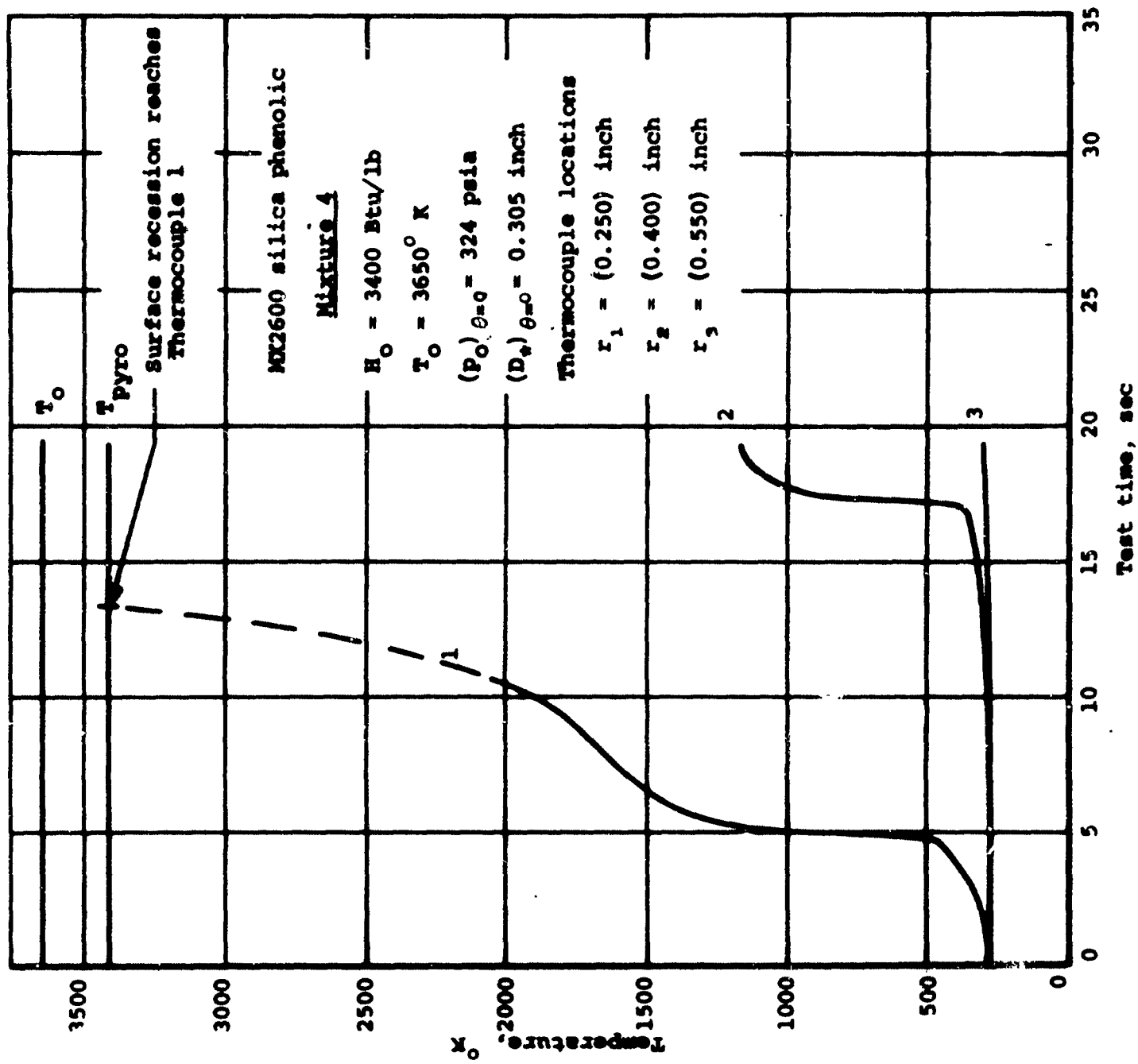
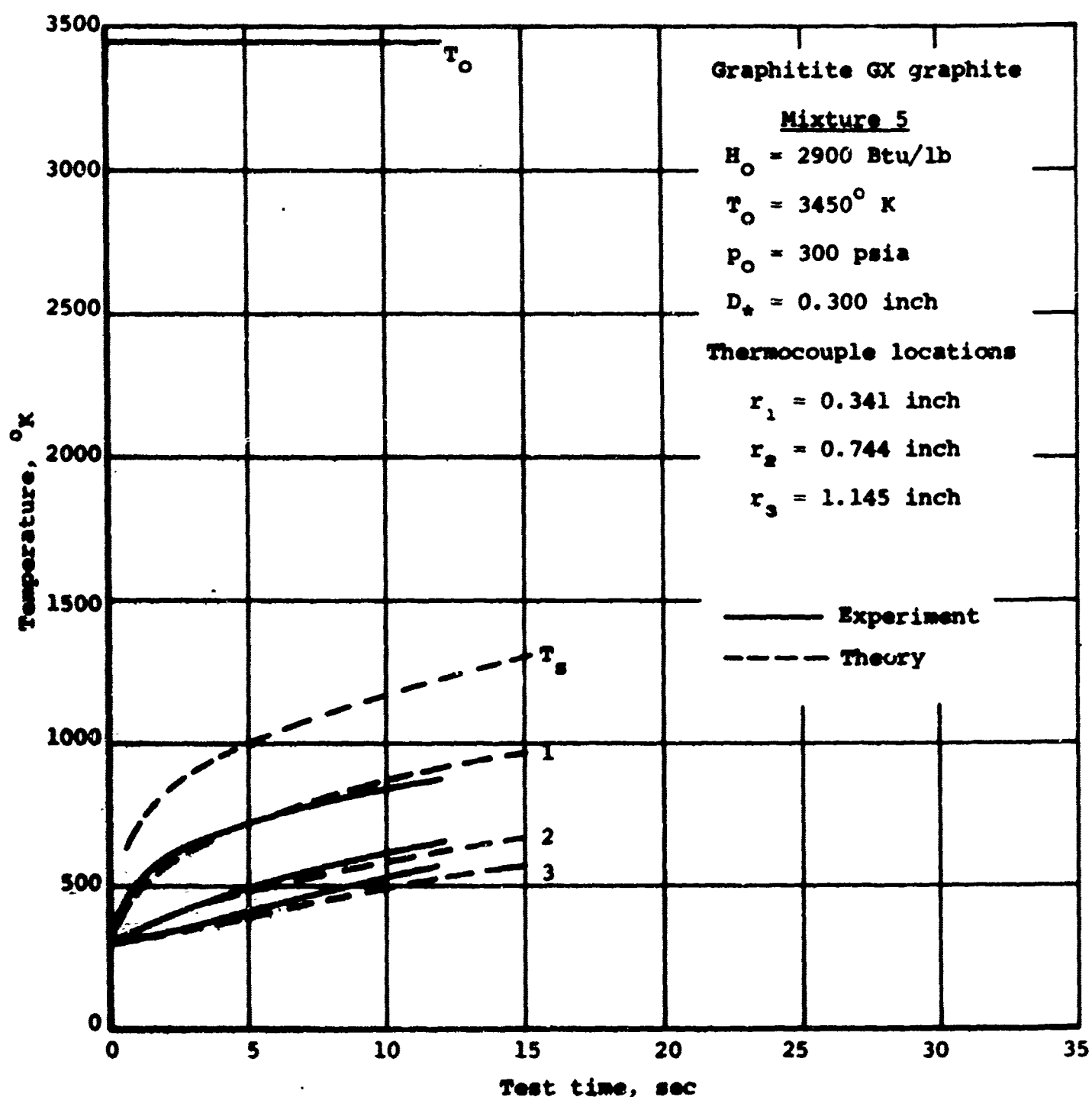
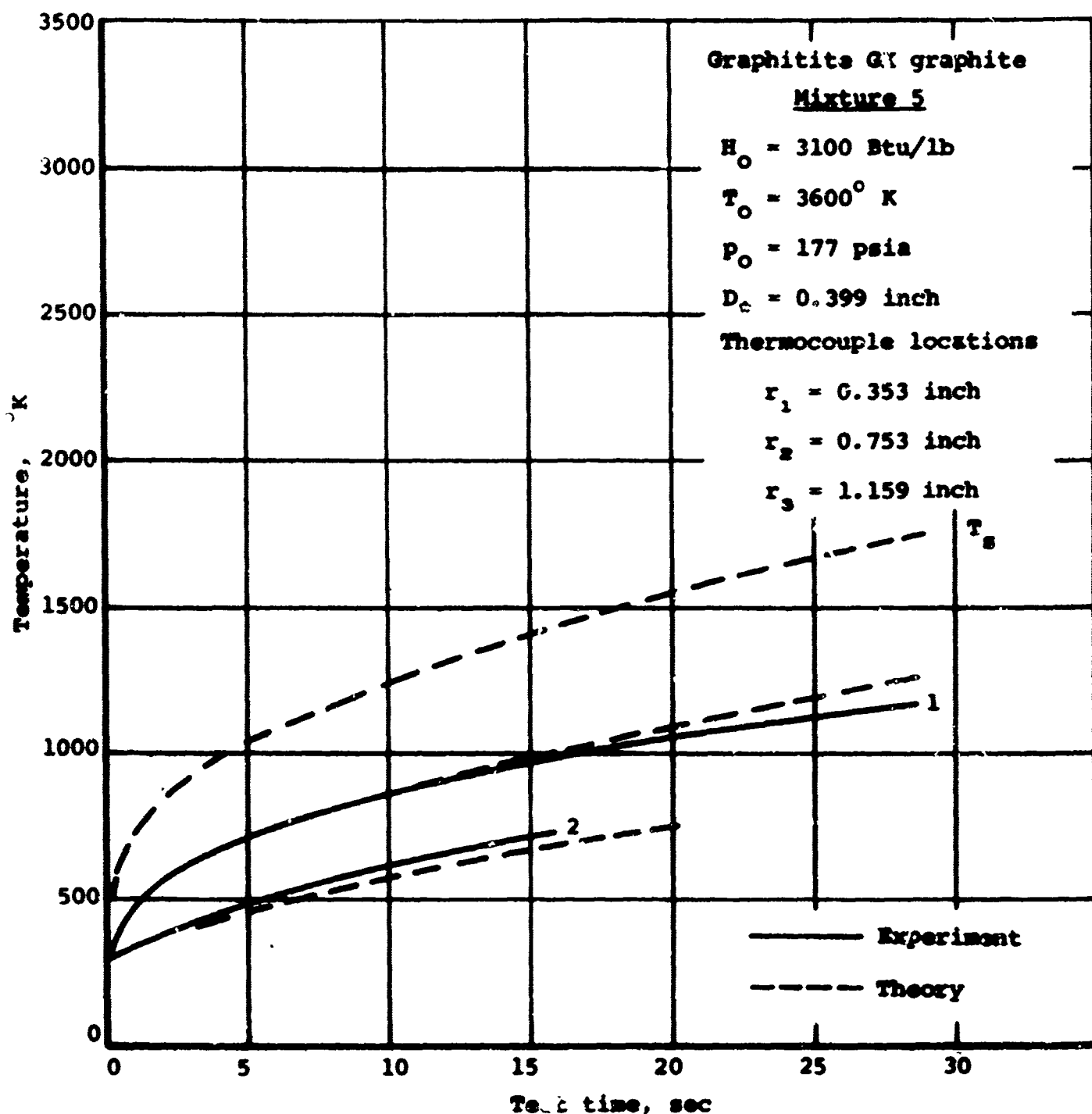


Figure 29. - Temperature histories, MK2600 silica phenolic, Mixture 4, nozzle E22, Test No. 941.



(a) No--le Ell, Test No. 959

Figure 30.- Temperature histories, Graphite GX graphite,
Mixture 5.



(b) Nozzle E32, Test No. 1004.

Figure 30.- Concluded.

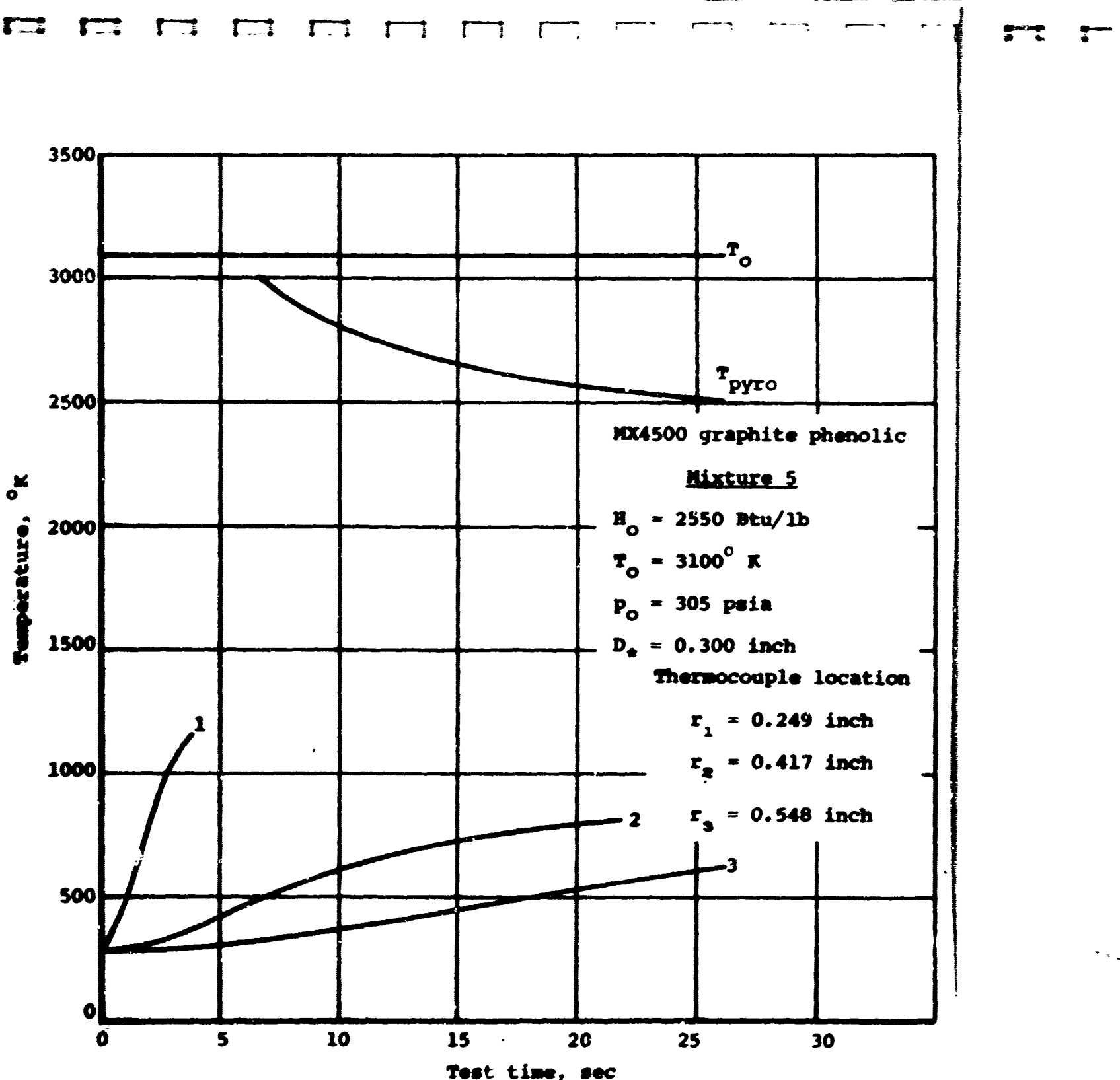


Figure 31.- Temperature histories, MX4500 graphite phenolic.
Mixture 5, Nozzle E32, Test No. 1004.

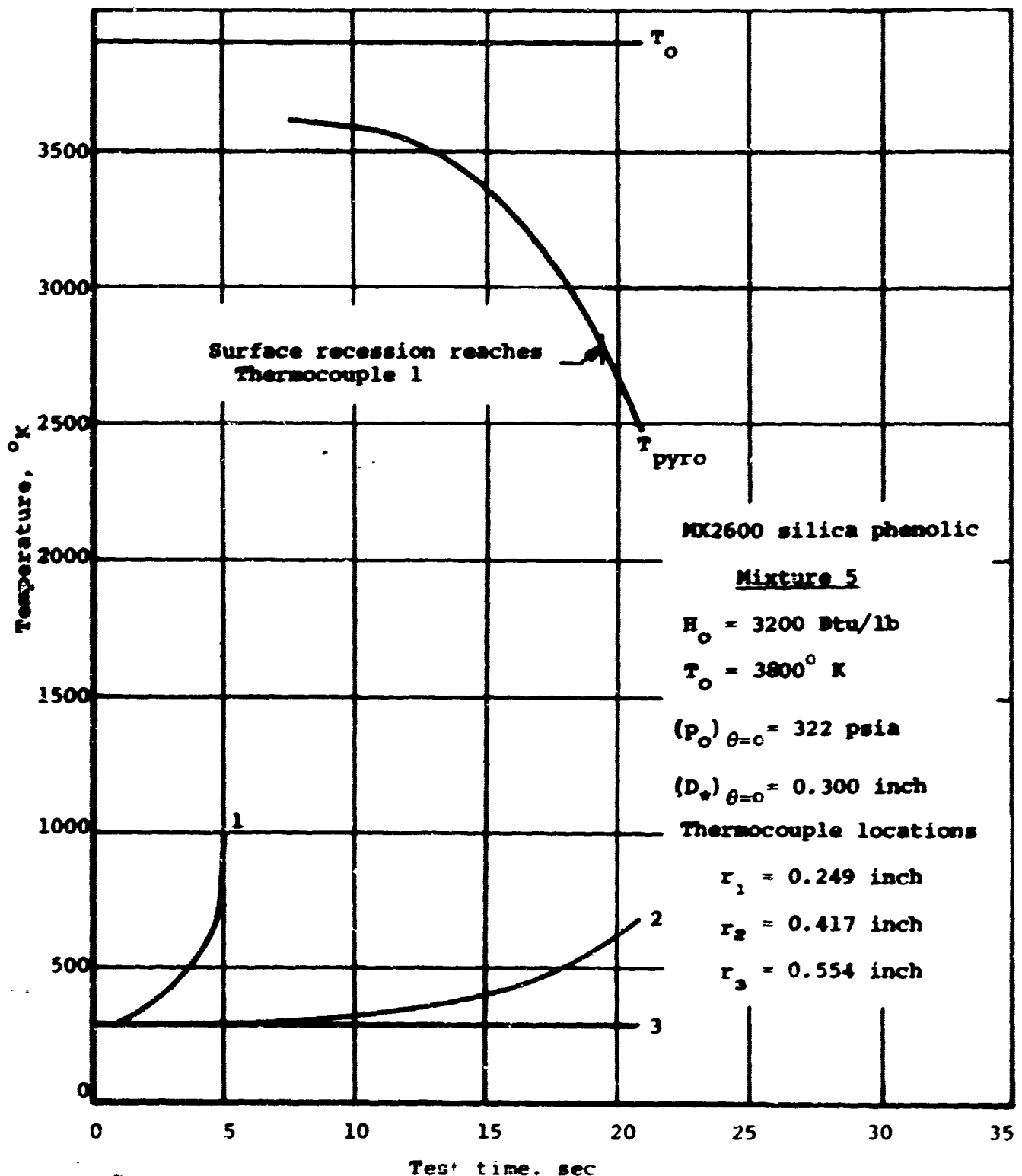


Figure 32.- Temperature histories. MX2600 silica phenolic.
Mixture 5. nozzle E32. Test No. 1004.

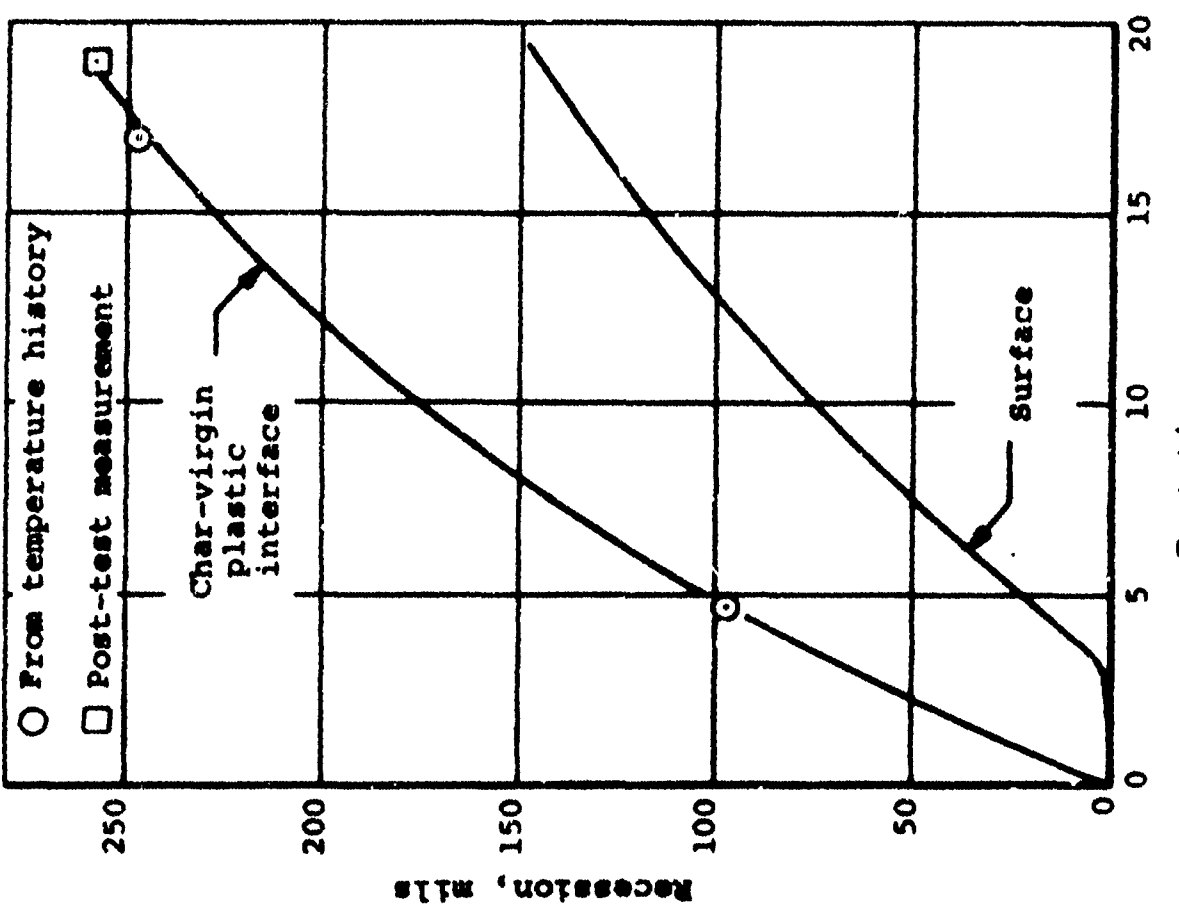
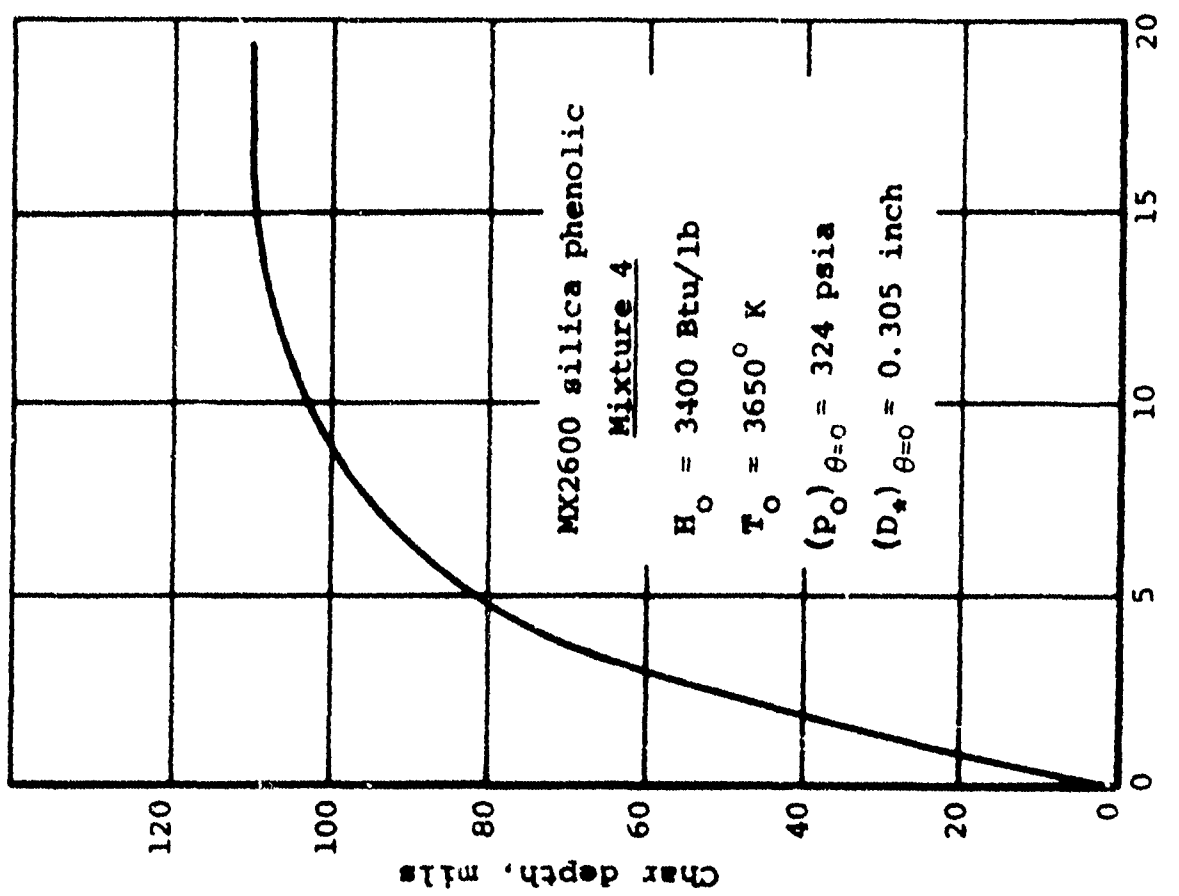


Figure 33. - Char recession and char depth, MX2600 silica phenolic, Mixture 4, nozzle E22, Test No. 941.

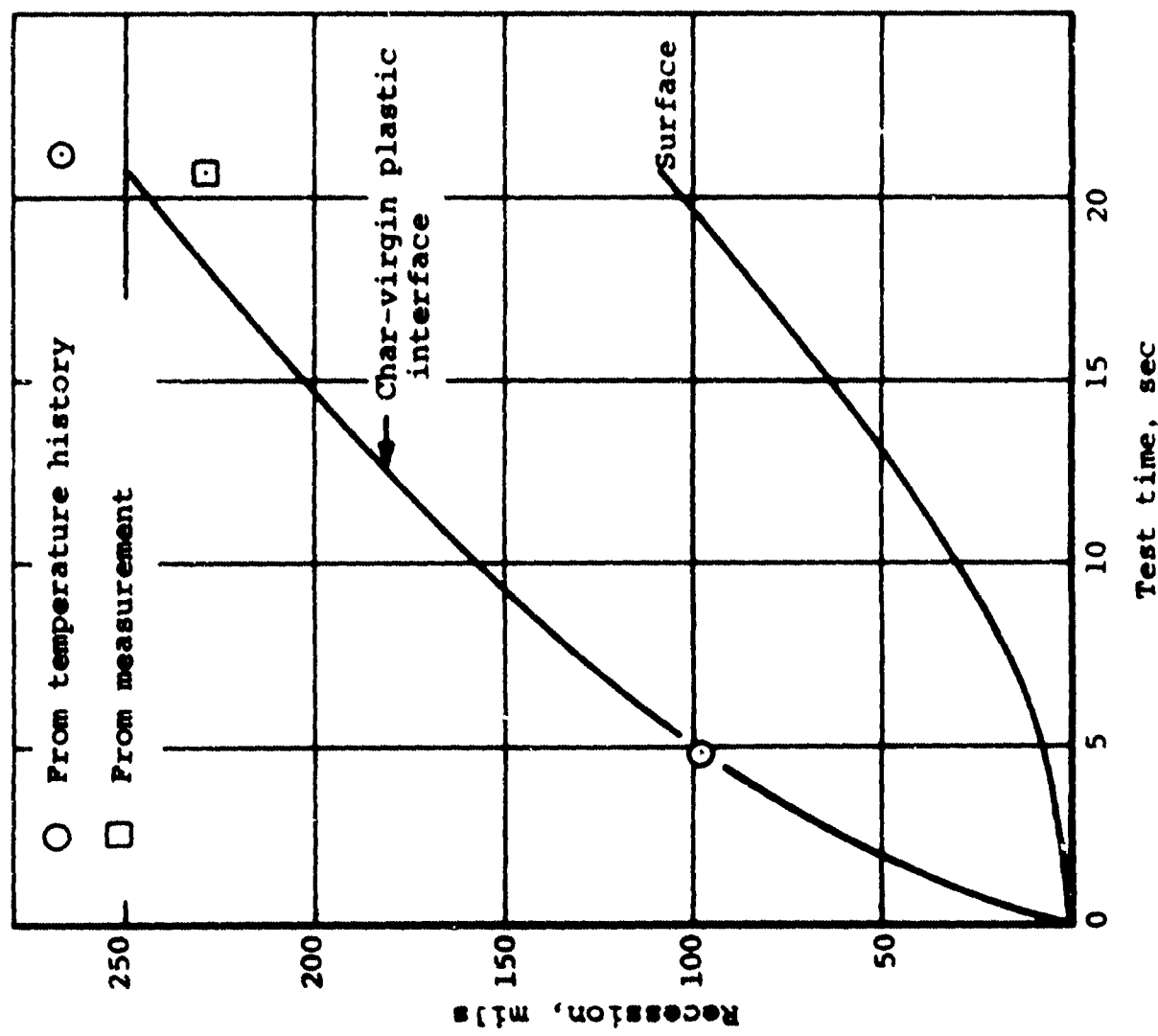
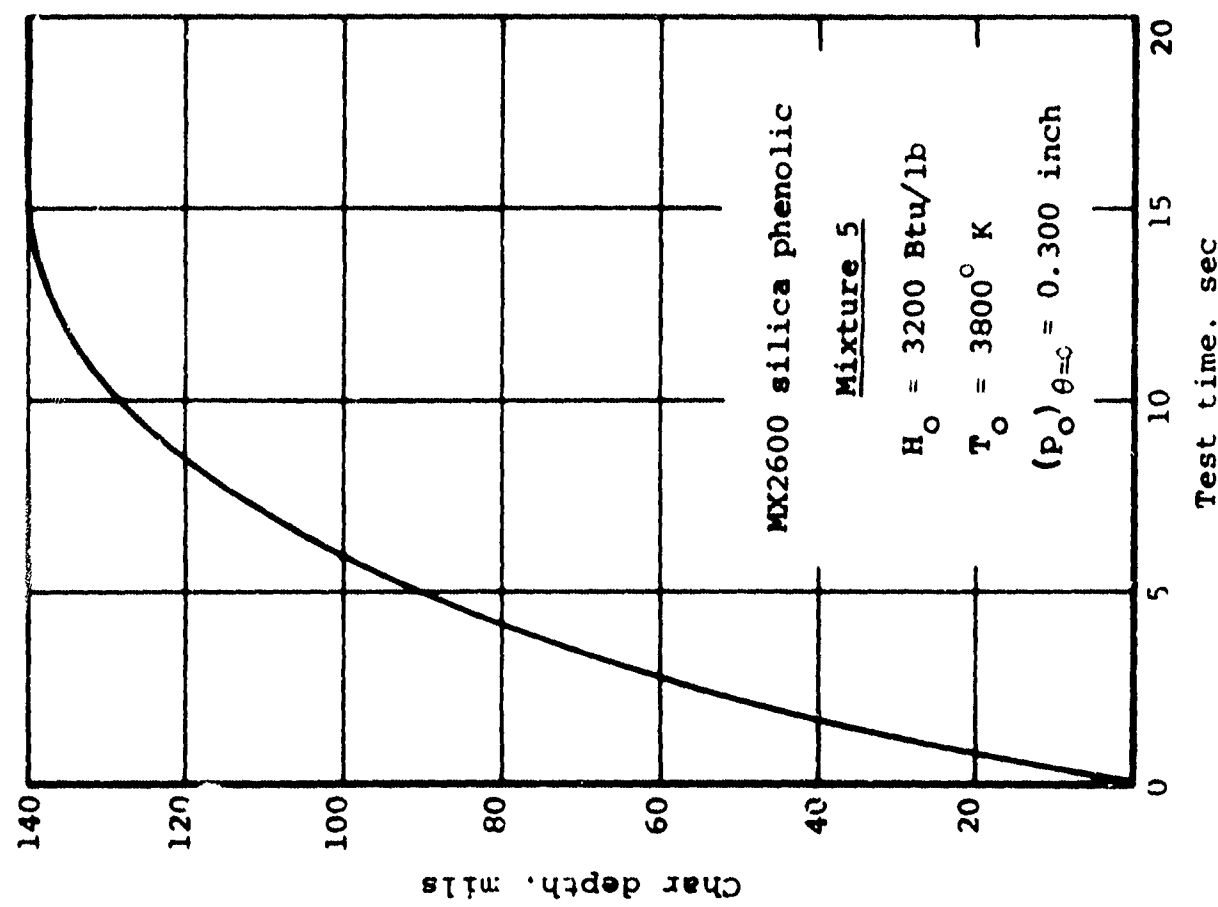


Figure 34. - Char recession and char depth. MX2600 silica phenolic. Mixture 5.
nozzle E24, Test No. 960.